

# **The Sedimentology and Architecture of Carbonate Platform Slopes**

Dissertation

with the aim of achieving a doctoral degree

at the Faculty of Mathematics, Informatics and Natural Sciences

Department of Earth Science of Universität Hamburg

Submitted by

**Marco Wunsch**

Hamburg

2017



***Eidesstattliche Versicherung***

*Hiermit erkläre ich an Eides statt, dass ich die vorliegende Dissertationsschrift selbst verfasst und keine anderen als die angegebenen Quellen und Hilfsmittel benutzt habe.*

*Hamburg, den*

*Unterschrift*

Day of oral defense: 16/01/2018

The following evaluators recommend the admission of the dissertation:

Prof. Dr. Christian Betzler

Dr. Sebastian Lindhorst

## **Abstract**

The aim of this thesis is unravel the factors controlling the architecture and sediment distribution along carbonate platform slopes. To achieve this goal, two Bahamian carbonate slopes were chosen, the leeward slope of Great Bahama Bank (GBB) and the windward slope of Cay Sal Bank (CSB). Both slopes border the Santaren Channel, a deep-water strait dominated by two contour currents flowing in opposite directions. The western part of the channel is dominated by south-directed contour currents. In the eastern part, strong contour currents flow towards the north and merge with the Florida Currents at the coalescence of the Santaren Channel with the Straits of Florida. The middle of the Santaren Channel is occupied by elongated drift body, the Santaren Drift.

The thesis relies on a dense grid of hydroacoustic data (subsurface profiler and Multibeam data), which allow new insights into slope processes and sedimentary dynamics along both slopes. Sediment samples retrieved with grab sampler, multicorer, as well as box and gravity corer complemented the hydroacoustic data. In addition, three reflection seismic surveys were used to reconstruct the depositional history of the leeward slope of GBB since the Late Miocene. The age control comes from the correlation of Ocean Drilling Program Leg 166 dates into the reflection seismic data.

The hydroacoustic data emphasize the diversity of the slope morphology and the sedimentation pattern developed during the youngest sequence, which has formed since the last glacial maximum. Both slopes are dissected by gullies, channels and furrows. Several different mechanisms produce these slope features. This includes intensified off-bank transport and tectonic movements, as well as undercutting and erosion at the toe of slope by contour currents. On the leeward slope of GBB, large slope failures occurred during the sea-level lowering after the last interglacial and formed large depressions, which are upslope bordered by scarps and gullies. These slope failures created a slope morphology that channelized the exported platform sediments during the subsequent highstand. In addition, the backscatter intensities and surface samples document the influence of contour currents on spatial sediment distribution. Along the slope of GBB, the coarsest sediments are found near the platform margin. More basinward, down to a water depth of about 560 m, there is a fining in grain size. This fining reflects the gravitational controlled grain-size distribution along carbonate platform slopes. More distally, however, the surface-sediments show a reverse pattern and the grain size coarsen again between 560 to 600 m. This coarsening is related to the contour currents, which winnow fine-grained material from this slope

segment. The windward slope of CSB is covered by very fine-grained sediments, which are derived from the southward-directed contour currents.

The sediment export of GBB was not homogenous during the Holocene. This is documented in the slope succession by sediment coarsening towards younger times and an accompanying decrease in aragonite content. Two gravity cores were analyzed for sediment composition and grain-size distribution. The cored slope succession consists of a hardground overlain by a unlithified packstone with large lithoclasts, a unlithified wackestone with a high content of aragonite needles, and a peloidal packstone on top. This succession is caused by the complex platform bathymetry, which triggered a shift in the sediment-producing community during the postglacial sea-level rise. The hardground formed during the last glacial maximum and the packstone deposited during the subsequent sea-level rise. Contemporaneous with the flooding of the platform, the margins were colonized by *Halimeda* meadows. The meadows are the source of a vast amount of fine-grained sediments, which mainly consisting of small aragonite needles. This flooding stage is represented in the slope succession by unlithified sediments with a wackestone texture. With the continuous sea-level rise, the platform interior became flooded. In the shallow platform interior a pellet-producing benthic community was established and caused a change in composition of the exported sediments. On the slope, a peloidal packstone deposited, which is characterized by a coarsening-upward trend and decreased aragonite content. The encountered change in the slope succession implies that the highstand shedding can not be seen as a simple on-off mechanism, in which the platform export is only controlled by the sea-level position. Local factors like platform bathymetry and sediment-producing communities are also important in controlling texture and composition of the exported sediments.

The deeper parts of the leeward slope of GBB are imaged in the reflection seismic data as seismic sequences, produced by third order sea-level fluctuations. In addition, the data document how the current regime shaped the slope. The current control strengthens towards the north and is highest where the contour currents coalesce with the Florida Current. Along this slope segment, drift migration and current winnowing at the toe of slope form a deep moat. Here, the slope progradation is inhibited by channel incisions and the accumulation of large mass transport complexes, triggered by current winnowing. Towards the south, where the current control is less intensive, the accumulation of mass transport complexes and channel incision are rather controlled by the position of the sea level. Large slope failures were triggered during the Mid-Pleistocene transition and Mid-Brunhes event, periods characterized by changes in the cyclicity or the amplitude of sea-level fluctuations. The high

resolution hydroacoustic data imaged four additional sequences in the succession of the upper Pleistocene, originated in fourth order oscillations of the sea level. These sequences also show clear differences in function of the slope exposure to contour currents. To emphasize the role of the slope morphology and the currents in the facies distribution in these upper Pleistocene sequences, two stochastic models were developed. In areas of high currents influence, an interplay of erosional and depositional processes form a complex facies pattern with downslope and along strike facies alterations. In areas with lower current influence, major facies alternations occur predominately in downslope direction, and a layer-cake pattern characterizes the along strike direction. The results of this thesis stress established models for carbonate slopes by determining timing and the trigger mechanisms of slope failures, channel incisions and bedforms on two Bahamian slopes. In addition, it is shown that contour currents is an underestimated driver for sedimentation and slope architecture.

## Zusammenfassung

Der Zweck dieser Dissertation ist es die Faktoren zu ermitteln, die die Architektur und Sedimentverteilung entlang von Karbonatplattformhängen kontrollieren. Um dieses Ziel zu erreichen, wurden zwei bahamaische Karbonathänge ausgewählt, Der leewärtige Hang der Großen Bahamas Bank (GBB) und der luvwärtige Hang der Cay Sal Bank (CSB). Beide Hänge begrenzen die Santaren Straße, eine Tiefwasserstraße die von zwei gegenläufigen Konturströmungen dominiert ist. Der westliche Teil der Santaren Straße ist dominiert von einer südwärts gerichteten Strömung. Im östlichen Teil fließt eine starke Strömung nordwärts, diese vereinigt sich weiter im Norden mit dem Floridastrom. In der Mitte dieser Wasserstraße erstreckt sich ein Driftkörper, der Santaren Drift.

Die vorliegende Arbeit basiert auf einem dichten Netz aus hydroakustischen Daten (Sedimentecholot und Fächerecholot), welches neue Erkenntnisse in die Hangprozesse und Sedimentdynamik entlang dieser beiden Hänge bieten. Sedimentproben gewonnen mittels Backengreifer, Multicorer, sowie Kastengreifer und Schwerelot ergänzen die hydroakustischen Daten. Zusätzlich wurden drei reflektionsseismische Datensätze bearbeitet, um die Ablagerungsgeschichte des leewärtigen Hanges der Großen Bahamas Bank seit dem Spätmiozän zu rekonstruieren. Eine genaue Alterskontrolle wurde durch die Korrelation der Reflektionsseismik mit Kerndaten erreicht, welche während der Expedition 166 des Ocean Drilling Program (ODP) gewonnen wurden.

Die hydroakustischen Daten dokumentieren eine vielfältige Hangmorphologie und ein einzigartiges Sedimentationsmuster, die sich seit dem letzten glazialen Maximum gebildet haben. Beide Hänge sind durchzogen von Rinnen, Kanälen und Furchen, welche durch unterschiedliche Prozessen gebildet wurden. Diese Prozesse umfassen einen verstärkten Plattformexport, Tektonik und Hangfußerosion durch die Konturströmung. Der Meeresspiegelabfalls nach dem letzten Interglazial löste entlang des leewärtigen Hanges der Großen Bahamas Bank großflächige Hangrutschungen aus. Diese Rutschungen formten weitläufige Senken, die hangaufwärts durch Abbruchkanten und Rinnen begrenzt sind. Die so entstanden Hangmorphologie kanalisierte die exportierten Plattformsedimente während des darauffolgenden Meeresspiegelhochstandes. Die Rückstreuungsintensitäten des Fächerecholots und die Oberflächenproben zeigen einen Einfluss der Konturströmung auf die Sedimentverteilung des leewärtigen Hanges der GBB. Die größten Sedimente finden sich im proximalen Teil des Hanges, wobei die Korngröße mit zunehmender Wassertiefe abnimmt und somit der angenommene gravitationsgesteuerten Korngrößenverteilung entlang von Karbonathängen folgt. Am Hangfuß (ca. 560 m Wassertiefe) nimmt die

Korngröße wieder zu, durch die Strömungserosion von feinkörnigem Material. Der luvwärtige Hang der CSB ist bedeckt mit feinkörnigen Sedimenten, die durch die Konturströmung dorthin transportiert wurden.

Der Plattformexport der GBB war nicht homogen während des Holozäns. Dokumentiert ist dies in der Abfolge des leewärtigen Hangs in einer Kornvergrößerungssequenz (*Coarsening upward*), welche begleitet ist von einem abnehmenden Aragonitgehalt. Zwei Schwerelotkerne wurden auf die Sedimentzusammensetzung und Textur hin analysiert. Die erbohrte Hangabfolge besteht aus einem Hartgrund überlagert von einem Packstone mit großen Lithoklasten, einem feinkörnigen Wackestone mit hohem Aragonitgehalt und einem peloidalem Packstone. Diese Veränderung in den exportierten Sedimenten wurde verursacht durch die einzigartige Plattformbathymetrie und der Änderungen in den sedimentproduzierenden Gemeinschaft während des postglazialen Meeresspiegelanstiegs. Der Hartgrund wurde während des letzten glazialen Tiefstands gebildet, wohingegen der Packstone während des darauffolgenden Meeresspiegelanstiegs abgelagert wurde. Zeitgleich mit der Flutung der Plattform, wurden die Plattformränder von weitläufigen Halimeda-Wiesen besiedelt. Diese Wiesen sind die Quelle für feinkörniges Sediment das hauptsächlich aus Aragonitnadeln besteht. Diese Phase der Flutung ist in der Hangabfolge durch unverfestigte Sedimente mit Wackestone-Textur repräsentiert. Mit dem kontinuierlichen Anstieg des Meeresspiegels wurden auch die inneren Bereiche der Plattform überflutet. In diesen sehr flachen inneren Plattformbereichen etablierte sich eine Pellet-produzierende benthische Artenvergesellschaftung. Am Hang wurde ein peloidaler Packstone abgelagert, welcher durch eine Kornvergrößerungssequenz (*Coarsening upward*) und abnehmenden Aragonitgehalt charakterisiert ist. Die Wechsel in der sedimentären Hangabfolge legen nahe das Highstand shedding nicht als ein simpler An-Aus Mechanismus gesehen werden muss. Vielmehr kontrollieren lokale Faktoren, wie Plattformbathymetrie und die unterschiedlichen Sedimentproduzenten die Textur und Zusammensetzung der exportierten Sedimente.

Die tieferen Bereiche des leewärtigen Hanges der Großen Bahamas Bank werden in den reflektionsseismischen Daten als Seismische Sequenzen abgebildet, welche durch Meeresspiegelschwankungen dritter Ordnung produziert werden. Die Daten dokumentieren eine Strömungskontrolle auf den Hang, die in vorangegangenen Studie unterschätzt wurde. Der Einfluss der Strömung nimmt nach Norden hin zu und ist dort am Höchsten, wo die Konturströmung mit dem Floridastrom verschmilzt. Entlang Hangsegmenten mit hoher Strömungskontrolle formten Driftmigration und Strömungserosion ein tiefer Strömungsgraben. Dort, wird eine weitere Hangprogradation durch das Einschneiden von

Kanälen und die Akkumulation von riesigen Schüttungskomplexen (Mass transport complexes) verhindert. Weiter südlich, wo die Strömungskontrolle schwächer ist, werden Hangrutschungen und Kanalbildung hauptsächlich durch die Position des Meeresspiegels gesteuert. Große Rutschungen wurden durch Meeresspiegelschwankungen während der *Mid-Pleistocene transition* und des *Mid-Brunhes event* ausgelöst. Beide Perioden sind durch Änderungen in der Zyklizität und Amplitude der Meeresspiegelschwankungen gekennzeichnet. Die hochauflösenden hydroakustischen Daten zeigen fünf weitere Sequenzen in der spätpleistozänen Abfolge, diese wurden durch Meeresspiegelschwankungen vierter Ordnung geformt. Auch diese Sequenzen zeigen klare Unterschiede in der Strömungskontrolle. Zwei stochastische Modelle wurden entwickelt um den Einfluss der Hangmorphologie und Strömung auf die Faziesverteilung in den spätpleistozänen Sequenzen zu untersuchen. In Bereichen mit einem hohen Strömungseinfluss formt ein Zusammenspiel aus erosiven und konstruktiven Prozessen ein komplexes Faziesmuster mit Fazies-Wechseln entlang also auch zum Streichen des Hanges. In Hangbereichen mit geringer Strömungskontrolle finden Wechsel in der Fazies hauptsächlich in Richtung des Hanges statt. In Richtung des Hangstreichens sind die unterschiedlichen Fazies in Schichten angeordnet. Die Ergebnisse belasten etablierte Modelle für Karbonatplattformhänge durch die Bestimmung von Zeitpunkt und Auslöser von Hangrutschungen und Kanalinzisionen. Zusätzlich, wird gezeigt das Konturströmung ein unterschätzter Faktor für Sedimentation und Hangarchitektur ist.

## Table of Contents

<b>1. Chapter I: Introduction</b> .....	<b>15</b>
1.1 Carbonate platform slopes.....	15
1.2 Geological and oceanographic setting of the study area.....	17
1.3 Aim of the thesis.....	19
1.4 Outline of the thesis.....	20
<b>2. Chapter II: Sedimentary dynamics along carbonate slopes</b> .....	<b>23</b>
2.1 Outline of the chapter.....	23
2.2 Study area and oceanographic setting .....	23
2.3 Data and methods.....	25
2.4 Results.....	26
2.4.1 The slope morphology of the Great Bahama Bank.....	29
2.4.2 The slope morphology of Cay Sal Bank .....	33
2.4.3 Surface sediments.....	37
2.5 Interpretation and discussion .....	40
2.5.1 Contour current indicators.....	40
2.5.2 Depositional model.....	41
2.5.2.1 Great Bahama Bank: Sea-level lowstand.....	41
2.5.2.2 Great Bahama Bank: Sea-level rise and highstand.....	42
2.5.2.3 Cay Sal Bank: Sea-level lowering and lowstand.....	47
2.5.2.4 Cay Sal Bank: Sea-level rise and highstand .....	49
2.5.2.5 Tectonic control.....	51
<b>3. Chapter III: Sedimentary dynamics and high-frequency sequence stratigraphy of the southwestern slope of Great Bahama Bank</b> .....	<b>53</b>
3.1 Outline of the chapter.....	53
3.2 Geologic and oceanographic setting of the study area.....	53
3.3 Material and methods.....	55
3.3.1 Geophysical data.....	55
3.3.2 Bathymetric data.....	56

3.3.3	Stochastic facies modeling.....	56
3.4	Results.....	57
3.4.1	Major deposit types and general reflection pattern.....	57
3.4.2	Sequence stratigraphic framework.....	59
3.4.3	The seismic sequences.....	59
3.4.3.1	Sequence g.....	59
3.4.3.2	Sequence f.....	60
3.4.3.3	Sequence e.....	60
3.4.3.4	Sequence d.....	60
3.4.3.5	Sequence c.....	62
3.4.3.6	Sequence b.....	63
3.4.3.7	Sequence a.....	65
3.4.3.8	Stochastic models.....	65
3.5	Discussion.....	66
3.5.1	Slope development since the Late Miocene.....	66
3.5.1.1	Sequence g (8.4 Ma-5.5 Ma).....	66
3.5.1.2	Sequence f (5.5 Ma-3.8 Ma).....	68
3.5.1.3	Sequence e (3.8-3.1 Ma).....	69
3.5.1.4	Sequence d (3.1-2.0 Ma).....	70
3.5.1.5	Sequence c (2.0-0.6 Ma).....	70
3.5.1.6	Sequence b and a (0.6-0 Ma).....	75
3.5.1.6.1	Southern part of the study area.....	75
3.5.1.6.2	Northern part of the study area.....	76
3.5.1.6.3	Development of the recent platform margin.....	77
3.5.2	Facies distribution and heterogeneities along the leeward slope.....	79
3.5.3	The role of contour currents on the slope sedimentation along the leeward slope.....	82
<b>4.</b>	<b>Chapter IV: The Holocene slope succession of Great Bahama Bank; slope sedimentation in response to platform bathymetry and sediment producers.....</b>	<b>83</b>
4.1	Outline of the chapter.....	83

4.2	Platform morphology and environmental settings.....	83
4.3	Data and methods.....	84
4.4	Results.....	85
4.4.1	Core sites.....	85
4.4.2	Core M95-495.....	87
4.4.3	Core M95-577.....	88
4.5	Interpretation and discussion.....	91
4.5.1	Depositional geometry.....	91
4.5.2	Glacial/transgressional stage (sea level position: -125 m to -60 m).....	91
4.5.3	Early highstand stage (sea level position: -60 m to -5 m).....	92
4.5.4	Late highstand stage (sea level position: >-5 m).....	94
4.5.5	Implications for the highstand shedding .....	96
<b>5.</b>	<b>Chapter V: Conclusions.....</b>	<b>99</b>
	<b>References.....</b>	<b>103</b>
	<b>Acknowledgments.....</b>	<b>117</b>



## *Chapter I*

### **Introduction**

#### **1.1 Carbonate platform slopes**

Ancient and modern carbonate slopes provide key information about the adjoined carbonate factory and the factors controlling the platform growth (Eberli and Ginsburg, 1987; Betzler et al., 1999; Reolid et al., 2014). For example, carbonate slopes are excellent archives for sea-level fluctuations caused by both, the changes in the eustatic sea level and tectonic subsidence (Sarg, 1988; Eberli, 2000). Nevertheless, compared to siliclastic slopes, the sedimentary dynamics along carbonates slopes are poorly understood. This gap in knowledge can be attributed to the lack of continuous outcrops and the complex spatial heterogeneity of slope sediments, induced by a wide range of depositional and re-depositional processes (Playton et al., 2010). This heterogeneity makes the development of general depositional models and the prediction of lateral changes in facies or petrophysical properties challenging (Lucia, 1995). An improved understanding of the depositional processes along carbonate slopes is also important from an applied viewpoint, considering the interest in deep-water carbonates as hydrocarbon reservoir (Reijmer et al., 2015). Carbonate slopes are potential reservoirs or act as migration pathways from the basinal source rock to the reservoirs along the ancient platform margins. Examples for such hydrocarbon slope reservoirs are the Tengiz field (Kazakhstan) and the Poza Rica (Mexico), where large parts of the hydrocarbon production come from ancient slope deposits (Enos, 1985; Kenter et al., 2005; Janson et al., 2011; Collins et al., 2013).

Established models for carbonate platform slopes differentiate between erosional, bypass or accretionary slopes (Schlager and Ginsburg, 1981), and more recently between two end-members of carbonate slopes; accretionary or escarpment (bypass) (Playton et al., 2010). In addition, carbonate slope deposits were subdivided into grain and mud-dominated deposits to cover a wide spectrum of sedimentological heterogeneities, such as, for example, the sediment texture. With regard to the slope exposition to the wind regime, windward slopes show an aggradational geometry, whereas leeward slopes are characterized by the accretion of platform-derived neritic carbonates (Schlager and Ginsburg, 1981; Schlager and Camber, 1986; Playton et al., 2010).

In conventional sequence stratigraphic concepts, the sediment budget of carbonate slopes is influenced by the sea-level position (Droxler and Schlager, 1985; Schlager et al., 1994). During sea-level highstands, the platform top is occupied by a shallow-water carbonate factory, which exports sediment into the adjacent basins (Kendall and Schlager, 1981; Droxler et al., 1983). This process, termed highstand shedding, is seen as the main mechanism to form wedge-shaped sedimentary bodies along the slopes of Bahamian carbonate platforms (Droxler et al., 1983; Droxler and Schlager, 1985; Wilber et al., 1990; Schlager et al., 1994). Exported sediments are typically fine-grained and enriched in aragonite, which is primarily present as aragonite needles (< 5  $\mu\text{m}$ ) in the mud fraction (< 63  $\mu\text{m}$ ) (Schlager and James, 1979). The aragonite formed in the shallow-water realm has increased Strontium (Sr) concentrations compared to aragonite of pelagic origin (Boardman and Neumann, 1984). Two potential sources for aragonite needles were identified in the Bahamian region. The first is the spontaneous precipitation of aragonite during whitening events. Whitings are patches of milky water that occur in the calm platform interior and have been claimed to originate from direct precipitation of carbonate from the water column (Cloud, 1962). The second source is the calcareous algae *Halimeda*, which precipitates aragonite needles to stabilize their intercellular structures (Flügel, 2010; Gischler et al., 2013). During sea-level lowstands, the platform top is emerged and the sediment supply to the slope is limited and restricted to pelagic input (Kendall and Schlager, 1981; Schlager et al., 1994). This limited sediment supply favors early diagenetic formation of hardgrounds by the precipitation of marine cements (Malone et al., 2001; Eberli et al., 2002).

The geometry of carbonate slopes is related to the composition of the sediment produced on the platforms, and on the slope itself, as well as the amount of sediment bypassed to the basin (Schlager and Ginsburg, 1981). Because of this, compositional and depositional variability and the early submarine cementation, carbonate slopes can produce steeper slopes compared to slopes in siliciclastic settings (Schlager and Camber, 1986; Adams and Kenter, 2013). The detailed analysis of ancient and modern carbonate slopes show a relationship between the maximal slope angle and the sediment fabrics on the slope, in which the 'angle of repose' decreases with increasing mud content (Kenter et al., 1990). Where the slope angle exceeds the angle of repose; gravity-driven processes re-adjust the slope. Slope adjustments and gravity-driven processes are very common along carbonate slopes, and range from large mass transport complexes over the incision of channels and gullies to thin turbidite beds and offbank-transported mud during highstand shedding (Betzler et al., 1999; Bernet et al., 2000; Puga-Bernabéu et al., 2011; Mulder et al., 2012; Jo et al., 2015; Principaud et al., 2015, Wunsch et al., 2016). Recent studies show that bottom

and contour currents, which flow along the slopes, are an important controlling factor of slope geometry and sediment distribution (Betzler et al. 2014; Wunsch et al., 2016). In particular, Betzler et al. (2014) show how contour currents sculpt the present day slope of Great Bahama Bank as a periplatform drift, in which the contour currents winnow sediments from the toe of slope and redistribute the platform export.

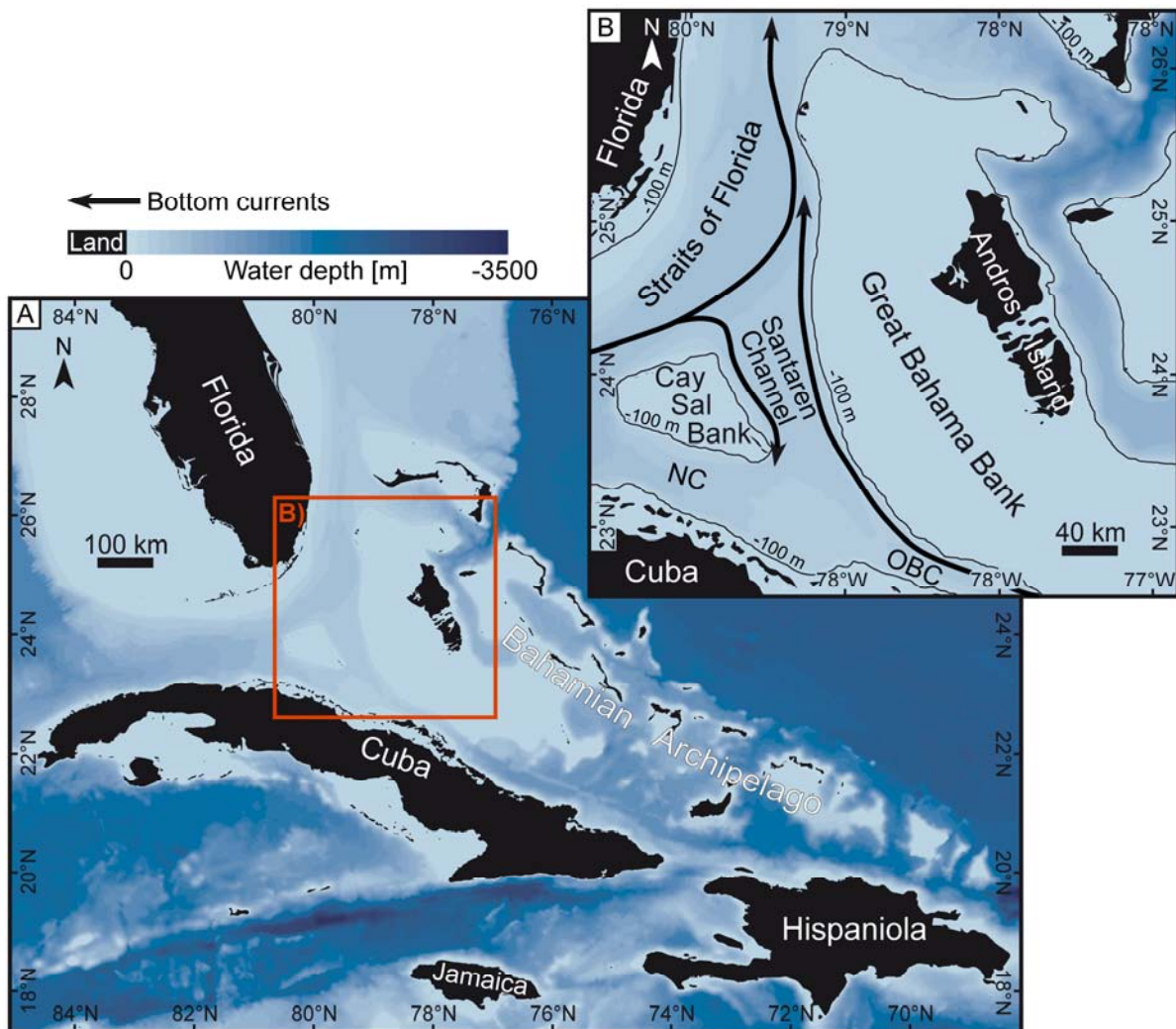


**Fig. 1.1:** **A:** Location map of the Bahamian archipelago. Red box indicates the outlines of the study area shown in B. **B:** Close view of the study area within the Santaren Channel. Arrows indicates the directions of the main bottom currents. Current data after Lee et al. (1995); Leaman et al. (1995); Chérubin (2014); Lüdmann et al. (2016). NC = Nicholas Channel; OBC = Old Bahama Channel

## 1.2. Geological and oceanographic setting of the study area

The Bahamian archipelago is located between 20° and 28° N and 72° and 80° W and contains numerous isolated carbonate platforms (Fig. 1.1A). The Bahamas have a subtropical, humid marine climate with an annual average air temperature of 25°C (Bergman et al., 2010). The average yearly rainfall is 857 mm with regional variations (Bosart and Schwartz, 1979). Seasons are characterized by warm, wet summers and cooler,

dry winters (Gebelein 1974). The Great Bahama Bank (GBB) is the largest platform of the archipelago and the largest carbonate platform in the world (Fig. 1.1B) (Bergman et al., 2010). The vertical thickness of GBB's carbonate succession exceeds 5 km (Meyerhoff and Hatten, 1974). The Doubloon Saxon-1 well, which was drilled on the south-western part of the platform bottomed out in Lower Cretaceous carbonates in more than 6 km of depth (Wallis, 1993). The modern topography of GBB is the result of repeated tectonic segmentation and coalescence of a Cretaceous megabank (Eberli and Ginsburg, 1987; 1989). The tectonic segmentation is related to rifting and reactivation of Jurassic faults during the Middle Cretaceous to Middle Tertiary, induced by the collision of the North American plate with the Cuban arch (Ladd and Sheridan, 1987; Masafarro and Eberli, 1999; Masafarro et al., 1999). During the Neogene, several of these smaller platforms coalesced by basinal aggradation, platform progradation and seaway filling formed the modern Great Bahama Bank (Fig. 1.2) (Eberli and Ginsburg, 1987; Eberli et al., 1994). Seismic data show that in both, the Straits of Andros and the Straits of Florida, a phase of basin and slope aggradation preceded the platform progradation. The initial basin was filled by aggrading wedge-shaped bodies, which indicate a higher sedimentation rate in the basin axis than along the platform flanks (Eberli and Ginsburg, 1987; Eberli et al., 1994). The subsequent progradation occurred in pulses and is visible in the seismic data as a succession of prograding, sigmoidal shaped sediment packages (Eberli and Ginsburg, 1989) (Fig. 1.2). Since the Miocene, the leeward margin of GBB prograded 25 km towards the west (Eberli and Ginsburg, 1987). During this progradation a change of the depositional relief from a ramp to a flat-topped platform with a steeper margin occurred in the Pliocene (Fig. 1.2) (Betzler et al., 1999).

The bottom current system around the Bahamian archipelago is dominated by the North Atlantic gyre to the east of the Bahamas and by the Florida Current (FC) to the west (Chérubin, 2014). The FC is composed of water masses from the Gulf of Mexico and the Caribbean Sea (Schmitz and Richardson, 1991). It passes the Straits of Florida and becomes a major part of the Gulf Stream, the surface-flowing limb of the North Atlantic gyre. The transport rate of the FC varies on inter-annual timescales and is reduced during glacial times (Schott et al., 1988; Lynch-Stieglitz et al., 1999). Along the northern side of Cay Sal Bank (CSB), the FC meanders and forms cyclonic frontal eddies. These eddies force a part of the FC to bend southwards into the Santaren Channel (SC) that flows as contour currents along the slope of CSB (Lee et al., 1995). The SC is a 65 km wide and 750 m deep water area between GBB and CSB, which connects the Straits of Florida with the Old Bahama Channel. The eastern part of the SC is dominated by strong north-directed contour currents,

which flow along the leeward slope of GBB (Leaman et al., 1995). This north flowing currents merge with the FC at the coalescence of the Santaren Channel with the Straits of Florida (Fig. 1.1B). The surface currents system is formed by a complex interaction between ocean and wind-driven currents, which results in a prevailing west to northwest-directed surface current in the study area (Wang and Mooers, 1997; Kourafalou and Kang, 2012). The surface currents are responsible for the distribution of sediments and the prevailing off-bank transport to the western leeward side of Bahamian carbonate platforms (Hine et al., 1981; Hine and Steinmetz, 1984). Tidal regimes in the Bahamas are semidiurnal and microtidal with a mean range of ca 0.7 m (Bergman et al., 2010).

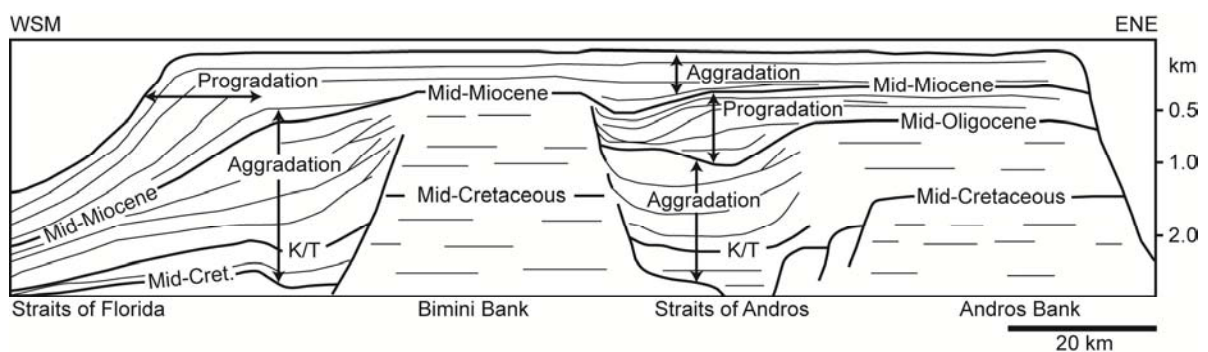


**Fig. 1.2:** Interpretation of seismic section through Great Bahama Bank displaying the complicated internal architecture of the bank. Modified after Eberli and Ginsburg (1989); Eberli et al. (1994).

### 1.3 Aim of the thesis

This thesis aims on providing new genetic models on carbonate slope architecture and on unraveling the related sedimentary processes and controlling factors. Another objective is to determine the influence of bottom currents on the sedimentation pattern and the geometry of carbonate slopes. To achieve these goals geophysical (hydroacoustic and reflection seismic data) and sedimentological data (gravity cores and grab samples) were combined with the existing stratigraphical and sedimentological core data based on ODP leg 166. The results question established models for carbonate slopes by determining timing and trigger mechanisms of slope failure and highlights the bottom currents as underestimated driver for slope deposition.

## 1.4 Outline of the thesis

Beside the Introduction (Chapter I) and the summarizing conclusions (Chapter V), the thesis subdivides into three thematic complexes (Chapter II to IV).

*Chapter II* compares the windward slope of Cay Sal Bank with the leeward slope of Great Bahama Bank. The chapter emphasizes the diversity and complexity of the slope morphology and the sediment distribution of the youngest sequence, which developed since the last glacial maximum. The results document a complex interplay of depositional and erosional processes on both slopes through time and provides new insight into the current regime and its influence on slope architecture and sedimentary processes. The processes triggering slope failures and the formation of channels, gullies and furrows differ on both slopes. At the windward slope of Cay Sal Bank, the local tectonic regime and winnowing by contour currents are responsible for slope failures and the incision of large channels. At the leeward slope of the Great Bahama Bank, extensive slope failures occurred during the sea-level lowering after the last interglacial. The resulting slope morphology channelized the exported platform sediments during the subsequent sea-level rise and highstand. This chapter is based on the published manuscript “Sedimentary dynamics along carbonate slopes (Bahamas archipelago)” by Wunsch et al. (*Sedimentology*, 2016).

*Chapter III* shows that the erosional and depositional processes encountered in the youngest sequence (Chapter II) also acted along the leeward slope of Great Bahama Bank during the older sequences. Newly acquired reflection seismic data were linked with the existing seismic stratigraphy and the sedimentological data provided by ODP Leg 166. The data document an intensified current control on the leeward slope since the Late Miocene. However, the influence of the contour currents on the slope strengthens from south to north. It is shown that along slope segments with high current influence, current winnowing oversteepened the toe of slope and favors the incision of channels and large slope failures. In contrast, along slope segments with weaker current influence, slope failures are controlled by the position of the sea-level. Based on the hydroacoustic data, four higher order sequences were identified within the existing seismic stratigraphic framework of third order seismic sequences. In addition, two stochastic facies models were developed to reveal the influence of the slope morphology and currents on the sedimentation pattern and hence on the facies distribution. This chapter is based on the published manuscript entitled “Sedimentary Dynamics and High-Frequency Sequence Stratigraphy of the Slope of Great Bahama Bank” by Wunsch et al. (*Sedimentary Geology*, 2018).

*Chapter IV* focuses on the flooding history of Great Bahama Bank after the last glacial maximum. Two gravity cores from the platform slopes were analyzed for sediment composition and grain-size distribution. The sedimentary succession results from a complex interplay of postglacial sea-level rise, platform morphology and sediment-producing organisms. The results of this chapter challenge the established models of highstand shedding and demonstrate that the sediment export from platform tops during sea level highstands is not a simple on-off mechanism. During the early flooding of Great Bahama Bank, the leeward margin areas were colonized by dense meadows of the calcareous algae *Halimeda*. These *Halimeda* meadows produced a vast amount of aragonite needles, which deposited on the slope as fine-grained and aragonite-rich sediments with a wackestone texture. Later, with the successively flooding of the platform interior and the establishment of a pellet-producing benthic community of the platform interior, the mode/type platform export changed. The exported sediments show a coarsening through time accompanied by a decrease in aragonite content. This change in the sediment composition implies that the platform export (grain-size, components) is not only controlled by global factors (sea-level position, solar insolation) but rather by local factors like the platform bathymetry or sediment-producing communities.



## *Chapter II*

# **Sedimentary dynamics along carbonate slopes**

### **2.1 Outline of the chapter**

The reconstruction of the sedimentary processes along carbonate platform slopes is an ongoing research field, because the full complexity of these systems is yet not fully understood (Playton et al., 2010; Reijmer et al., 2015). Studying the youngest slope sedimentation captured by sea floor and subsurface data with the modern current pattern and the sea-level fluctuation can provide many new insights into the sedimentary processes and their depositional products. Under this premise, this chapter used hydroacoustic and sedimentological data covering two Bahamian carbonate slopes. The data emphasizes the diversity and complexity of the slope morphology and the sediment distribution of the youngest high-frequency sequence, which has developed since the last glacial maximum. The chapter documents a complex interplay between depositional and erosive processes on both slopes through time and provides information on the current regime and its influence on the slope sedimentary processes.

### **2.2 Study area and oceanographic setting**

The Bahamian archipelago is situated between 20° and 28°N and 72° and 80°W and contains numerous isolated carbonate platforms (Fig. 2.1A). The study area is located in the Santaren Channel (Fig. 2.1B), an up to 700 m deep and 65 km wide strait, which connects the Florida Straits with the Old Bahama Channel. To the west, the Santaren Channel is bordered by the windward margin of the Cay Sal Bank (CSB), and to the east by the leeward margin of the Great Bahama Bank (GBB). The GBB is a flat-topped carbonate platform with an average water depth of 10 m and an area of almost 100 000 km<sup>2</sup> (Boss and Rasmussen, 1995; Harris et al., 2015). The CSB is a smaller (6000 km<sup>2</sup>) carbonate platform with a platform top beneath a water depth of 10 m (Purkis et al., 2014). The platform margins are at water depths of 15 to 30 m (Hine and Steinmetz, 1984; Purkis et al., 2014).

The morphology of the Bahamian archipelago is the result of repeated tectonic segmentation that started during the middle Cretaceous and formed several small platforms and deep-water re-entrants (Eberli and Ginsburg, 1987; Ladd and Sheridan, 1987; Masferro and Eberli, 1999). A number of these smaller platforms coalesced to form the GBB (Eberli and Ginsburg, 1987, 1989). Ball et al. (1987) proposed that the shape of the leeward margin

indicates a strong imprint of the Florida Current on slope sedimentation by inhibiting slope progradation. However, since the late Middle Miocene the leeward platform margin prograded 25 km to the west (Eberli and Ginsburg, 1987). Variations in the rate of progradation and thus the architecture of the platform are linked to amplitude and duration of sea-level changes. Cores from Ocean Drilling Program (ODP) Leg 166 retrieved along the western GBB show that the sedimentation at the leeward slope occurs primarily during sea-level highstands by the deposition of platform-derived material (Eberli, 2000). By contrast, sea-level lowstands are represented by reduced sedimentation rates, early cementation and the formation of hardgrounds (Malone et al., 2001; Eberli et al., 2002).

On average, the CSB has a 5 m deeper platform top than the GBB with limited reef development (Goldberg, 1983), no active sand shoals, no tidal flats, a thin to non-existent sedimentary cover, and a relatively deep margin and lagoon system (Hine and Steinmetz, 1984). The platform top shows evidence for karstification during sea-level lowstands (Purkis et al., 2014). The main sediment export from CSB occurs over the western leeward slope (Hine and Steinmetz, 1984; Purkis et al., 2014). Because of the lowered platform top, the CSB is considered ‘partially drowned’ (Hine and Steinmetz, 1984) but the seagrass covered platform interior is similar in composition as GBB (Purkis et al., 2014). There is evidence that CSB is underlain by a fault system rooted in an anticlinal structure formed during the Cuban orogeny that is potentially still active today (Masferro, 1997; Masferro et al., 1999). These structures follow the general north-west/south-east trend of the Cuban Fault and Thrust Belt and the Santaren anticline (Masferro, 1997; Masferro et al., 1999, 2002; Kula, 2014). One of the faults just north of CSB breaks the sea floor, documenting local neo-tectonic activity. Orthogonal scars and channels along the eastern side of CSB might also be caused by probably older faults (Kula, 2014).

The recent current system around the Bahamian archipelago (Fig. 2.1A) is dominated by the North Atlantic gyre to the east of the Bahamas and by the Florida Current (FC) to the west (Bergman et al., 2010). The FC is composed of water masses from the Gulf of Mexico and the Caribbean Sea (Schmitz and Richardson, 1991). It passes the Straits of Florida and becomes a major part of the Gulf Stream, the surface-flowing limb of the North Atlantic gyre. The transport rate of the FC varies on inter-annual and seasonal timescales (Schott et al., 1988). Based on oxygen-isotope data, Lynch-Stieglitz et al. (1999) proposed a reduced northward flow of water masses through the Florida Straits during the last glacial maximum (LGM). The local current regime within the Santaren Channel is influenced by the FC and the current within the Old Bahama Channel (Fig. 2.1A). The FC passes along the northern side of CSB. In this area, the FC meanders and forms cyclonic frontal eddies. These eddies

force a part of the current to bend southward into the Santaren Channel (Lee et al., 1995). Currents flow as contour currents along the windward slope of CSB, while the eastern part of the Santaren Channel is dominated by a northward-directed contour current that flows from the Old Bahama Channel along the leeward slope of GBB (Leaman et al., 1995). In short, the surface current system within the Santaren Channel has a complex pattern, which results from the interaction of ocean and trade-wind-driven currents. Numerical models indicate a prevailing west to north-west-directed surface current (Wang and Mooers, 1997; Kourafalou and Kang, 2012). On the platform top of the GBB and CSB trade-wind-induced surface currents are responsible for the distribution of sediments and the prevailing off-bank transport to the western leeward side of the banks (Hine and Steinmetz, 1984; Purkis et al., 2014). Tidal regimes in the Bahamas are semidiurnal and microtidal with a mean range of ca 0.7 m (Bergman et al., 2010).

### **2.3 Data and methods**

This study combines sediment surface samples and data of sub-bottom profiles, reflection seismics and multibeam bathymetry. High-resolution sub-bottom data were recorded during R/V Meteor cruise M95 CICARB with a parametric sediment echosounder (PARASOUND P70; Atlas Elektronik, Bremen, Germany). The system was operated with two frequencies (18 kHz and 22 kHz). The software PS32segy (Hanno Keil, University of Bremen, Germany) was used to cut and convert the data. Data processing was performed with the software package ReflexW (Sandmeier Software, Karlsruhe, Germany), comprising automatic gain control and amplitude normalization along the profile. Long profiles were subjected to trace stacking in order to reduce the data volume.

Reflection seismic data were recorded with a 144-channel digital streamer with an active length of 600 m (Hydroscience Technologies Inc., Mineral Wells, TX, USA). The seismic array consisted of a standard and a mini GI gun (Sercel, Houston, TX, USA) with a total volume of 3.2 l, ran at 150 to 180 bar. The shot interval was 12.5 m at a survey speed of 5 kn. Data were processed using ProMax (Halliburton-Landmark, Houston, TX, USA) to zero phase, filtered in time and f-k domain, and corrected for dip and normal moveout. For stacking, a bin size of 6.25 m was selected. Finally, migration in time domain was carried out. For visualization and interpretation, sub-bottom and seismic data were loaded into Petrel E&P (Schlumberger, London, UK).

Bathymetric data were recorded with the hull-mounted Multibeam system EM122 (Kongsberg Maritime, Kongsberg, Norway), which uses a sonar frequency of 12 kHz, 432 beams and 864 soundings per ping. The system was operated with 140° sector coverage and

equidistant sounding spacing. Beams were stabilized for roll, pitch and yaw. The software Caris HIPS & SIPS (Caris, Fredericton, Canada) was used for data processing and gridding (7.5 m cell size). Backscatter intensities were processed to estimate the acoustic properties of the surface sediments. Where the near-surface sediment sound velocity is close to the sound velocity of the overlying water column; the acoustic pulse penetrates the sediments and is scattered back by subsurface reflectors. Consequently, the recorded data do not show the real backscatter intensities of the sea floor. This leads to an adulteration of the recorded backscatter intensities (Blondel, 2009). The backscatter intensities were draped as a sonar mosaic onto the bathymetric grids for visualization. The software package Fledermaus (QPS, Zeist, The Netherlands) was used for data visualization and interpretation.

Surface sediment samples were collected to determine the sediment type. Samples were wet sieved and analysed for grain-size spectrum and composition. Grain-size statistics are based on the graphical method (Folk and Ward, 1957) and were calculated using GRADISTAT (Blott and Pye, 2001). The sediment texture was determined by the microscopic analysis of thin sections and smear slides and classified after Dunham (1962).

## **2.4 Results**

Within the entire study area, the subsurface data show a series of high-amplitude reflections separating intervals with a transparent reflection pattern. Correlation of hydroacoustic data with ODP Leg 166 core data (Fig. 2.2A-C) confirms that the uppermost of these reflections corresponds to the cemented interval of the high-frequency sequence boundary S (SB S), which formed during the last sea-level lowstand (Eberli et al., 1997; Malone et al., 2001; Betzler et al., 2014). Radiocarbon dating yielded an age of 42.7 kyr cal BP for SB S at ODP site 1009 and younger than 10 kyr cal BP for the sediments overlaying SB S (Slowey et al., 2002), which indicates a hiatus of ca 30 kyr. These ages are supported by oxygen-isotope data of ODP core 1009, which indicate that the sediments above SB S are deposited during marine isotope stage (MIS) 1 (Malone, 2000; Slowey et al., 2002). The following descriptions of sedimentological and stratigraphical data refer to the interval delimited by sequence boundary S and the sea floor. Along the leeward slope of GBB, this sequence is up to 56 m thick, whereas it reaches a maximum of 10 m at the windward slope of the CSB.

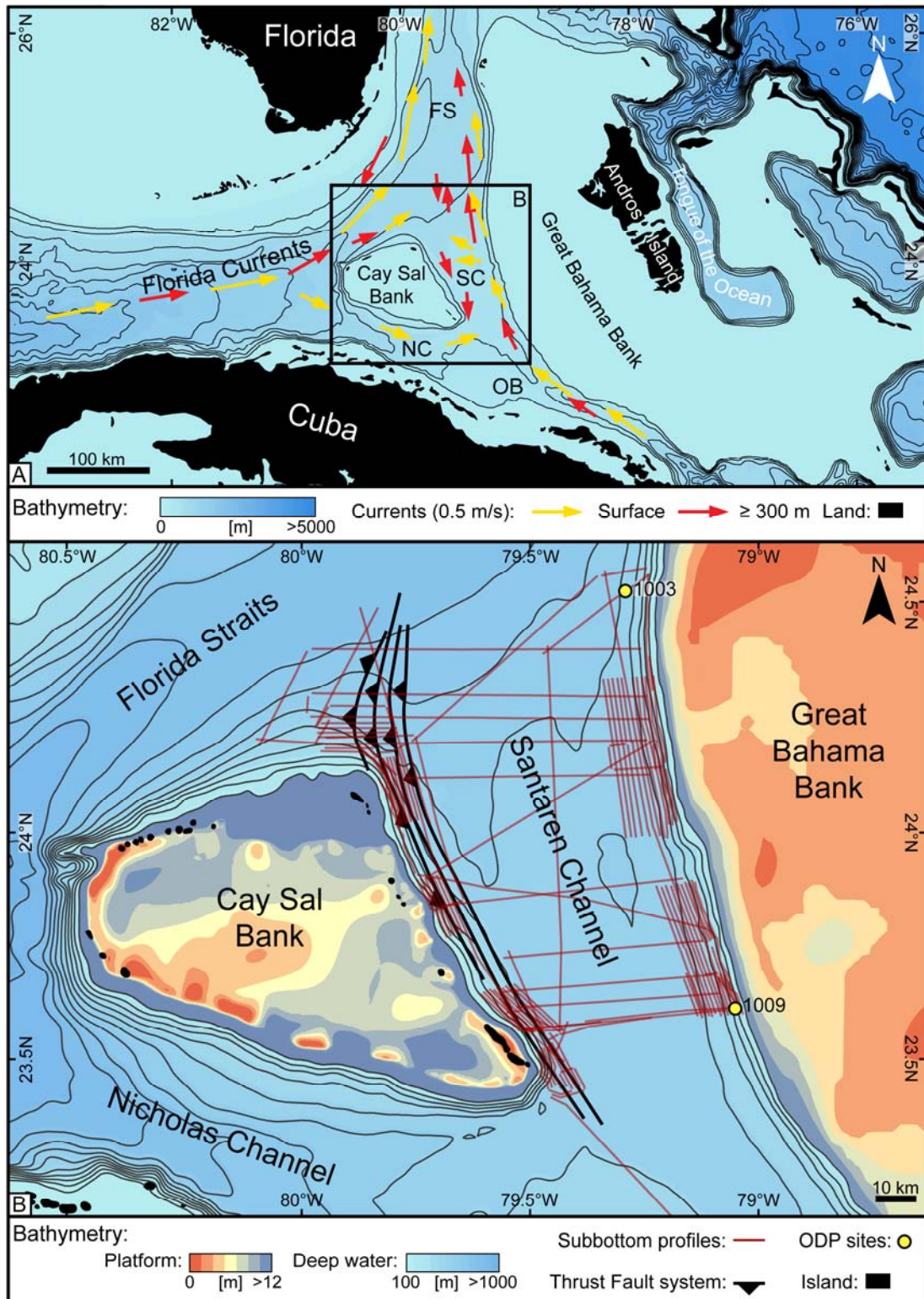


**Fig. 2.1:** A: Location map of the Bahamian archipelago. The prevailing current directions within the Florida Straits (FS), the Santaren Channel (SC), the Old Bahama Channel (OB) and the Nicholas Channel (NC) are marked with arrows. Red arrows indicate bottom currents, and yellow arrows indicate surface and near-surface currents. Current data after Leaman et al. (1995); Bergman et al. (2010); Lüdmann et al. (2016); Wang and Moers (1997); Kourafalou and Kang (2012); Chérubin (2014). The box shows the outline of the study area shown in B. B: Close view of the study area within the Santaren Channel. Red lines indicate the positions of the subsurface profiles. The locations of site 1003 and 1009 of ODP leg 166 are marked with points in yellow. Position of the thrust fault system after Kula (2014).

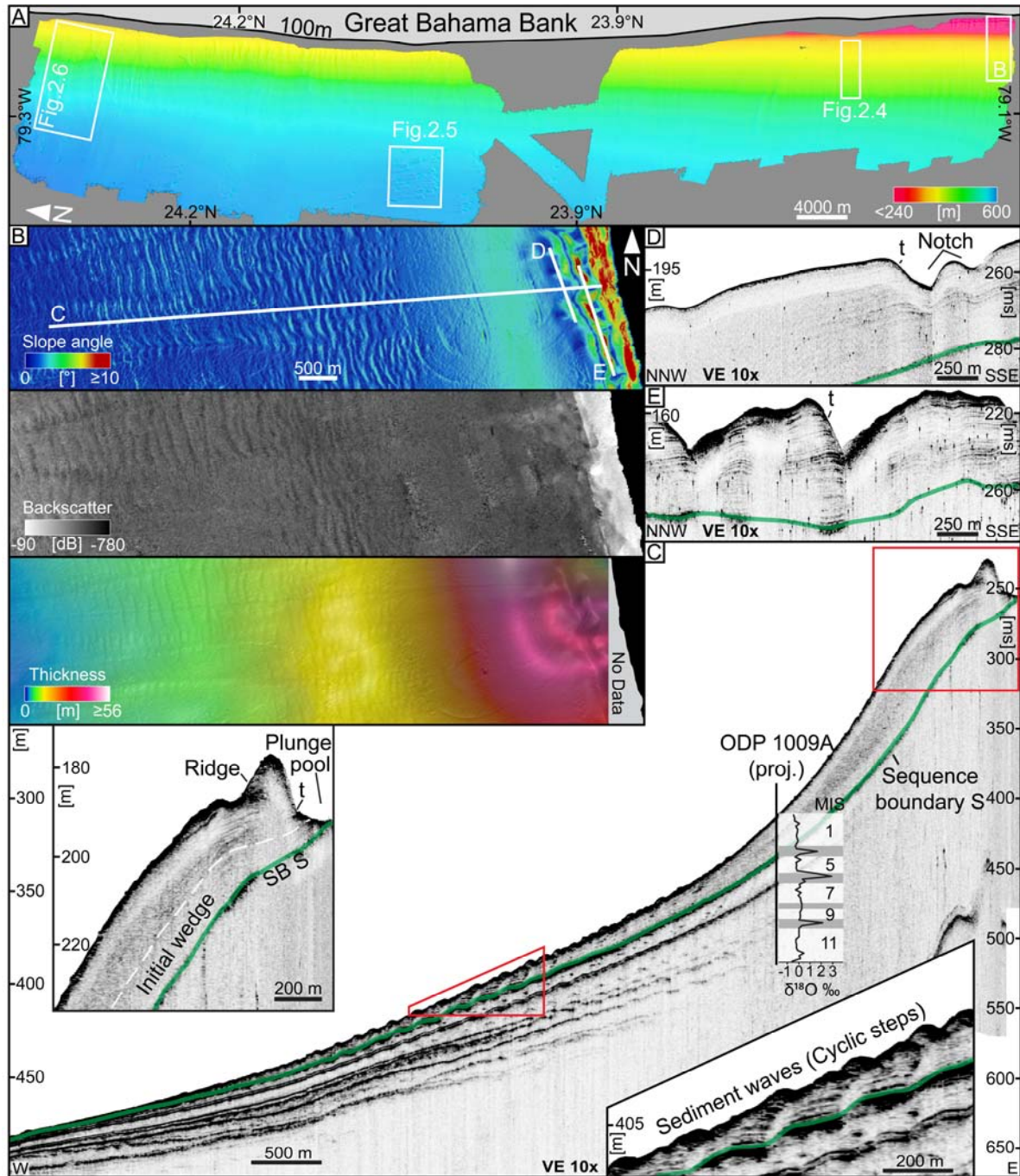


**Fig. 2.2:** **A:** Multibeam bathymetry of the leeward slope of the Great Bahama Bank. White rectangles indicate the positions of B and Figs 2.4 to 2.6. **B:** Detailed multibeam bathymetry, slope-angle steepness map, backscatter image and thickness map of the deposits overlying Sequence Boundary S (SB S). White lines indicate the positions of the cross-sections in C to E. **C:** The subsurface profile shows sedimentary structures and thickness variations of the youngest sequence on the southern part of the leeward slope. The youngest sequence forms a wedge, which onlaps the slope at a water depth of 160 m (modified after Betzler et al., 2014). The lower boundary is formed by SB S in the succession of ODP Site 1009 (Eberli et al., 1997). The  $\delta^{18}\text{O}$ -data of ODP site 1009 indicate the Holocene age of the wedge (Data: Malone, 2000). Insets in C show detailed views of the succession of cyclic steps, the plunge pool and the adjoining ridge. The internal reflections of the wedge are truncated (t) within the floor of the plunge pool. **D:** Subsurface profile of the margin-parallel ridge. The reflections are truncated (t) at the position of the notches. The green line indicates SB S. **E:** The bottom of the plunge pool is irregular. The reflections are partly truncated (t). The green line indicates SB S.

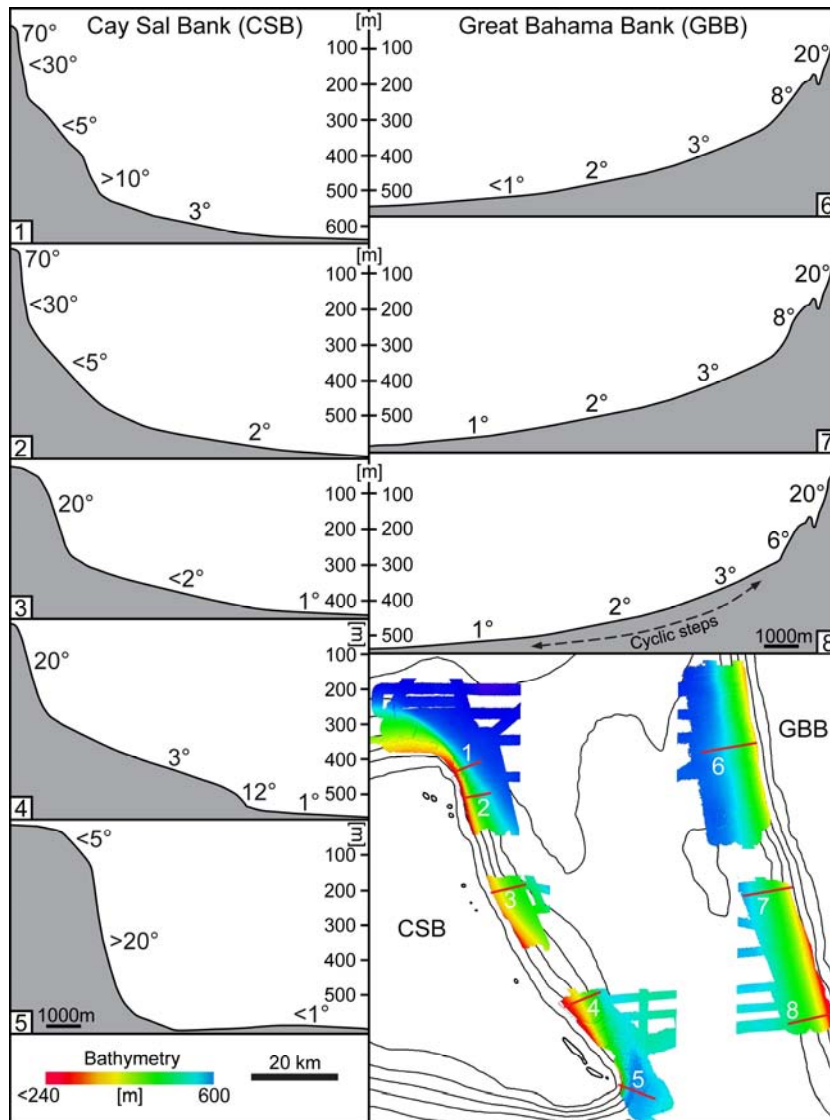


**Fig. 2.3:** Compilation of slope profiles from the windward slope of the Cay Sal Bank and the leeward slope of the Great Bahama Bank. Positions of the profiles are marked in the map. All slope profiles have a vertical exaggeration of 10.

#### 2.4.1 The slope morphology of the Great Bahama Bank

Review and study of the data resulted in the identification of the following morphological features: a margin-parallel depression with an adjoined ridge at the proximal part of a sedimentary wedge, which is partly covered by sediment waves and dissected by shallow furrows. Fields of mounds and blocks, and a system of gullies and scarps are located in the northern part of the leeward slope. These features will be described and documented in detail in the following paragraphs.

The general shape and configuration of the slope is illustrated in Fig. 2.2A. The platform breaks into the slope at ca 40 to 50 m. The uppermost slope is a steep submarine cliff (Wilber et al., 1990), which flattens basinward to 20°. At the base of the cliff the slope is lined by an up to 300 m wide and partly more than 35 m deep margin-parallel depression that is bordered basinward by a ridge. This ridge is dissected by V-shaped notches

(Fig. 2.2B; D). Both structures line the entire leeward slope of the GBB (Wilber et al., 1990). Wilber et al. (1993) described this depression as an erosional trough, similar to a plunge pool. The subsurface data illustrate that the sequence overlaying SB S is formed by a sedimentary wedge, which onlaps the slope at a water depth of 160 m and thins out ca 7 km away from the platform margin (Fig. 2.2C). In its most proximal part, the wedge is characterized by faintly parallel reflections that turn distally into a transparent reflection pattern, which thins out below stacked convex reflections of high to medium amplitude at a water depth of ca 330 m (Fig. 2.2C). The internal reflection pattern of the margin-parallel ridge consists of parallel to subparallel reflections of medium amplitude, which are truncated where the notches occur (Fig. 2.2D). The floor of the plunge pool is undulated; the subsurface data show parallel to subparallel reflections of medium amplitude (Fig. 2.2E).

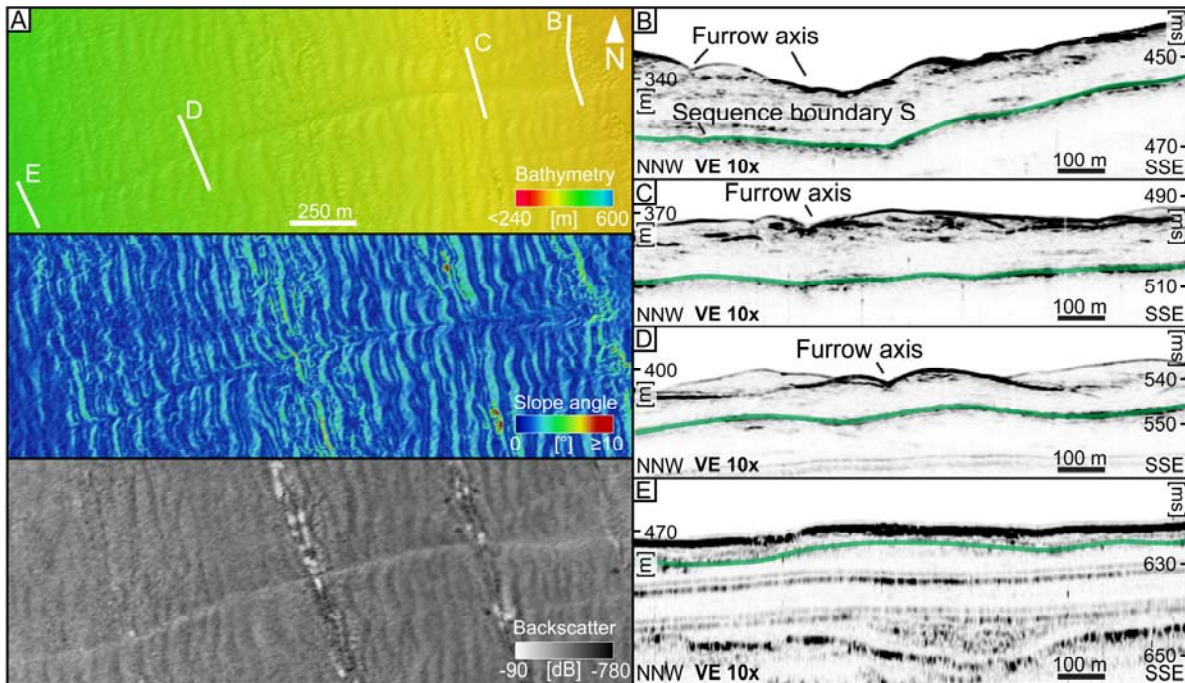


**Fig. 2.4:** Southern part of the leeward slope of Great Bahama Bank showing a shallow furrow cutting into a field of cyclic steps. For location see Fig. 2.2A. The green line indicates Sequence Boundary S. **A:** Multibeam bathymetry, slope angle-steepness map, and backscatter image of the furrow area. White lines indicate the positions of the cross-sections in B to E. **B to E:** Cross-sections of the furrow that runs perpendicular to the axis at water depths of 340 m, 370 m, 400 m and 470 m, respectively.

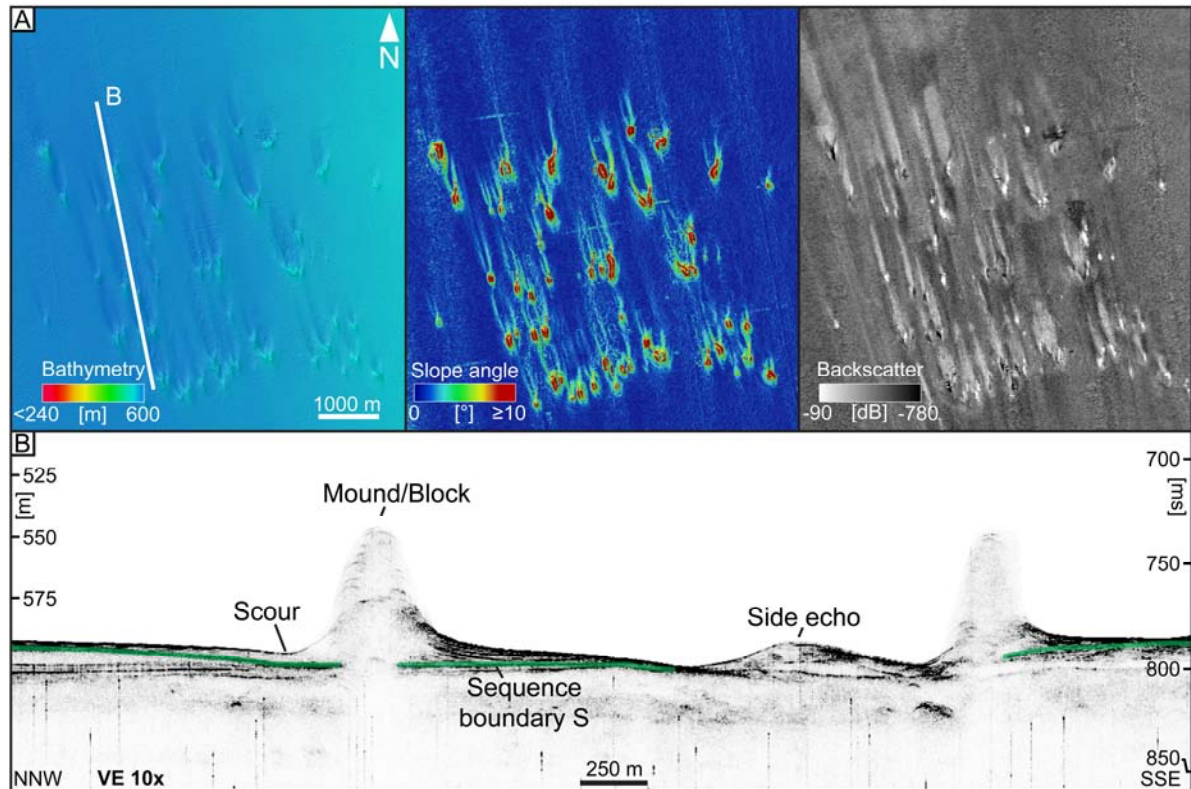


**Fig. 2.5:** Field of mounds and blocks at a water depth of ca 600 m. See Fig. 2.2A for location, the green line indicates Sequence Boundary S. **A:** Multibeam bathymetry, slope-angle steepness map and backscatter image of the area. White line indicates the cross-section in B. The mounds are up to 25 m high and have an elongated shape. Their downcurrent terminations are formed by elongated scours, which point to the north-west. **B:** The blocks and mounds appear as acoustically hard without internal reflections.

In the southern part of the GBB slope, the sedimentary wedge has slope angles of 6 to 8° that flatten to 3° towards the axis of the Santaren Channel (Fig. 2.3). This part of the sea floor is dominated by a field of sediment waves, which disappear at a water depth of 550 m, where the slope angle decreases to 1° and less (Fig. 2.3). These bedforms are up to 3 m high with wavelengths of ca 120 m. Downslope, V-shaped furrows dissect the crests of the sediment waves (Fig. 2.4A). These furrows appear at a water depth of 350 m and terminate at a depth of 530 m, where the slope angle is less than 2°. The internal reflection pattern of the flanks and base of the furrows is diffuse, and their most distal part is characterized by subparallel reflections of medium to low amplitude (Fig. 2.4B-E).

Towards the north (Fig. 2.2A), the slope is characterized by a strike-discontinuous distribution of morphological features and bedforms. These comprise mounds and blocks at the distal part and gullies and scarps on the proximal slope. Fields of mounds and blocks are located at the toe of slope at a water depth of ca 600 m. The blocks and mounds are up to 25 m high and elongated parallel to the current direction (Fig. 2.5A). Their downcurrent

terminations are formed by elongated scours that point to the north/north-west. In the subsurface data, the blocks and mounds partly appear as acoustically hard, but show parallel internal reflections in the upper part (Fig. 2.5B).

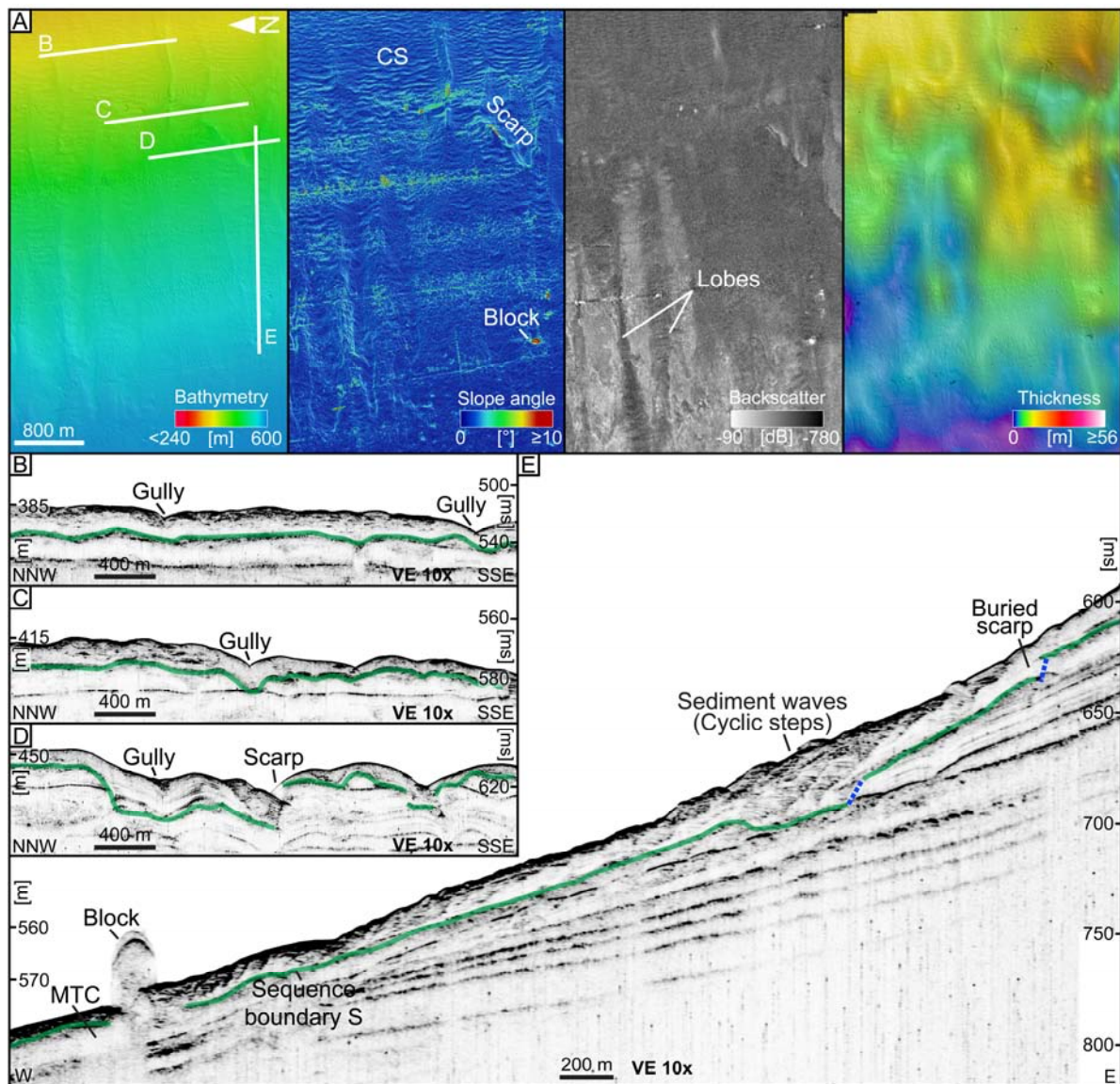


**Fig. 2.6:** Northern part of the leeward slope of Great Bahama Bank with a gully and scarp system leading to a complex slope morphology. See Fig. 2.2A for location, the green line indicates Sequence Boundary S. **A:** Multibeam bathymetry, slope-angle steepness map, backscatter image and thickness map of the Holocene sediments. White lines indicate the positions of the cross-sections provided in B to E. **B to D:** Cross-sections of the gully that runs perpendicular to the axis at water depths of 390 m, 430 m and 450 m, respectively. **E:** The slope-parallel profile shows the sedimentary structures and the thickness variations of the youngest sequence across a buried scarp. The area beneath the scarp is occupied by cyclic steps (CS).

Gullies and scarps dominate the slope morphology in the northern part of the investigated area (Fig. 2.6A). The upslope terminations of the gullies are located at a water depth of ca 370 m, while the downslope terminations are all at the same water depth of 450 m. Gullies are 180 to 550 m wide, with a depth of 2 to 15 m. The reflection pattern within the gully flanks consists of discontinuous reflections of high amplitudes in the upper part and of subparallel reflections of low to medium amplitude in the lower part (Fig. 2.6B-C). The gully axes cut into the underlying stratigraphic level, which is visible in the subsurface data as 'cut and fill' structures (Fig. 2.6C; D). In the gully axes, medium to high-amplitude chaotic reflections in the proximal change to transparent reflections in distal part (Fig. 2.6 B-D). At the downslope terminations of the gullies, tongue-shaped and up to 500 m wide lobes and scarps appear (Fig. 2.6A). The surface of the lobes is covered with sediment waves. The internal reflection pattern is characterized by stacked convex reflections of high to medium amplitude (Fig. 2.6E). Locally, the lower part of the lobes is imaged with a transparent reflection pattern, which is overlain by stacked convex reflections of high to medium amplitude (Fig. 2.6E).

#### **2.4.2 The slope morphology of Cay Sal Bank**

The following morphological features were identified along the slope of Cay Sal Bank (CSB): fields of mounds fringing the upper slope, dendritic channels, a zigzag shaped step in the sea floor, and furrows that are separated by sediment ridges. Towards the south, the slope is intersected by channels and the toe of slope is occupied by fields of blocks and mounds. These features will be described in detail in the following paragraphs.

In plan view, the windward platform margin of CSB has a concave shape (Fig. 2.7A). The platform edge of the bank is located at a water depth of 50 m (Fig. 2.7B), and the upper 70 m of the slope are formed by a submarine cliff dipping at 70° (Fig. 2.3). At the base of this cliff, at a water depth of 120 to 140 m, several mound-shaped structures occur. These up to 12 m high structures are imaged in the subsurface data as high-amplitude convex reflections (Fig. 2.7B). At a water depth of 240 m, where the slope angle decreases from 30° to less than 5°, there is a further field of mound-shaped structures (Fig. 2.7C). These structures are up to 10 m high with shapes varying from circular to slightly elliptic. In the subsurface data, these structures are imaged as high-amplitude convex reflections (Fig. 2.7B). The space in between these mound-shaped structures is occupied by a sediment wedge, imaged with a diffuse reflection pattern (Fig. 2.7B).

Downslope of the blocks, there are large variations in slope angle, but in general the slope steepens towards the southern and northern ends of the eastern flank of CSB (Fig. 2.3). The lowest slope angles are measured in the centre of the concave flank (2 to 3°); the southern part has slope angles of up to 20°, whereas the northern part shows slope angles up to 5° accompanied by a steep toe of slope (>10°) (Fig. 2.3).

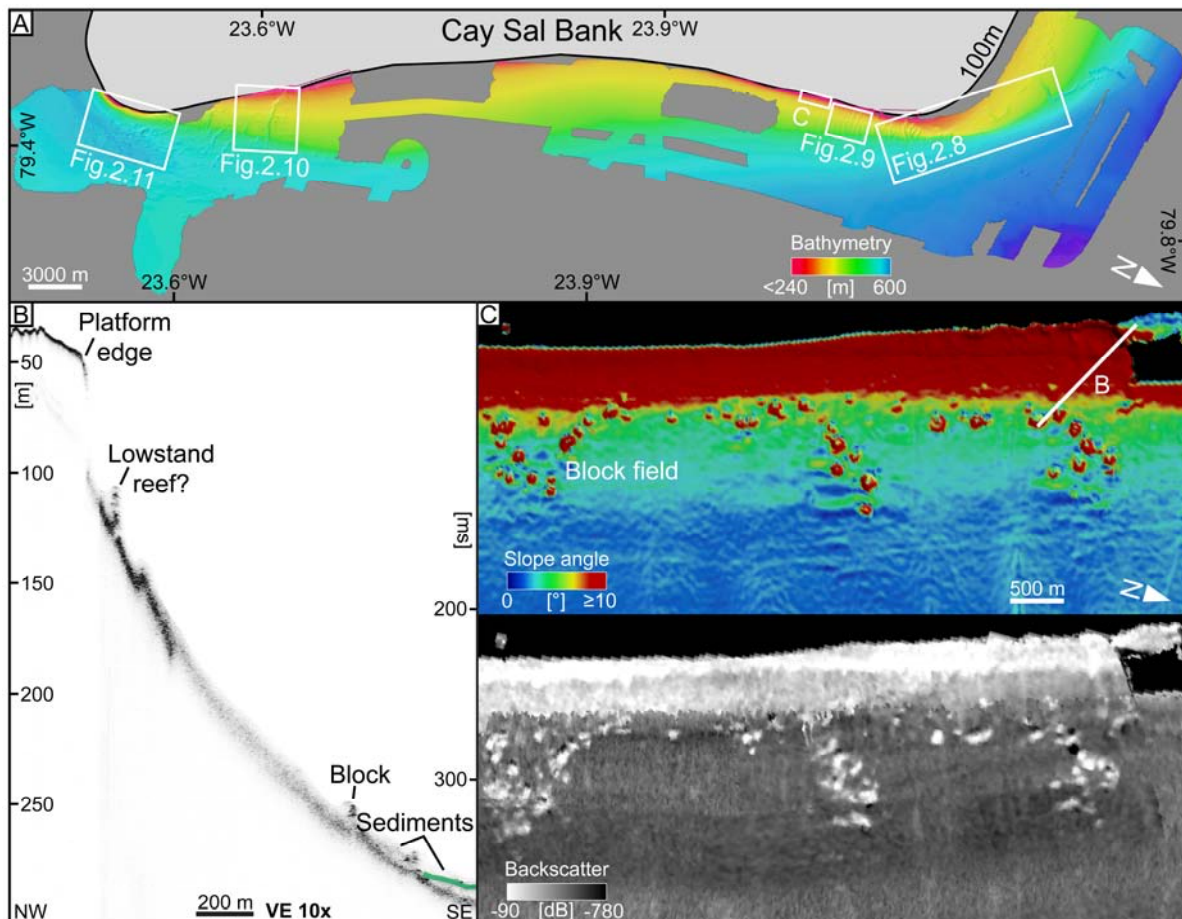


**Fig. 2.7:** **A:** Multibeam bathymetry of the windward slope of Cay Sal Bank. White rectangles indicate the positions of C and Figs 2.8 to 2.11. **B:** The slope-parallel subsurface profile shows the platform edge at a water depth of 50 m. At a water depth of 120 m, the slope is fringed by mound-shaped structures interpreted as lowstand reefs, which are imaged as convex reflections of high amplitudes. Further downslope, the slope is lined by a strip of blocks. At a water depth of 270 m, the slope is overlapped by a sedimentary wedge. The green line indicates Sequence Boundary S. **C:** Slope-angle steepness map and backscatter image of the area at a water depth of 240 m. The blocks are up to 10 m high and their shape varies from circular to slightly elliptic.

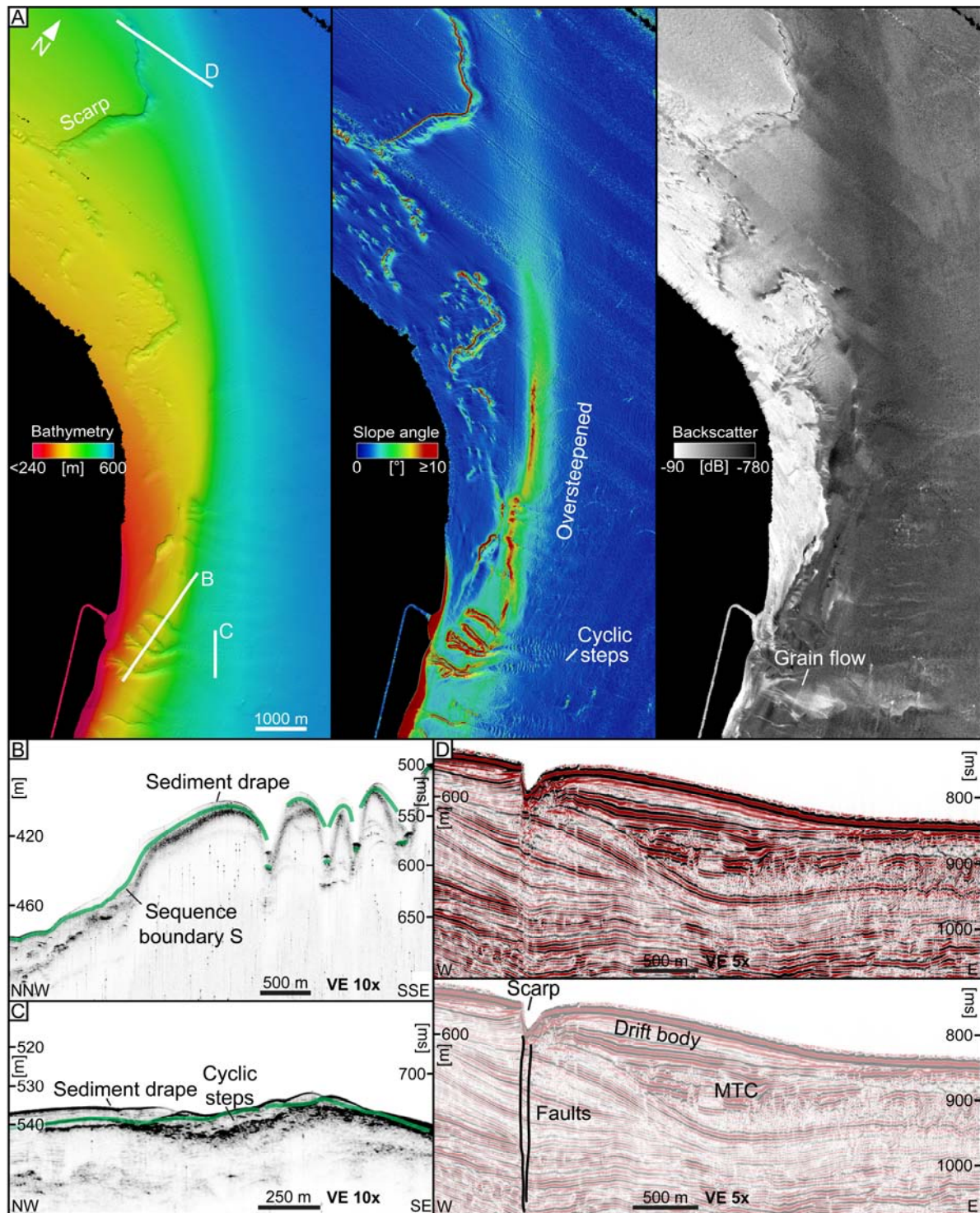


**Fig. 2.8:** North-western edge of the windward slope of Cay Sal Bank, where the slope is incised by four channels. Cyclic steps occupy the thalwegs and the areas beneath their distal termini. Towards the north, the slope is intersected by a scarp, which forms a 40 m high and 9 km long step. See Fig. 2.7A for location, the green line indicates Sequence Boundary S. **A:** Multibeam bathymetry, slope-angle steepness map and backscatter image. White lines indicate the positions of the cross-sections provided in B to D. **B:** Cross-section of the channels that runs perpendicular to the channel axes at a water depth of 420 m. **C:** Profile perpendicular to the channel axes showing the area where the channels terminate at a water depth 540 m. **D:** Cross-section shows the scarp separated from a drift body by a ca 100 m wide depression. Internally, this drift body is characterized by subparallel and continuous medium to high-amplitude reflections. The reflections underneath the scarp are dissected by fault planes. MTC = mass transport complex.

In the northern part of the eastern CSB slope, four deep channels intersect the slope (Fig. 2.8A). The channel widths range from 300 to 660 m, with a depth of up to 60 m. The single channels split up into a dendritic pattern at their upslope end. Multibeam data reveal upslope-facing sediment waves in the thalwegs and at the termini of the channels (Fig. 2.8A). The internal reflection pattern within the channel flanks in the upper part is transparent but consists of convex reflections of medium to low amplitude in the lower part. The channel fill is imaged as convex reflections of high amplitude (Fig. 2.8B; C).

Further north, at the entrance to the Florida Straits, the CSB slope is dissected by a 40 m high and 9 km long scarp (Fig. 2.8A; D). In plan view, the scarp has a zigzag shape. To the east of the scarp and separated by a ca 100 m wide depression is a convex-shaped 10 km long sediment body that internally contains parallel and continuous medium to high-amplitude reflections (Fig. 2.8D).

Towards the south of CSB, curved furrows intersect the slope (Fig. 2.9A). The furrows are dendritic in the proximal part (Fig. 2.9B) and located between 270 m and 500 m of water depth, where the slope angle decreases from 5 to 2°. Furrow widths range from 60 to 100 m with a relief of 2 to 10 m. The thalwegs and the areas beneath the terminations of the furrows are covered with upslope-facing sediment waves. The furrows are separated by asymmetrical ridges with their steeper sides dipping towards the north and their gentle flanks dipping south. In the subsurface data, the ridges are imaged as stacked sinuous reflections of medium to low amplitudes (Fig. 2.9C). Downslope, the relief of the ridges decreases and the internal reflections change to subparallel with medium amplitude (Fig. 2.9D).

In the southern part of the CSB slope, two channels exist at water depths between 300 m and 520 m (Fig. 2.10A). The larger channel cuts 30 m into the sea floor and is up to 700 m wide, whereas the smaller channel is 10 m deep and up to 300 m wide. The thalweg and the area at the channel terminations are covered by upslope-facing sediment waves (Fig. 2.10A; B). In subsurface data, the channel flanks are imaged as convex reflections of medium amplitude, which converge towards the channel axis (Fig. 10C; D). The interval between the channels is seismically characterized by the occurrence of cut and fill structures of various sizes. These cut and fill structures show parallel to subparallel reflections of medium to high amplitude, which are capped by subparallel reflections of low to medium amplitude (Fig. 2.10D). Below the cut and fill structures [below 600 msec TWT (two way travel time)], seismic reflections are dissected by nearly vertical planes. Along these planes the seismic reflections are attenuated and locally an offset of the reflections is visible (Fig. 2.10D). In

the slope-parallel seismic line (Fig. 2.10E) the reflection pattern consists of parallel and slightly basinward-dipping reflections of low to medium amplitude. In the area where the toe of slope is located, the reflections are dissected by three nearly vertical planes, which are characterized by the attenuation of the seismic reflections. Between these planes the reflection pattern is discontinuous and partly concave reflections of medium amplitude occur (Fig. 2.10E).

The southernmost part of the CSB slope is steep (Fig. 2.3) and a field of mounds and blocks litters the toe of slope (Fig. 2.11A). These blocks and mounds are circular in shape and up to 40 m high, and have elongated scours on one side that point to the south or south-west. The northern flanks of the mounds are generally smooth and overlapped by sedimentary wedges of various thickness (Fig. 2.11B). These mound-shaped structures appear acoustically hard, lacking internal reflections (Fig. 2.11B). The internal reflection pattern of the sedimentary wedges consists of parallel to subparallel reflections of medium to high amplitude (Fig. 2.11B).

### **2.4.3 Surface sediments**

The distribution of surface sediments along both slopes is shown in Fig. 2.12. Tab. 2.1 shows the sample locations, water depths and main compositional characteristics. Along GBB the loose first sediments on the slope are found in the overlapping sediment wedge with the plunge pool on its upper end while the portion of the slope above the wedge is cemented (Schnyder et al., 2014). The plunge pool and the adjacent ridge consist of coarse-grained sediments with a grainstone texture. These sediments are mainly composed of medium to coarse peloidal sand. The major components are peloids, foraminifera and, in one sample, *Halimeda*. More basinward, down to a water depth of ca 560 m, the slope is covered by fine-grained sediments with a packstone texture. These deposits are mainly composed of very fine to fine peloidal sand and carbonate mud. Distally, the sediment coarsens again and the slope between 560 m and 600 m is covered by medium to coarse foraminiferal sand with a grainstone texture.

The surface of the mounds/blocks at the toe of slope is partly covered by dead scleractinia and sponge fragments. The dominating coral species are *Lophelia pertusa*, *Madrepora oculata* and *M. minutiseptum*. The finest sediments within the study area are located in the Santaren drift, at water depths of ca 600 m. These sediments have a wackestone texture and are mainly composed of carbonate mud. The main coarse components are pteropod shells and fragments. On the windward slope of the CSB, changes in grain size and sediment composition occur along the strike of the slope. The northern part of the slope is covered by

sediments with a packstone texture, which are mainly composed of very fine to fine bioclastic sand and mud with admixtures of pteropod shells and fragments as well as planktonic foraminifera. Towards the south, the sediments coarsen due to an increasing percentage of coarse bioclastic sand and gravel. These sediments show a floatstone texture.

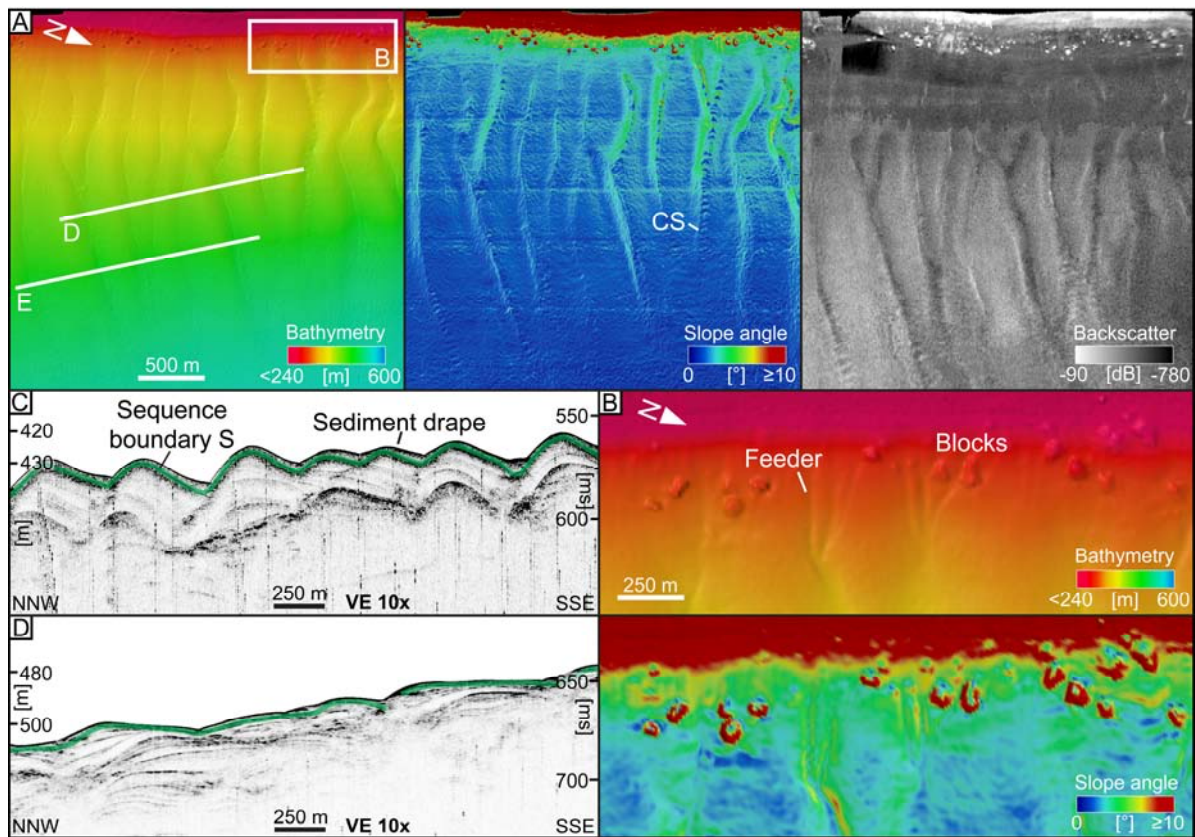


**Fig. 2.9:** System of furrows and asymmetrical ridges in the northern part of the Cay Sal Bank. Cyclic steps (CS) occupy the thalwegs and the areas beneath their distal termini. See Fig. 2.7A for location, the green line indicates Sequence Boundary S. **A:** Multibeam bathymetry, slope-angle steepness map and backscatter image of the area. White lines indicate the positions of the cross-sections provided in C and D. The white rectangle indicates the position of B. **B:** Close view of the proximal ends of the furrows at a water depth of ca 270 m. The proximal ends of the furrows consist of small shallow feeders, which start within the block field and converging downslope into the furrows. **C to D:** Cross-sections of the furrows that run perpendicular to the furrow axes at water depths of 430 m and 500 m.

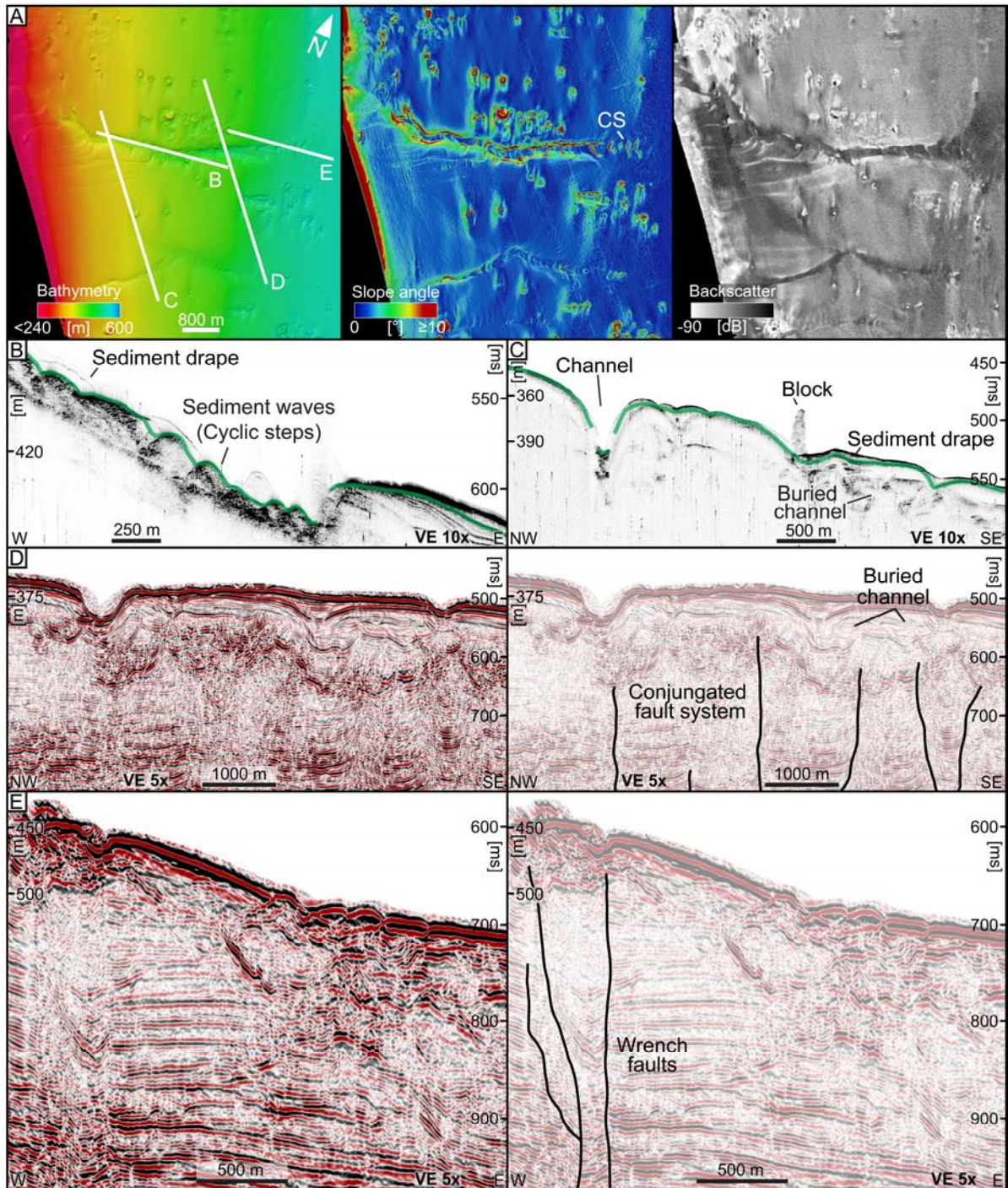


**Fig. 2.10:** Southern part of the Cay Sal Bank windward slope with two channels intersecting the drift sediments. The thalwegs and the areas beneath the termini of the furrows are covered with cyclic steps (CS). See Fig. 2.7A for location, the green line indicates Sequence Boundary S. **A:** Multibeam bathymetry, slope-angle steepness map and backscatter image of the area. White lines indicate the positions of the cross-sections provided in B to E. **B:** Cross-section of a channel thalweg that runs in parallel to the channel axis. The thalweg is occupied by cyclic steps. **C:** Cross-section of the channels at a water depth of 360 m. Cut and fill structures within the channel flanks are interpreted as buried channels. **D:** Strike-parallel profile located at a water depth of 550 m. The upper part of the profile is characterized by large concave cut and fill structures, which are interpreted as buried channels. In the lower part, the reflections are dissected by vertical fault planes. **E:** The slope-parallel seismic line shows three nearly vertical planes, which dissected the reflections in the area of the toe of the slope.

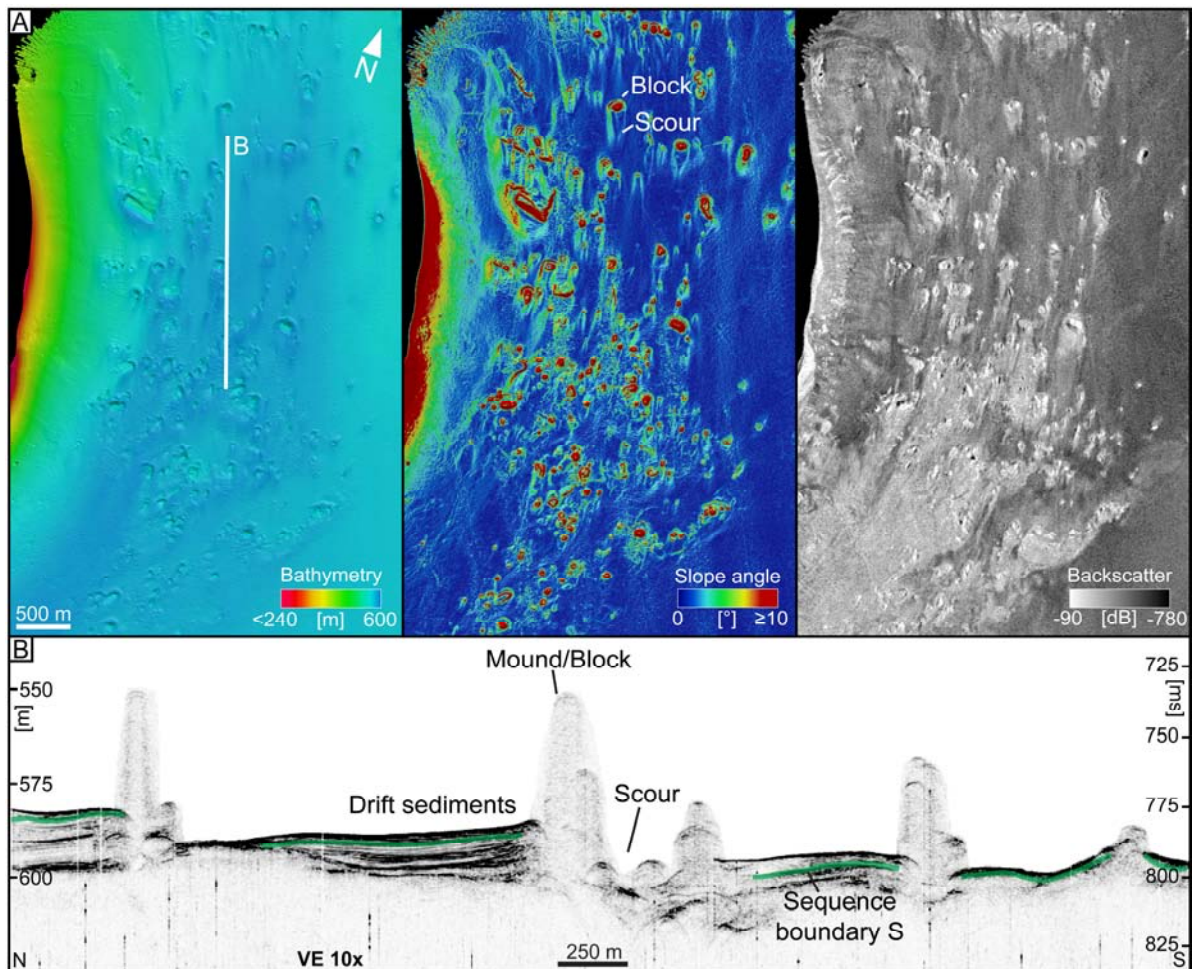


**Fig. 2.11:** The south-western edge of the windward slope of Cay Sal Bank. See Fig. 2.7A for location, the green line indicates Sequence Boundary S. **A:** The slope is characterized by steep slope angles and the toe of slope is occupied by a field of mounds and blocks. These structures are circular in shape, and up to 40 m high. Their downcurrent terminations are formed by elongated scours that point to the south or south-west. White line indicates the positions of the cross-section provided in B. **B:** The northern mound flanks are generally smooth and overlapped by sedimentary wedges of various thicknesses. These mounds appear acoustically hard without internal reflections.

## 2.5 Interpretation and discussion

### 2.5.1 Contour current indicators

In the Santaren Channel, scours at the sea floor are pervasively linked to block and mound-shaped bodies. Scours behind obstacles are generated by erosive bottom currents (Werner et al., 1980). Figure 2.13 shows the direction of the contour currents as indicated by orientation and shape of the scours, with the scour length taken as a relative indicator for bottom-current speed. Flume experiments show that the length of such scours also depends on the size of the obstacle, but their presence can be taken as an indicator for strong bottom currents (Werner et al., 1980; Stow et al., 2009). At the northern edge of the CSB, east-directed contour currents bend into the Santaren Channel and flow southward along the

slope of CSB. At the southern edge of CSB, the flow direction changes towards the southwest. Scours along the CSB slope are up to 700 m long (Fig. 2.11A). The eastern side of the Santaren Channel is dominated by northward flowing contour currents, which form up to 1200 m long northward-oriented scours (Fig. 2.5A). Tidal reversals of the bottom currents were measured 40 m above the sea floor along the eastern side of the Straits of Florida but because of the interference of the north-directed contour current the north direction is dominant (Correa et al., 2012; Lüdmann et al., 2016).

## **2.5.2 Depositional model**

### **2.5.2.1 Great Bahama Bank: Sea-level lowstand**

The depositional processes during the last sea-level fall and the associated glacial lowstand are dominated by reworking and non-deposition at the leeward slope of GBB, that leads to the formation of omission surfaces, hardgrounds and firmgrounds at or near the sea floor and the formation of SB S (Fig. 2.14; Tab. 2.2) (Schlager et al., 1994; Malone et al., 2001; Eberli et al., 2002). The data herein presented indicate that along the northern part of the slope extensive slope failure occurred during the lowering of the sea level. These slope failures displaced debris and small blocks as mass transport complexes (MTC) to the toe of slope (Figs 2.6 and 2.14). Correlation between the position of the detachment surface of the slope failures and the  $\delta^{18}\text{O}$ -stratigraphy at ODP site 1003 confirm that the sediments above the detachment surfaces were deposited during MIS 1, whereas the sediments beneath originated from MIS 8 (Rendle et al., 2000; Rendle and Reijmer, 2002). Age assignment of the slope failures to the last lowstand is further supported by U/Th dates from depths of 8.22 mbsf and 14.4 mbsf (metres below sea floor), which yielded ages of 5 ka BP and 383 ka BP, respectively (Henderson et al., 2000). Sequence boundary S, which formed during MIS 4 to 2, separates these sediment packages from one another. This places the slope failures into the time interval between the onset of the last glaciation and the onset of MIS 1. In addition, the age of the slope failures is constrained to this time interval by the age of MTC material (MIS 8 to 5). The head walls of the MTC are formed by up to 25 m high scarps at the sea floor (Fig. 2.6A). Upslope extensions of the slope failures formed the initial base of the gullies (Fig. 2.6A- C); they appear at a water depth of 370 m and terminate at 450 m, where the scarps are located. Debris and small blocks of the MTC are colonized by deep-sea corals (Betzler et al., 2014; Lüdmann et al., 2016), comparable to similar situations elsewhere in the Florida Straits (Correa et al., 2012; Hebbeln and Wienberg, 2012). The deep-sea corals form up to 25 m high mounds, which are elongated parallel to the current direction (Fig. 2.5A; B) (Lüdmann et al., 2016).

Large-scale MTC are known from other sites of the Bahamian archipelago (e.g. Harwood and Towers, 1988; Mulder et al., 2012; Jo et al., 2015; Principaud et al., 2015), where they have been related to the release of pore-water pressure triggered by seismic shocks. Here, it is proposed that the slope failures occurred along distinct detachment layers caused by changes in sediment shear strength. Cores drilled during ODP Leg 166, show that the highstand sediments consist of mudstone, wackestone, packstone and grainstone with interbedded floatstone (Eberli et al., 1997). These highstand deposits are bounded by well-lithified intervals which are formed at or near the sea floor during sea-level lowstands (Malone et al., 2001; Eberli et al., 2002). These alternations of heavily and less cemented intervals introduce abrupt shifts in shear strength within the sedimentary column. Most important is the low shear strength of the highstand sediments just above the lithified horizons, because it represents a potential weak detachment layer along which slope failure can occur (Jo et al., 2015; Principaud et al., 2016). In addition, the sedimentary succession is characterized by an intercalation of turbidites and periplatform ooze (Bernet et al., 2000; Eberli, 2000). The coarse bottom layer of the turbidites contains more interstitial water, which is prone to higher water content and may also act as a detachment layer (Eberli, 1988; Jo et al., 2015).

The slope failures are likely to be triggered after a sea-level highstand during the subsequent sea-level lowering. This corroborates the recent findings of Principaud et al. (2016) from the northern part of the leeward slope of GBB, where those authors suggest that slope instabilities occurred during the early stages of a major sea-level fall after times of highest rates of slope sedimentation.

#### **2.5.2.2 Great Bahama Bank: Sea-level rise and highstand**

Sedimentation after formation of SB S initiated between 11.3 kyr and 10 kyr BP (Slowey et al., 2002) and forms a sedimentary wedge, which is interpreted as periplatform drift (Betzler et al., 2014). This periplatform drift is internally subdivided into two parts (Fig. 2.2C, inset). The proximal is a package with a transparent to faintly parallel-bedded succession, which distally thins out below the package of the sediment waves that forms the distal part (Fig. 2.2C). This subdivision is also reflected in the sedimentary succession at ODP site 1009, which shows a decrease in aragonite content and a coarsening-upward above 9.30 mbsf (Eberli et al., 1997), i.e. at the depth position of the limit between both packages. Radiocarbon dating yielded an age of ca 5.3 kyr cal BP for sediments at 12 mbsf (Slowey et al., 2002). A similar sedimentary turnover described by Roth and Reijmer (2004) from the north-western edge of GBB was dated ca 4.6 ka BP.

This packaging within the periplatform drift is interpreted to reflect the successive flooding stages of GBB. Post-LGM bank flooding started at 7.2 ka BP, and around 6 ka BP, 70% of the platform was flooded (Roth and Reijmer, 2004; Purkis et al., 2014). During this phase of sea-level rise, the carbonate production resumed in the flooded parts of the platform top and the platform started to export to the leeward slope. The exported sediments accumulated at the base of the steep cliff and formed the lower package of the wedge at a water depth of 160 m (Fig. 2.2C). In the northern part of the GBB slope, the platform export was funneled by upslope extensions of the slope failures forming the gullies. These funneled sediments subsequently filled the depressions beneath the scarps (Fig. 2.6E). This filling process is further documented by the thickness map, which displays increased thickness of the Holocene sequence beneath the scarps (Fig. 2.6A). During the late stages of the post-glacial sea-level rise (5.0 to 4.6 ka BP; Roth and Reijmer, 2004), the carbonate production on the platform top peaked and the density cascading strengthened, which is reflected by the onset of the sediment wave formation and the shallow furrows in the southern part of the leeward slope (Fig. 2.4A). Betzler et al. (2014) interpreted these sediment waves as cyclic steps and related their genesis to the platform export of the GBB. This off-bank transport is in general oriented normal to the isobaths, but on the GBB flank, the crests on average have a clockwise angle of up to 15° with respect to depth contours of the slope (Betzler et al., 2014). Similar to examples described by Kostic (2011), the GBB cyclic steps form downslope of a break in slope angle, which probably triggers a hydraulic jump in supercritical flows. These cyclic steps differ from antidunes by their asymmetry (Fig. 2.2C, inset); antidunes show equal slopes on both sides, whereas cyclic steps have a steeper lee side and more gentle stoss side (Cartigny et al., 2011). In this part of the slope, the entire upper sediment package of the Holocene wedge consists of cyclic steps (Fig. 2.2C). The orientation of sediment waves reflects the direction of the off-bank directed bottom-current flow.

The shallow furrows (Fig. 2.4A) which crosscut the cyclic steps, are related to density cascading events. It is proposed that density cascades are partly funneled by the V-shaped notches in the ridge on the downward side of the plunge pool (Fig. 2.2D; E). The funneled part of the flow erodes the notches on the basinward flank of the ridge (Fig. 2.2D). The incised furrows are relatively shallow and their base never intersects the subjacent sequence boundary; locally levee-like structures are observable (Fig. 2.4D). The absence of obvious lobes and cyclic steps within the furrow axis indicates that these furrows are short-term and caused by single events.

The influence of the contour currents is reflected in the spatial distribution of the sediments (Fig. 2.12; Tab. 2.1). The coarsest sediments are found near the platform margin, in the area of the plunge pool. More basinward, down to a water depth of ca 560 m, there is a fining in grain size. Here, the slope is covered by very fine to fine peloidal sand with a high mud content. This fining reflects the gravitational controlled grain-size distribution along carbonate platform slopes, which assumes a decrease in grain size with increasing distance from the platform (Playton et al., 2010). More distally, however, the surface sediments show a reverse pattern and the slope between 560 to 600 m is covered by medium to coarse foraminiferal sand with a reduced percentage of mud. This coarsening is related to the contour currents, which winnow fine-grained material: Current measurements determined a current velocity of  $120 \text{ cm sec}^{-1}$  at the toe of slope of the GBB (Lüdmann et al., 2016).

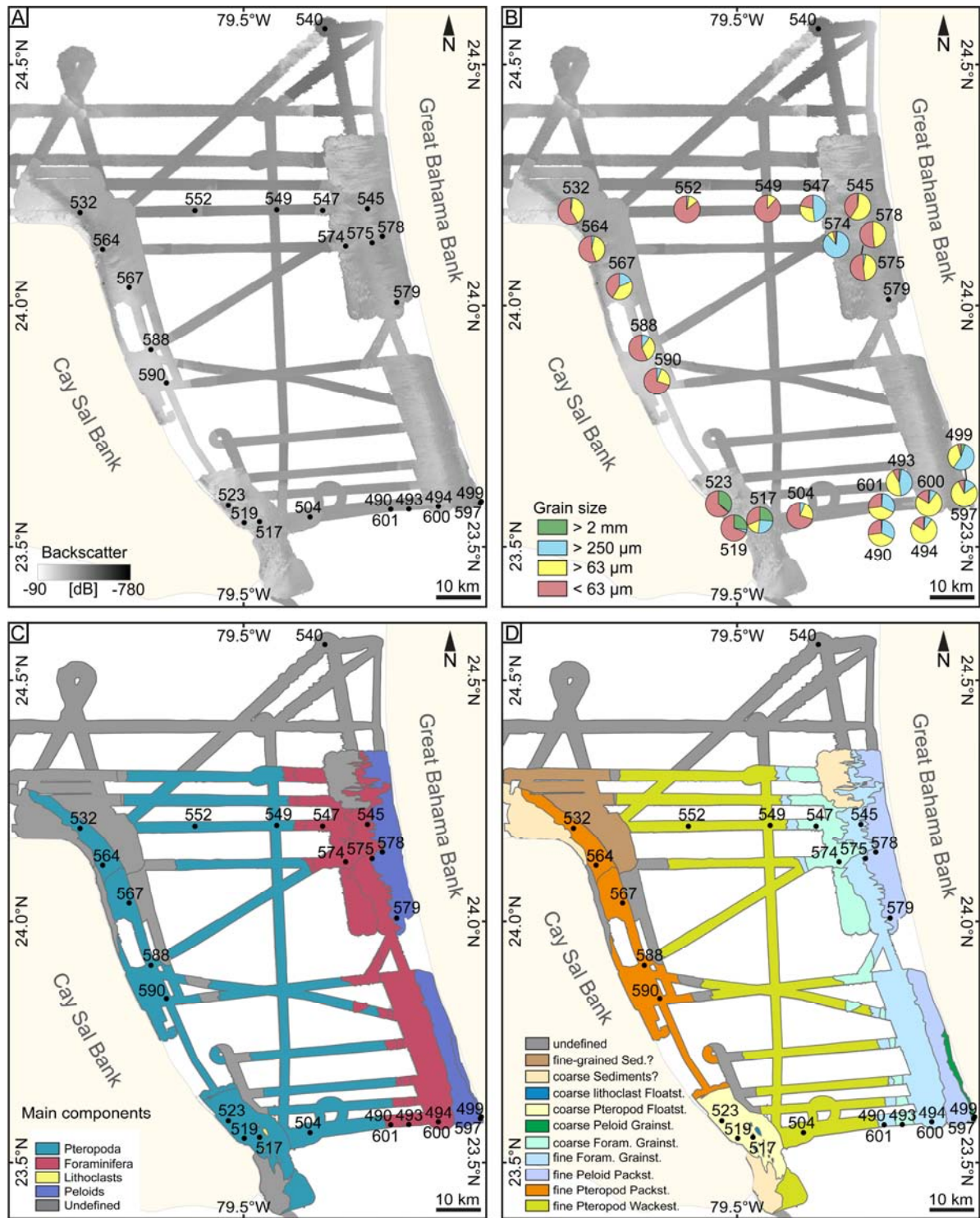


**Fig. 2.12:** Characteristics of the sediment surface samples collected during the research cruise M95. **A:** Backscatter data and positions of the sample sites. **B:** Positions of the surface samples with individual grain-size characteristics. **C:** Spatial distribution of main components. **D:** Surface sediments classified after Dunham (1962).

Sample	Latitude	Longitude	Depth (m)	Main component	Secondary component (frequency)	Grain-size distribution (%)				CaCO <sub>3</sub> content (%)	
						>2 mm	>250 µm	>63 µm	<63 µm	Bulk	<63 µm
490	23°35,984' N	79°12,924' W	541	Foraminifera	LC, Pelo, Pt	1.1	31.0	40.9	27.0	84.5	84.5
493	23°36,071' N	79°10,771' W	546	Foraminifera	LC, Pelo, Snails, Bivalves	2.6	45.2	44.1	8.1	84.3	89.0
494	23°36,414' N	79°07,210' W	501	Foraminifera	LC, Pelo, Pt	1.2	9.1	73.5	16.2	89.5	90.1
499	23°36,803' N	79°02,230' W	160	Peloids	Hali, Foram, SF	5.1	54.7	35.9	4.3	91.5	84.4
504	23°35,172' N	79°22,830' W	534	Pteropoda	Pelo, Foram, SF	0.3	6.4	22.9	70.4	81.5	84.8
517	23°34,303' N	79°28,756' W	510	Lithoclasts	Foram, Pelo, SF	26.2	25.7	16.9	31.2	87.3	85.7
519	23°34,225' N	79°30,706' W	413	Pteropoda	Foram, Pelo, SF	27.2	3.4	0.4	68.9	89.6	84.5
523	23°36,345' N	79°32,614' W	386	Pteropoda	SS, Pelo, SF	35.2	1.4	0.1	63.3	84.6	86.1
532	24°11,659' N	79°50,511' W	567	Pteropoda	Foram, SS, Pelo	0.1	1.8	39.7	58.4	85.7	86.3
540	24°33,689' N	79°20,720' W	601	Corals	SS, Pt, Bivalves	-	-	-	-	-	-
545	24°12,138' N	79°15,823' W	560	Foraminifera	Pt, Pelo, SF	0.0	1.3	58.0	40.7	88.5	86.2
547	24°12,027' N	79°21,239' W	617	Foraminifera	Pt, Pelo, LC	0.5	47.9	29.9	21.7	83.7	81.1
549	24°11,957' N	79°26,765' W	586	Pteropoda	Foram, Pelo, SS	0.0	0.9	11.5	87.6	80.1	83.1
552	24°11,829' N	79°36,524' W	635	Pteropoda	Foram, Pelo, LC	0.3	2.5	12.1	85.2	74.8	81.4
564	24°07,002' N	79°47,844' W	484	Pteropoda	Foram, SF, Pelo	0.3	3.2	41.4	55.0	83.0	86.5
567	24°02,564' N	79°44,633' W	534	Pteropoda	Foram, SF, Pelo	0.7	18.9	39.3	41.1	87.0	88.6
574	24°07,775' N	79°18,488' W	603	Foraminifera	Pt, Pelo, LC	1.2	87.3	7.4	4.1	82.8	77.2
575	24°08,036' N	79°15,309' W	559	Peloids	Pt, Foram, LC	0.1	2.8	45.0	52.2	89.4	88.4
578	24°08,712' N	79°14,024' W	509	Peloids	Pt, Foram, LC	0.0	0.9	47.4	51.7	89.7	90.4
579	24°00,839' N	79°12,290' W	418	Peloids	Pt, Foram, SF	-	-	-	-	-	-
588	23°54,971' N	79°41,959' W	474	Pteropoda	Foram, SF, Pelo	0.4	10.0	32.7	56.9	88.3	91.9
590	23°51,049' N	79°40,086' W	451	Pteropoda	Foram, Pelo, SF	0.3	5.6	24.3	69.9	79.5	86.0
597	23°36,761' N	79°02,093' W	151	Peloids	Foram, LC, Hali	1.4	14.1	77.1	7.4	90.9	85.3
600	23°36,211' N	79°07,229' W	501	Foraminifera	LC, Pt, Pelo	1.5	8.6	73.3	16.5	88.7	83.6
601	23°35,826' N	79°12,989' W	540	Foraminifera	Pt, LC, Pelo	1.0	31.2	40.7	27.1	84.7	81.3

**Table 2.1:** Composition of the surface samples collected during the research cruise M95 CICARB. Secondary components: LC = Lithoclasts; Pelo = Peloids; Pt = Pteropod shells and fragments; Foram = Foraminifera; Hali = *Halimeda*; SF = Skeletal fragments; SS = Sponge spicules.

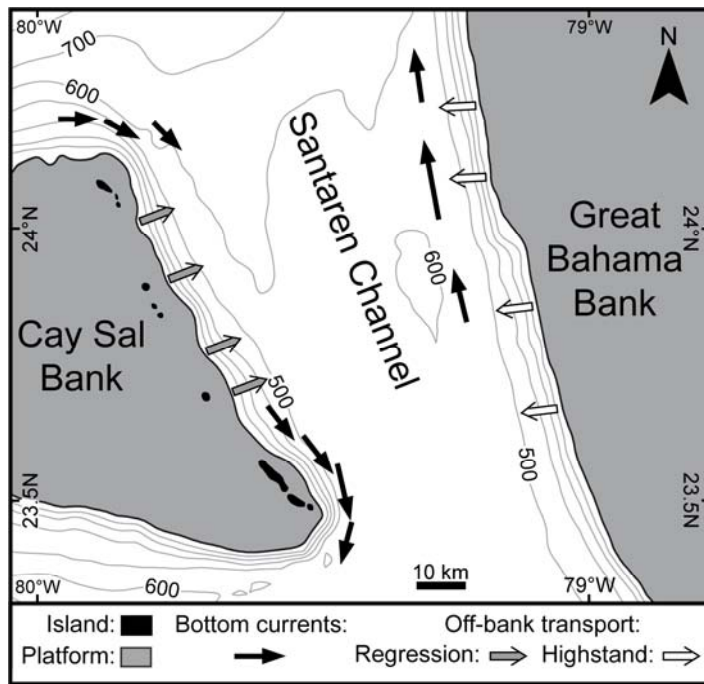


**Fig. 2.13:** Map of the prevailing contour currents direction derived from the orientation and size of the scour marks located downcurrent of blocks and mounds (black arrows). Grey and white arrows indicate the current direction of off-platform export as derived from cyclic steps and sediment waves.

### 2.5.2.3 Cay Sal Bank: Sea-level lowering and lowstand

Around 115 ka BP, at the onset of the last glaciation, the sea level fell 10 m below its present position (Siddall et al., 2003). As a consequence, the platform centre of CSB emerged, whereas the platform margins were still placed at a water depth of 40 m (Purkis et al., 2014). The emerged inner bank therefore was a barrier for the west-ward-flowing trade-wind-induced surface currents. It is proposed that this water mass movement was balanced through an offshore-directed downwelling that eroded and transported platform material basinward (Fig. 2.15A).

Downwelling current flow was unhindered because there is no reef along this margin (Hine and Steinmetz, 1984), and the exported sediments could bypass the upper 200 m of the slope and accumulate within and beneath the block strip (Figs 2.7B; 2.14; 2.15A), which is nowadays located at a water depth of 240 to 290 m, where the slope angle flattens. Similar sediment accumulations behind a strip of fallen blocks occur on many windward slopes throughout the Bahamian archipelago (Grammer and Ginsburg, 1992). This can be speculated if the surface currents were intensified during the glaciation, caused by the strengthening of the trade winds concurring with the shift of the Intertropical Convergence Zone (Broccoli, 2000; Peterson et al., 2000; Schmidt and Spero, 2011).

Furrow initiation along CSB is probably also induced by the downwelling, which episodically induced grain flows and turbidity currents. To entrain fine-grained carbonate sands very low shear velocities in the range of 1.0 to 1.8 cm sec<sup>-1</sup> are needed (Prager et al.,

1996; Black et al., 2003). Based on the equations provided by Southard et al. (1971) a current velocity of 10 to 20 cm sec<sup>-1</sup> is required to resuspend sediments similar to the deposits at the CSB slope. Once established, furrows channelize and bypass sediments to the lower slope. This sediment transport is reflected by the cyclic steps in the thalwegs and the terminal lobes (Fig. 2.9A). Several feeder areas in the proximal part of the furrows supply sediment to the furrows during following events. These feeders are located at a water depth of ca 250 m, within the strip of blocks (Figs 2.7B; 2.9B). The channelized flows interact with the southward-flowing contour currents (Fig. 2.13) which deflect parts of the channelized flow to the south (Fig. 2.11B). As a result, sediment is accumulating at the southern flanks of the furrows. As sediment thickness increases, the deflected flow forms a distinct steep north-facing bench (Figs 2.9C; 2.15B). The development of this specific furrow and ridge system is restricted to the northern part of the windward slope, lower slope angles towards the south prevent erosion by turbidity currents (Parker et al., 1986; Blanchette et al., 2006).

During sea-level lowering and sea-level lowstand, the south-directed contour currents also accumulated drift sediments along the CSB slope. In parts, on the lower slope, the same contour currents undercut these drift sediments. This is expressed by the oversteepening of the toe of slope with angles higher than 10° that leads to slope adjustments and the formation of the channels in the northern slope segment (Figs 2.3; 2.8A-C). Slope adjustments are located at slope segments, where the slope angle exceeded the angle of repose. This angle of repose is ca 10° for mud-rich sediments with high water content (Kenter, 1990; Laberg and Camerlenghi, 2008), like the encountered drift deposits.

The velocity of the contour current varies (Fig. 2.13) and decreases towards the south, where the concave shape of the bank forms a current-protected area, in which drift sediments accumulate (Fig. 2.7A). These drift deposits shape a gently inclined slope (2°) with a smooth surface (Fig. 2.3), draped by fine-grained sediments (Fig. 2.12; Tab. 2.1). Towards the southern edge of the windward slope, the current velocity increases again (Fig. 2.13). Here, the contour currents erode elongated scours at the downcurrent side of the blocks (Figs 2.11; 2.13).

The time window for the falling stage deposition along the slope had a duration of 42 ka, i.e. from 115 to 73 ka BP and ended when sea-level was lowered 50 m with regard to present day sea-level (Siddall et al., 2003), and the entire platform top of CSB was emerged. The furrows and channels at this stage were deprived of sediment input, cyclic step formation ceased and development of an up to 10 m thick veneer of sediment draping the bedforms

(Figs 2.8B; 2.9C; 2.10B) initiated. Thus, the main accumulation of sediments on the windward slope occurs during sea-level falls. Although available data do not allow an age assignment of the mound-shaped bodies at a water depth of 125 m (Fig. 2.7B), it is proposed that they are lowstand reefs growing during the LGM, when sea-level was 125 m lower than today (Fairbanks, 1989).

Sea-level position	Great Bahama Bank	Cay Sal Bank
Sea-level fall	No platform export. Several slope failures occur along weak detachment layers at a middle slope position. The debris is deposited as MTC at the toe of slope.	Downwelling currents erode material from the platform top and transport it towards the slope. Slope channels are active and furrows as well as asymmetric ridges were formed.
Lowstand	No platform export, winnowing by contour currents and formation of hardgrounds.	No platform export, channels are inactive. Along the upper slope growth of lowstand reefs. The sedimentation on the slope is dominated by contour currents.
Sea-level rise	Initial flooding of the platform, start of platform export and accumulation of an initial slope wedge.	Drowning of lowstand reefs. Bank top flooding 1 kyr earlier than at GBB. Start of platform export towards the western leeward slope. Small slope failures along the submarine cliff.
Highstand	Intensification of the platform export and development of the plunge pool and the cyclic steps.	Platform export towards the leeward slope. Along the windward slope, the contour currents dominate the sedimentation.

**Table 2.2:** Summary of all events on both slope organized by timing and sea-level stage.

#### **2.5.2.4 Cay Sal Bank: Sea-level rise and highstand**

Cay Sal Bank was flooded 1000 years earlier than Great Bahama Bank, at a time where the rate of sea-level rise was higher (Purkis et al., 2014). During this phase, the lowstand reefs that fringed the slope (Fig. 2.7B) were drowned and at the toe of the submarine cliff a relatively small slope failure occurred. This slope failure induced grain flows, which are well-imaged in the backscatter data (Fig. 2.8A). The timing of the slope failures coincides with observations from the Tongue of the Ocean, where similar slope failures occurred ca 10 ka BP (Grammer et al., 1993); indicating that failures in the submarine cliff are typical during the sea-level rise.

Around 6 ka BP, the entire platform was flooded (Purkis et al., 2014) and the production of shallow-water carbonates on the platform resumed. With the continued rise in sea-level, the westward-flowing surface currents swept across the platform and the bulk of the sediments were transported to the leeward slope of the platform (Hine and Steinmetz, 1984; Purkis et al., 2014). By contrast, on the windward slope, the Holocene sediments form only

a thin drape (Figs 2.8B; 2.10B; 2.14; 2.15C). This Holocene drape consists of fine-grained sediments, with a high mud content and pteropod shells and fragments as the main coarse component (Fig. 2.12; Tab. 2.1), similar in composition and texture to the sediments in the Santaren drift. Hence, these sediments are probably in great part derived from the southward-directed contour currents, indicating that the present-day sedimentation on the windward slope of CSB is mainly controlled by contour currents. The slight increase in grain size towards the south of the windward slope correlates with the increased velocity of the southward-flowing contour currents (Fig. 2.13), which accelerate in this area before bending into the Nicholas Channel (Lüdmann et al., 2016).

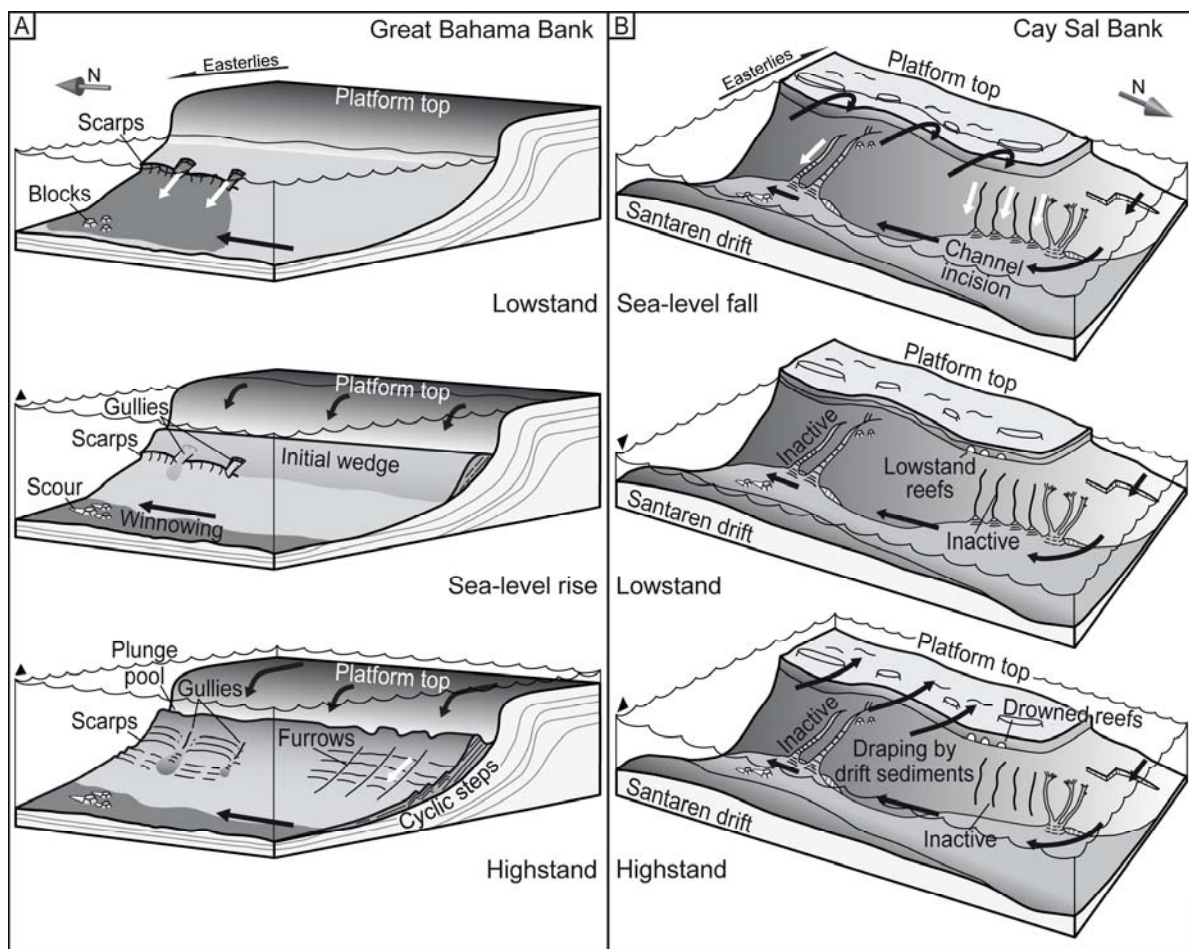


**Fig. 2.14:** Depositional model of the two Bahamian slopes, see discussion and Table 2.2 for details. Highstand stage of Great Bahama Bank (GBB), modified after Betzler et al. (2014).

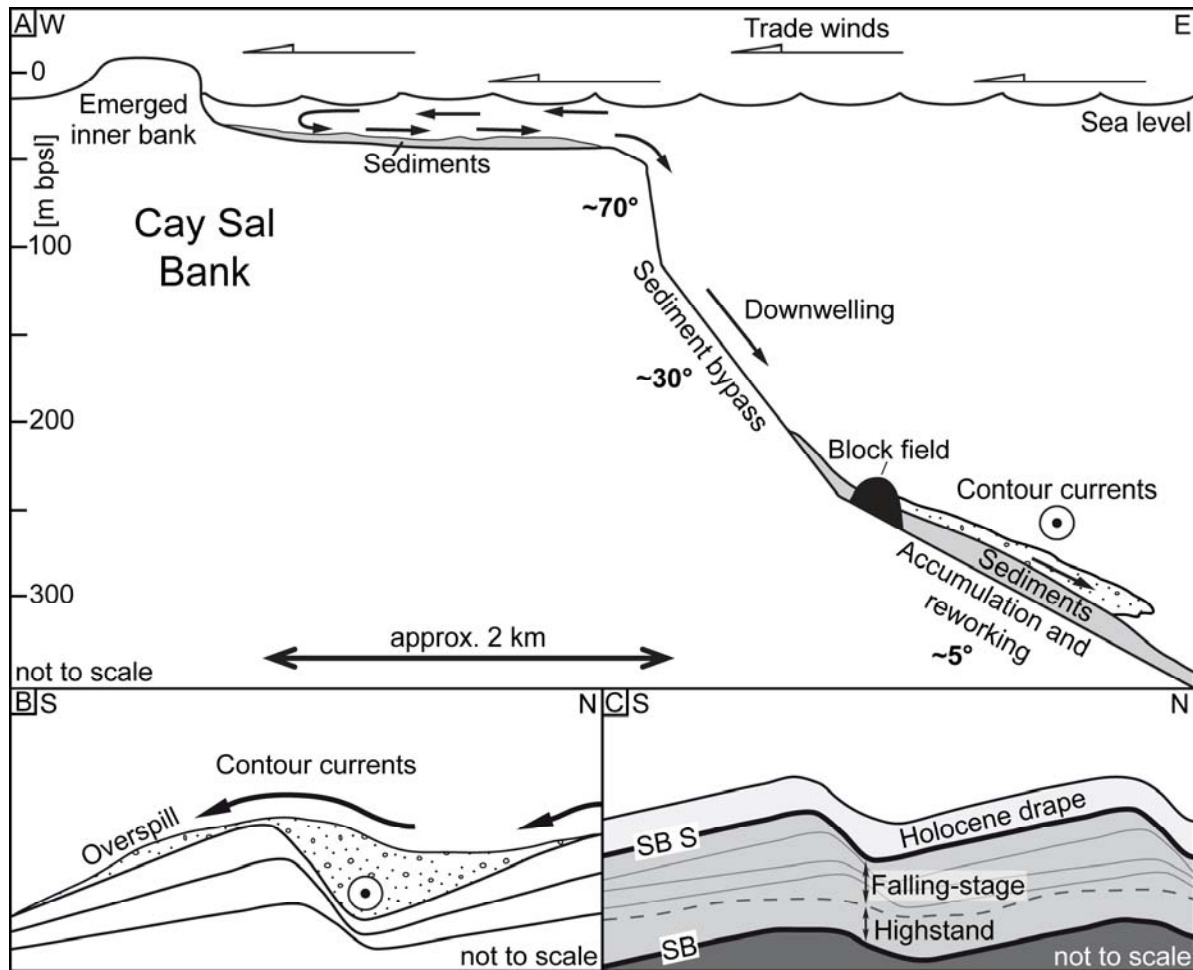


**Fig. 2.15:** Depositional model of the furrow and ridge system in the northern part of Cay Sal Bank. **A:** During the sea-level lowering, the western-directed surface currents induced a downwelling, which transported platform material to the windward slope. At a water depth of ca 270 m, this downwelling induced grain flows, which scoured slightly curved furrows into the slope. **B:** Once established, the furrows funnelled the platform material during the next events. The channelized flows interact with the southward-flowing contour currents, which deflected parts of the channelized flow to the south. As a result, sediment is accumulating at the southern flanks of the furrows. As sediment thickness increases, the deflected flow forms a distinct steep northern-facing bench. **C:** Stratigraphic scheme of sedimentary succession on the windward slope of Cay Sal Bank. The highstand sediments are superimposed by the sediments of the falling stage. During the following lowstand, Sequence Boundary S was formed. The succession is covered by a sediment drape, mostly Holocene in age.

### 2.5.2.5 Tectonic control

Slope depositional processes at CSB and GBB can clearly be linked to different sea-level stands, i.e. flooding stages of the banks, and to the contour current regime shaping and carving the slopes. In addition, the eastern CSB slope shows a tectonic control by the north-west/south-east trending Santaren Anticline (Masferro, 1997). This tectonic control is reflected in the concave shape of the flank of the bank (Masferro, 1997; Masferro and Eberli, 1999). Tectonic movements in the deeper subsurface induced a system of deep-rooted faults (Masferro and Eberli, 1999; Kula, 2014). The faults show thrust fault

characteristics in the north and wrench fault characteristics in the south of the study area. The indication for neotectonic activity along this fault system is a 40 m high scarp at the sea floor, which has a subsurface continuation to an underlying fault system (Fig. 2.8A; D) related to the north-east/south-west striking Cay Sal Anticline (Kula, 2014; Lüdmann et al., 2016). The scarp itself is interpreted as the headwall of a mass transport complex, which was deposited at the toe of the CSB slope (Fig. 2.8D). In the flow shade of this scarp, drift sediments formed a well-stratified sedimentary wedge (Fig. 2.8D). The surface of this drift body is covered by fine-grained sediments that are similar in composition and texture to the surface samples of the Santaren drift (Fig. 2.12; Tab. 2.1).

In the southern part of the area studied, faults also seem to control the occurrence and form of submarine channels in drift sediments (Fig. 2.10A). These channels are up to 700 m wide and up to 30 m deep, and in the subsurface several cut and fill structures within different stratigraphic levels are interpreted as buried channels (Fig. 2.10C; D). The occurrence of these buried channels is restricted to a small area (6000 m along slope) and their incision is related to a conjugated slope-parallel fault system (Fig. 2.10E). This fault system is induced by active deep-rooted wrench faults that trend north-east/south-west along the toe of slope of CSB (Fig. 2.1B). The tectonic activity related to this active fault system provides the heterogeneity to confine the channel incision within this relatively small slope area.

## *Chapter III*

# **Sedimentary dynamics and high-frequency sequence stratigraphy of the southwestern slope of Great Bahama Bank**

### **3.1 Outline of the chapter**

In chapter III, a combination of high-resolution subsurface and multichannel seismic data were linked with the existing seismic stratigraphy and sedimentological core data of ODP Leg 166 to reconstruct the depositional evolution of the leeward slope of Great Bahama Bank since the Late Miocene. The chapter shows that the interplay of erosional and depositional processes, encountered in the youngest sequence (chapter II) also acted during older sequences. The results of this chapter show how contour currents shaped the slope geometry. The current influence on the leeward slope increases from south to north. Along slope segments with high current control, drift migration and current winnowing at the toe of slope triggered large slope failures, which finally inhibited the slope progradation. Along slope segments with weaker current control, large slope failures are rather controlled by the position of the sea level.

### **3.2 Geologic and oceanographic setting of the study area**

The study area is located along the western slope of Great Bahama Bank (GBB) and covers the segment of the slope that is facing the Santaren Channel (SC). The SC is a 65 km wide and 750 m deep marine strait between GBB and Cay Sal Bank connecting the Straits of Florida with the Old Bahama Channel (Fig. 3.1A).

The isolated platforms of the Bahamian archipelago lie on horsts, which formed during the opening of the Atlantic (Mullins and Lynts, 1977; Eberli and Ginsburg, 1987, Eberli, 1991). Although the initial relief was partly leveled during early platform coalescence, tectonic segmentation during the collision of the North American plate with the Cuban arc reactivated older faults, drowned part of the platforms and created seaways (Eberli and Ginsburg, 1987; Ladd and Sheridan, 1987; Masferro and Eberli, 1999). During the Neogene, a renewed coalescence of several smaller platforms by seaway filling and bank progradation formed the modern GBB (Eberli and Ginsburg, 1987). Since the late Middle Miocene, the platform margin facing the SC prograded 25 km to the west (Eberli and Ginsburg, 1987). During the Pliocene, a change in the depositional profile from a ramp towards a flat-topped platform with a steep margin occurred (Betzler et al., 1999). Ball et al.

(1987) proposed that the Florida Current (FC) inhibited further westward progradation of the platform margin that faces the Straits of Florida. However, an up to 90 m thick wedge of Holocene sediments indicates ongoing sediment accumulation at the slope facing the SC (Wilber et al., 1990; Eberli et al., 1997, Roth and Reijmer, 2004, 2005; Betzler et al., 2014; Wunsch et al., 2016). This Holocene sediment wedge at the leeward flank of GBB is modified by contour currents and has thus been designated as periplatform drift by Betzler et al. (2014).

The current system around the Bahamian archipelago is dominated by the North Atlantic gyre to the east of the Bahamas and by the FC to the west (Bergman et al., 2010). The FC is composed of water masses from the Gulf of Mexico and the Caribbean Sea (Schmitz and Richardson, 1991). It passes the Straits of Florida and becomes a major part of the Gulf Stream, the surface-flowing limb of the North Atlantic gyre. The FC does not fill the entire strait and coastal countercurrents flow along the Florida shelf (Neumann and Ball, 1970; Grasmueck et al., 2006). Along the northern side of CSB, the FC meanders and forms cyclonic frontal eddies. These eddies force a part of the FC to bend southwards into the Santaren Channel (Lee et al., 1995). Currents flow with a velocity of about 60 cm/s along the windward slope of CSB (Lüdmann et al., 2016) (Fig. 3.1A), and north directed contour currents with a speed of ca. 120 cm/s below 500 m water depth flow along the eastern flank of the SC (Leaman et al., 1995, Lüdmann et al., 2016). This current merges with the FC at the confluence of the Santaren Channel and the Straits of Florida (Fig. 3.1A). The west-directed surface currents are responsible for the distribution of sediments and the prevailing off-bank transport to the western leeward side of the Bahamian carbonate platforms (Hine and Steinmetz, 1984). The surface current system is the result of the interaction between ocean and trade-wind-driven currents. Numerical models indicate a prevailing west to northwest-directed surface current in the study area (Wang and Mooers, 1997; Kourafalou and Kang, 2012).

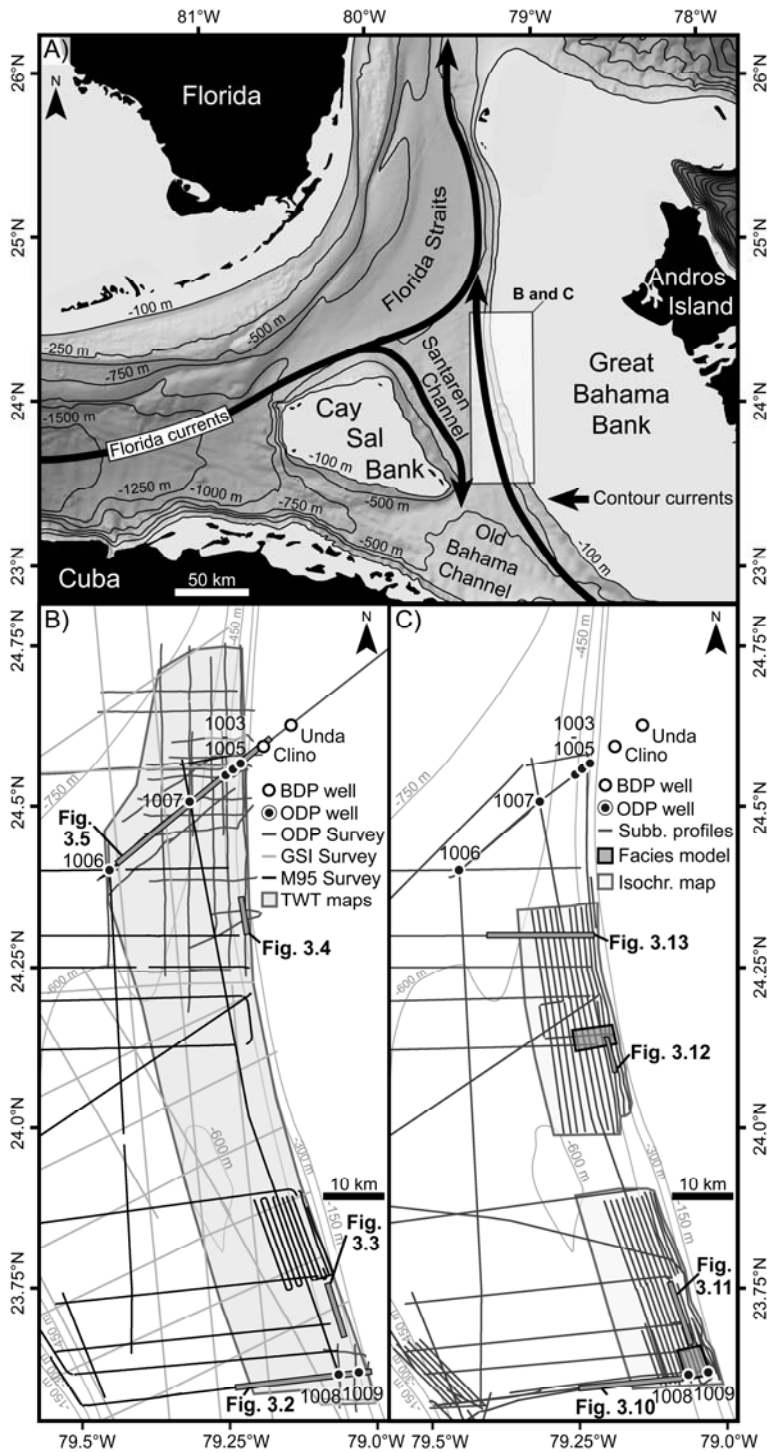


**Fig. 3.1:** A: Location of the study area. Prevailing directions of contour currents are marked with arrows. Current data after Lee et al., 1995; Leaman et al., 1995; Bergman et al., 2010; Lüdmann et al., 2016. Box shows the outline of the study area shown in B and D **B:** Study area within the Santaren Channel. Gray and black lines indicate reflection seismic profiles; ODP leg 166 sites 1003 to 1009 are marked with black, white-rimmed points; well positions of the Bahamian Drilling Program are indicated by white, black-rimmed points. Coverage of contour maps (Fig. 3.8) is indicated by grey shading. **C:** Black lines show the position of high resolution subsurface profiles; light-gray rectangles indicate the positions of the isochore maps (Fig. 3.14); dark-gray rectangles show the positions of the stochastic facies models (Figs. 3.16; 3.17).

### 3.3 Material and methods

#### 3.3.1 Geophysical data

Twenty-seven reflection seismic lines were acquired in 2013 during cruise M95 with R/V Meteor (Fig. 3.1B). The data were recorded with a 144-channel digital streamer with active length of 600 m (Hydrosience Technologies Inc., Mineral Wells, Texas, USA). The seismic array consisted of a standard and a mini GI gun (Sercel, Houston, Texas, USA) with

a total volume of 3.2 liters, ran at 150-180 bar. Shot interval was 12.5 m at a survey speed of 5 kn. Data were processed using ProMax (Halliburton-Landmark, Houston, Texas, USA) to zero phase, filtered in time and f-k domain, and corrected for dip and normal moveout. For stacking, a bin size of 6.25 m was selected. Finally, migration in time domain was carried out. Additionally, the M95 data set was combined with two older data sets to enhance the seismic grid. The first, a low resolution industrial survey was acquired by Geophysical Service Inc., using a 3.200 m long, 96-channel streamer and shot with a 2.015 in<sup>3</sup> airgun. The second data set is high-resolution survey using a 45/105 in<sup>3</sup> airgun and recorded with a 24-channel streamer. Details of the acquisition and processing are given in Anselmetti et al. (2000).

High-resolution subsurface data were recorded with a parametric sediment echosounder (PARASOUND P70, Atlas Elektronik, Bremen, Germany) (Fig. 3.1C). The system was operated with two frequencies (18 kHz and 22 kHz). The software PS32segy (Hanno Keil, University of Bremen, Germany) was used to cut and convert the data. Data processing was performed with the software package ReflexW (Sandmeier Software, Karlsruhe, Germany), comprising automatic gain control (AGC) and amplitude normalization along the profile. For visualization and interpretation, sub-bottom and reflection seismic data were loaded into Petrel E&P (Schlumberger, London, UK).

### 3.3.2 Bathymetric data

Bathymetric data were recorded with the hull-mounted Multibeam system EM122 (Kongsberg Maritime, Kongsberg, Norway), which uses a sonar frequency of 12 kHz, 432 beams and 864 soundings per ping. The system was operated with 140° sector coverage and equidistant sounding spacing. Beams were stabilized for roll, pitch and yaw. The software Caris HIPS & SIPS (Caris, Fredericton, Canada) was used for data processing and gridding (7.5 m cell size). Backscatter intensities were processed to estimate the acoustic properties of the surface sediments (c.f. Wunsch et al., 2016). The backscatter intensities were draped as a sonar mosaic onto the bathymetric grids for visualization. The software package Fledermaus (QPS, Zeist, The Netherlands) was used for data visualization and interpretation.

### 3.3.3 Stochastic facies modeling

To reconstruct lateral facies changes, stochastic modeling was performed by using the sequential indicator simulation with the software package Petrel E&P (Schlumberger, London, UK). The code is provided in the Geostatistical Software Library (GSLIB) and is

based on the indicator approach (Journel, 1983; Jaime Gomez-Hernandez and Mohan Srivastava, 1990; Deutsch and Journel, 1998). The indicator approach transforms each facies into a new variable, and the value of each variable corresponds to the probability of finding the related facies at a given position. This stochastic method is normally used to model heterogeneities (facies distribution, porosity, permeability) in hydrocarbon reservoirs. Input data for stochastic modeling are based on both the hydroacoustic data and the sedimentological data of ODP Leg 166 (Eberli et al., 1997) amended with grab and box core data (Wunsch et al., 2016) as well as gravity core data from Cruise M95 CICARB. Seven seismic facies were defined by correlating the sedimentological information typical the reflection patterns in the high-resolution subsurface data and linked to a specific sediment texture classified after Dunham (1962) and Embry & Klovan (1971). To extend the sedimentological information, synthetic wells were created. Each synthetic well provide an interpretation of the sedimentological section based on these seismic facies.

### **3.4 Results**

#### **3.4.1 Major deposit types and general reflection pattern**

Based on the seismic reflection patterns, Anselmetti et al. (2000) defined two major types of deposits in the slope-to-basin transition of leeward slope of the GBB: slope deposits and drift deposits. Slope deposits, consisting of inclined discontinuous to moderately continuous reflections of low to medium amplitude (Fig. 3.2) that across strike appear as discontinuous subparallel reflections of low to high amplitude (Fig. 3.3). Channel incisions with cut-and-fill structures occur at different stratigraphic levels (Fig. 3.4). Texturally, the slope deposits are composed of mudstone, wackestone, packstone, and grainstone with interbedded floatstone layers that result of a wide spectrum of depositional processes, from pelagic fall-out to turbiditic flow (Eberli et al., 1997; Betzler et al., 1999; Bernet et al., 2000). Basinwards, slope deposits interfinger with the drift deposits of the Santaren drift (Bergman et al., 2005). In the reflection seismic data, the drift deposits are imaged as continuous and parallel reflections of low to high amplitude (Anselmetti et al., 2000) (Fig. 3.5). At ODP Site 1006, these drift deposits consists of mudstone or lithified mud- to wackestone with intercalated clay layers (Eberli et al., 1997). Mass transport complex (MTC) deposits were later recognized as a third type of slope-to-basin deposits (Principaud et al., 2016). The MTC deposits form lenticular packages with a chaotic internal reflection pattern, often intercalated between the slope deposits and the drift deposits (Figs. 3.2; 3.5). Cores from ODP sites 1007 and 1008 indicate that these MTC deposits consist of peloidal coarse-

grained and mud- to grain-dominated floatstones with slump structures (folded beds) and clasts (Fig. 3.6) (Eberli et al., 1997; Bernet et al., 2000).

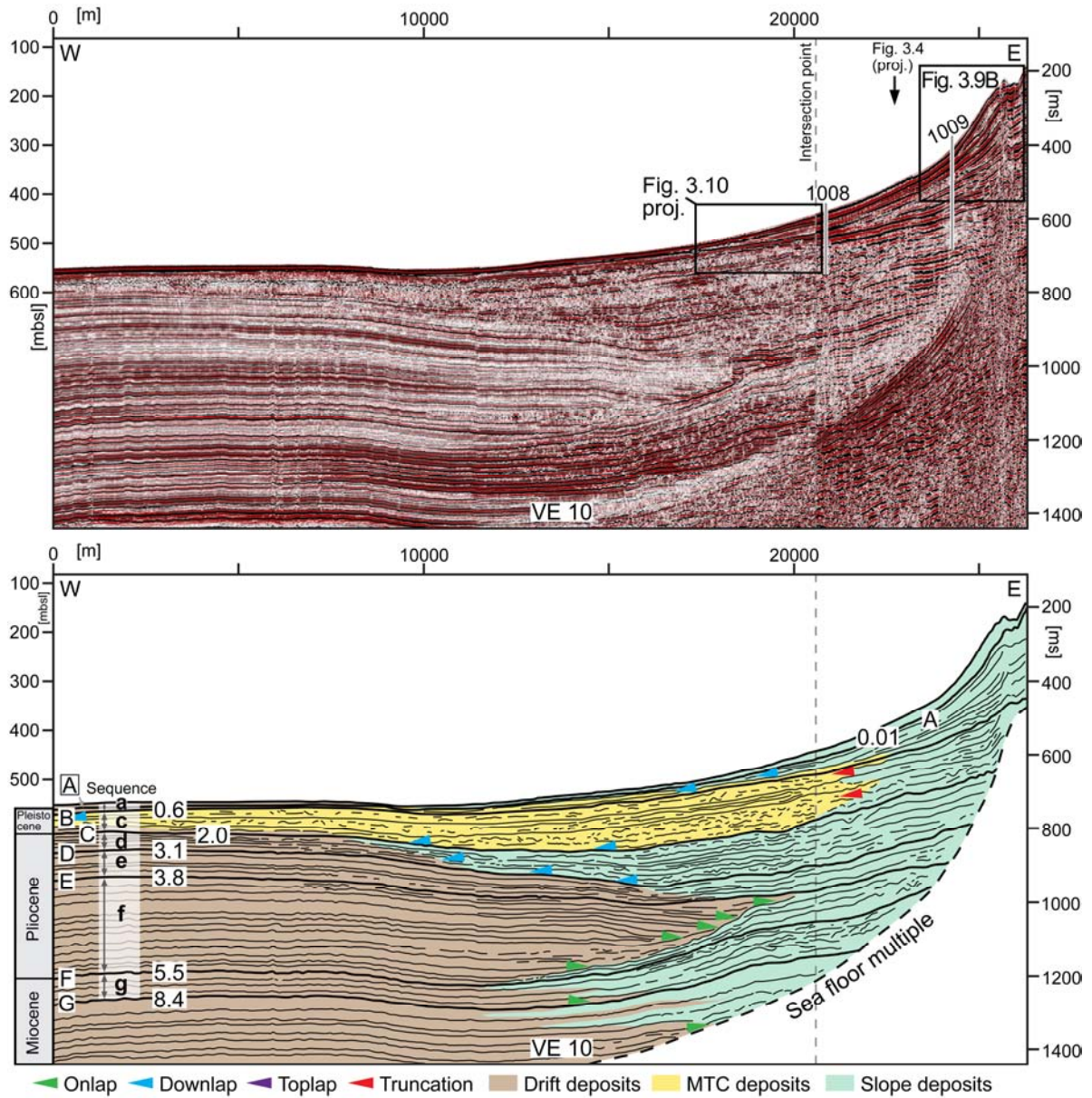


**Fig. 3.2:** Along-slope composite seismic profile from the southern working area and interpretation below. The dashed line indicates the intersection point. See Figure 3.1B for location. Seven seismic sequence boundaries (SSBs) (A to G) were defined following the nomenclature of Eberli et al. (1997). The ages of the SSBs are given in million years (Ma) and were determined based on calcareous nannofossil and planktonic foraminifer events. These seismic sequence boundaries delimit seven seismic sequences (a to g). Black rectangle indicates the projected position of Figures 3.9B and 3.10. Based on the seismic reflection patterns, three major deposit types form the slope-to-basin transition. The first type, the slope deposits (green), documents the deposition of platform material onto the leeward slope. Slope deposits generally consist of inclined discontinuous to moderately continuous reflections of low to medium amplitude. Basinal deposit type is formed by drift deposits (brown). The drift deposits are part of the Santaren drift, which consists of continuous and parallel reflection of low to high amplitude. The third major deposit type is formed by the MTC deposits (yellow). The MTC deposits are generated by large slope failures and form lenticular packages with a chaotic internal reflection pattern.

### 3.4.2 Sequence stratigraphic framework

This study concentrates on the upper seven third-order seismic sequences (g to a) and corresponding seismic sequence boundaries (SSBs) A to G defined by Eberli et al. (1997, 2002) (Figs. 3.2, 3.7A; Tab. 3.1); Sea floor multiples prevent clear imaging of deeper parts of the sedimentary succession. The age assignment of the SSBs relies on calcareous nannofossil and planktonic foraminifer events (Eberli et al., 1997; 2002; Kroon et al., 2000; Wright and Kroon, 2000), herein updated to the time scale of Gradstein et al. (2012) (Fig. 3.7A; Tab. 3.1). The high-resolution hydroacoustic data allow describing four additional sequences of higher order (b1 to b4) within seismic Sequence b (Fig. 3.7B; C). These high-order sequences are delimited by prominent high-amplitude single reflections (B1 to B4) (Figs. 3.7B; C; Tab. 3.1). Correlation to the succession at ODP sites 1006 and 1008 corroborate that the intervals are composed of sediments with a high aragonite content and light stable oxygen isotopes, whereas the bounding reflections correspond to changes in sediment composition or lithification, which cause the changes in the acoustic impedance (Figs. 3.7B; C).

SSB	Age (Ma)*	1003		1004		1005		1006		1007		1008		1009	
		TWT (ms)	Depth (mbsf)												
A	~0.02	16	13	20	16	24	19	4	2.5	3	2	7	6	26	21
B4	~0.18	/	/	26	21	41	33	8	6	/	/	12	12.5	50	40
B3	~0.27	/	/	46	37	64	51	/	/	/	/	24	20	86	69
B2	~0.36	18	14	58	46	81	65	18	18.5	14	11	36	27	102	81.5
B1	~0.45	27	21	/	/	96	77	25	21	/	/	48	40	118	94.5
B	0.6	28	23	73	68	100	90	33	30	15	12	63	63	138	126
C	2.0	117	107	165	153	219	201	100	90	35	40	N.D.	N.D.	N.D.	N.D.
D	3.1	150	145	200	185	244	228	160	145	220	210	N.D.	N.D.	N.D.	N.D.
E	3.8	171	166	N.D.	N.D.	275	259	190	170	210	220	N.D.	N.D.	N.D.	N.D.
F	5.5	315	315	N.D.	N.D.	387	385	410	380	303	303	N.D.	N.D.	N.D.	N.D.
G	8.4	340	350	N.D.	N.D.	430	430	530	505	350	365	N.D.	N.D.	N.D.	N.D.

**Table 3.1:** Summary of the seismic sequence boundaries (SSB). \*Ages defined from Biostratigraphic data, U/Th data of ODP core 1006 and 1008, respectively. /= Not detected N.D.= Not drilled. Ages were updated with the time scale of Gradstein et al. (2012).

### 3.4.3 The seismic sequences

#### 3.4.3.1 Sequence g

Sequence g is bounded at its base and top by seismic sequence boundary (SSB) G and F, respectively. In our data, the lower foreset and the bottomset of the prograding sequence are imaged (Fig. 3.2). At the toe of slope, the slope deposits gradually pass into the drift

deposits (Figs. 3.2; 3.5). Slope and drift deposits show nearly the same thickness around the slope-to-basin transition (Fig. 3.2). In the northern part, the slope deposits thin towards the modern platform margin (Fig. 3.5). Minor cut-and-fill structures dissect the slope deposits in the proximal parts of the slope. Major cut-and-fill structures characterize the upper seismic sequence boundary F (Figs. 3.3; 3.4).

#### **3.4.3.2 Sequence f**

Sequence f is delimited at its base by SSB F, which deepens towards the west (Fig. 3.8A). The sequence comprises an approximately 200 m thick package of drift deposits in the basinal portion, which progressively migrates eastward within the sequence while the coeval slope deposits are thin along the toe of slope (Fig. 3.5). The lowermost part of the succession within Sequence f interfingers with slope deposits, whereas the upper part of the drift deposits onlap the slope deposits. The migration pattern of the drift deposits varies from north to south. In the south, the internal reflections of the drift deposits show downbending onlap configurations and a continuous upslope migration (Fig. 3.2). In the north, the internal reflections converge towards the base of slope (Fig. 3.5). The drift migration and the thinning of the slope deposits along the base of slope created a north-northwest to south-southeast striking depression that shallows towards the south where migration is less pronounced (Fig. 3.8B).

#### **3.4.3.3 Sequence e**

The base of the sequence, SSB E, is an erosional unconformity with channels that cut into the underlying Sequence f (Fig. 3.4). These cut-and-fill structures coincide with a decrease in thickness of the slope deposits. More basinwards, the slope deposits wedge out and the mound-shaped drift deposits directly onlap SSB E. Towards the south, the slope deposits thicken and form a wedge that pass basinwards into the drift deposits (Figs. 3.2; 3.3). At the transition, both facies show nearly the same thickness (Fig. 3.2).

#### **3.4.3.4 Sequence d**

Sequence d lies above SSB D, which is irregular and forms channel-shaped incisions in the northern part of the study area (Fig. 3.4). These incisions coincide with large MTC deposits and a thinning of the slope deposits (Fig. 3.5). In dip direction, slope deposits form lenticular bodies that backfill the north-northwest to south-southeast striking depression at the toe of slope (Figs. 3.5; 3.8C). More basinwards, MTC deposits intercalate with the drift deposits (Fig. 3.5). Towards the south, the slope deposits form a wedge, which downlap onto the drift deposits (Fig. 3.2).

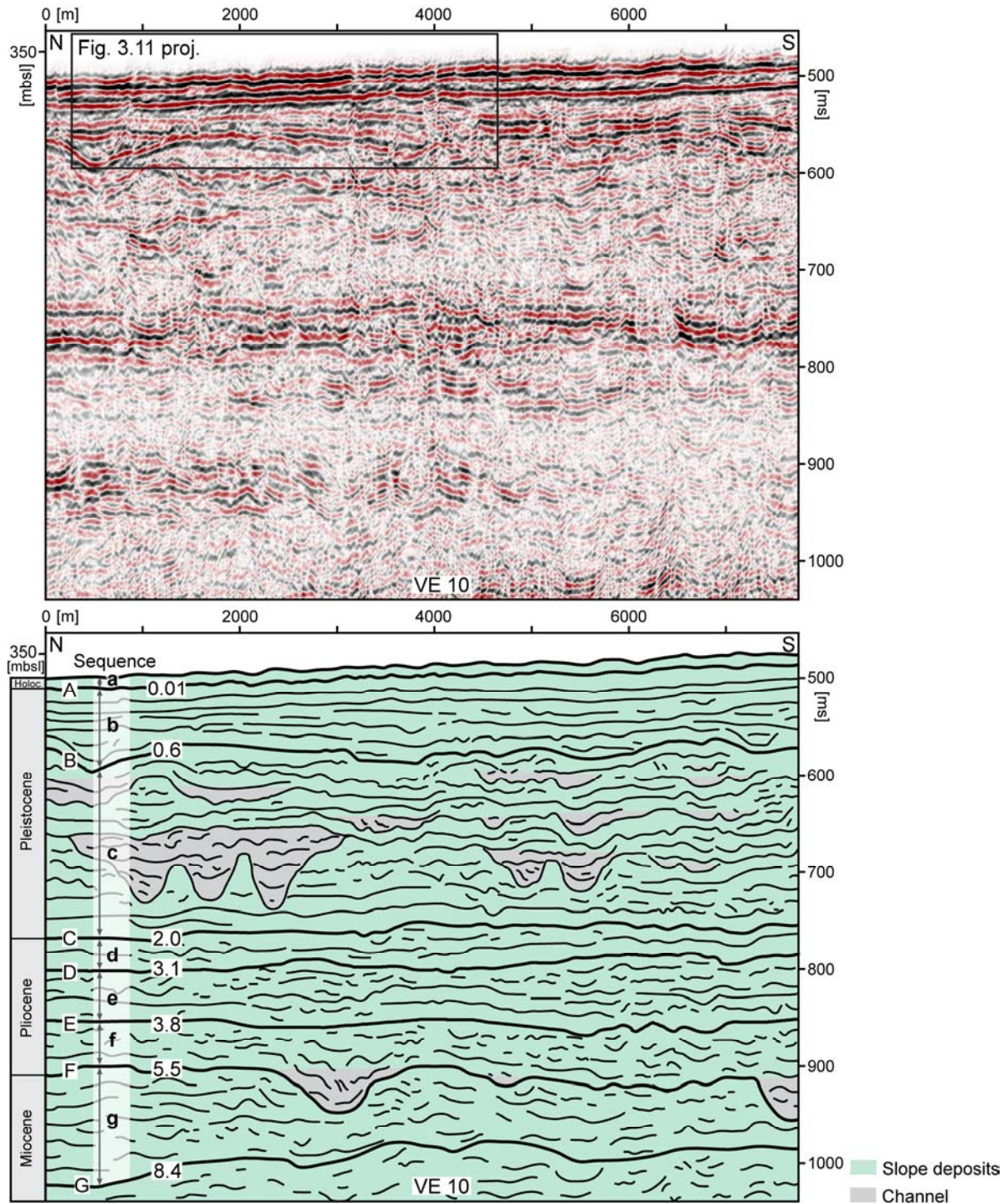


**Fig. 3.3:** Across-strike seismic profile from the southern working area and interpretation below. Profile location is indicated in Figure 3.1B. Black rectangle indicates the projected position of Figure 3.11. The slope deposits (green) occur as subparallel discontinuous reflections. Channels (grey) cluster along sequence boundary F and within Sequence c. These channels show a divergent filling pattern.

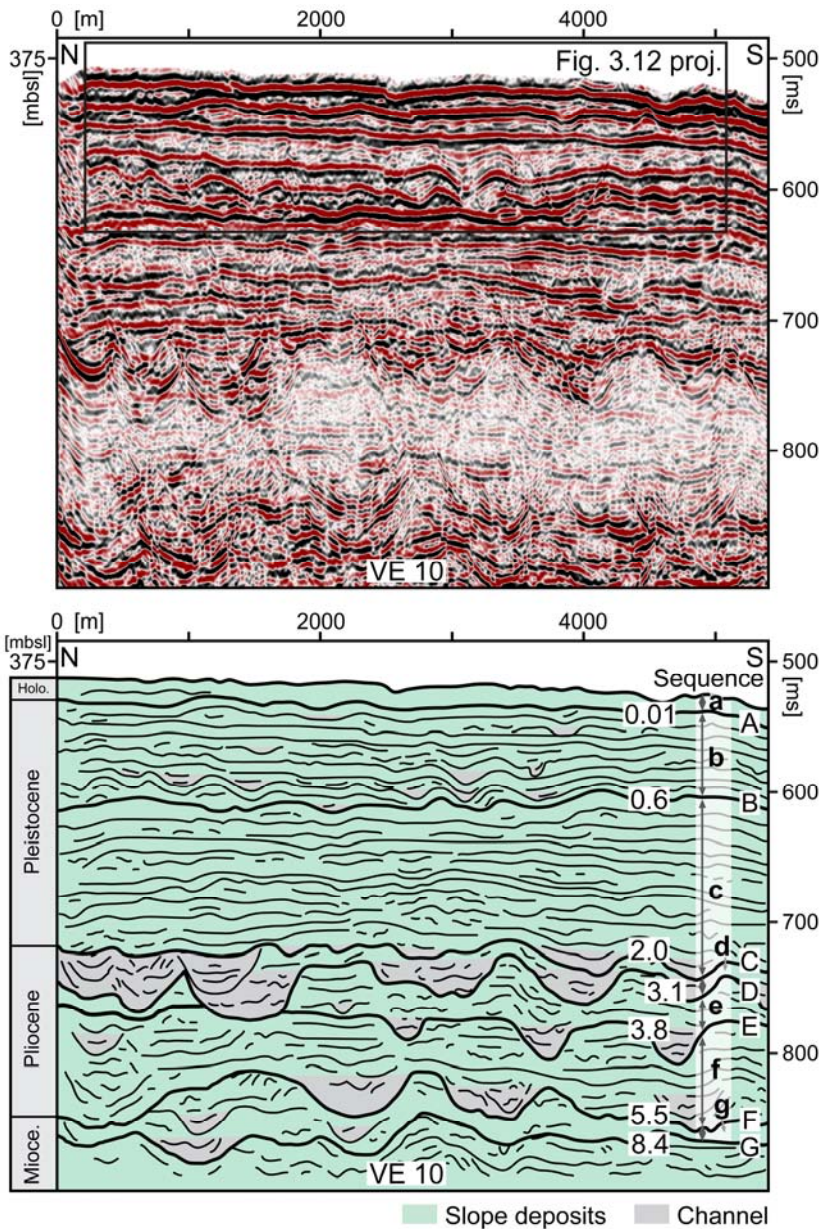


**Fig. 3.4:** Across-strike seismic profile from the northern part of the working area (interpretation below); for location see Figure 3.1B. Black rectangle indicates the projected position of Figure 3.12. The slope deposits (green) occur as subparallel discontinuous reflections, which are dissected by channels (grey). Channels are more frequent along sequence boundaries G to C. Minor channel incision occurred during the formation of sequence b. The channels show a divergent to chaotic filling pattern.

### 3.4.3.5 Sequence c

The lower seismic sequence boundary (SSB C) is dissected in the northern part by cut-and-fill structures and deepens towards the west and northwest (Figs. 3.4; 3.8C). In the northern part, the slope deposits form a wedge that interfinger with the MTC deposits towards the basin (Fig. 3.5). The internal reflections of the wedge are in parts truncated by the MTC deposits and the upper seismic sequence boundary (SSB B) (Fig. 3.5). In the southern part, MTC deposits partly truncate the slope deposits (Fig. 3.2). In the proximal parts of the slope, cut-and-fill structures of various size dissected the slope deposits and yielding an irregular reflection pattern (Fig. 3.3).

### **3.4.3.6 Sequence b**

The lower bounding SSB B deepens towards the west and northwest (Fig. 3.8D). Sequence b forms a wedge, which intercalates with MTC deposits at the toe of slope (Figs. 3.2; 3.5). During formation of the higher order sequences b1 to b4, the platform margin prograded westward and continuously steepened (Fig. 3.9A). Beneath the margin, every sequence has a wedge of slope deposits with a margin-parallel ridge and an adjoined depression (Fig. 3.9B). Internally, every individual wedge shows the same characteristics and features but with changes along strike. These changes are also visible in the recent sea-floor morphology. In the southern part, the sea floor is occupied by a strike-continuous field of cyclic steps (Betzler et al. 2014) (Fig. 3.10A). In the subsurface data, the slope deposits appear as relatively transparent intervals. The seismic sequence boundaries are continuous and appear wavy in the proximal part of the wedge (Fig. 3.10B; C). The cyclic steps are locally interrupted by shallow furrows (Fig. 3.11A; B). In the margin-parallel profiles, SSB B1 and B2 appear irregular and form shallow depressions (Fig. 3.11B). By contrast, the overlying SSBs (B3 to B4) are flat horizons. Within sequences b3 and b4, the lower sequence boundaries are each overlain by a high-amplitude single reflection, which mimics the actual sequence boundary (Fig. 3.10C). Towards the north, the sea floor is characterized by gullies and a patchy distribution of cyclic steps (Fig. 3.12A). The margin-parallel profiles exhibit cut-and-fill structures that cluster along the sequence boundaries (Fig. 3.12B). These cut-and-fill structures show a chaotic to divergent filling pattern (Fig. 3.12C). The abundance of these cut-and-fill structures along the SSBs leads to an irregular and discontinuous appearance of the SSBs. In parts, the sequence boundaries B2 to B4 are truncated by SSB A, which is represented on the recent sea floor by scarps (Figs. 3.12B; 3.13A-C). At its toe, the slope is overlapped by MTC deposits, which intercalated with the drift deposits basinwards (Fig. 3.13B; D). This change along the strike of the slope is also visible in the isochore maps (Fig. 3.14). In the whole study area, Sequence b1 displays an irregular distribution, with areas of increased sediment thickness in the proximal and distal parts of the slope (Fig. 3.14A). In the southern part, this pattern changes during Sequences b2 to b4. The slope deposits form a distinct wedge, which thins out approximately 7 km away from the recent platform margin (Fig. 3.10B; 3.14B to D). In the northern part, the sediment distribution is intermittent and patchy in all sequences (Fig. 3.14A to D).

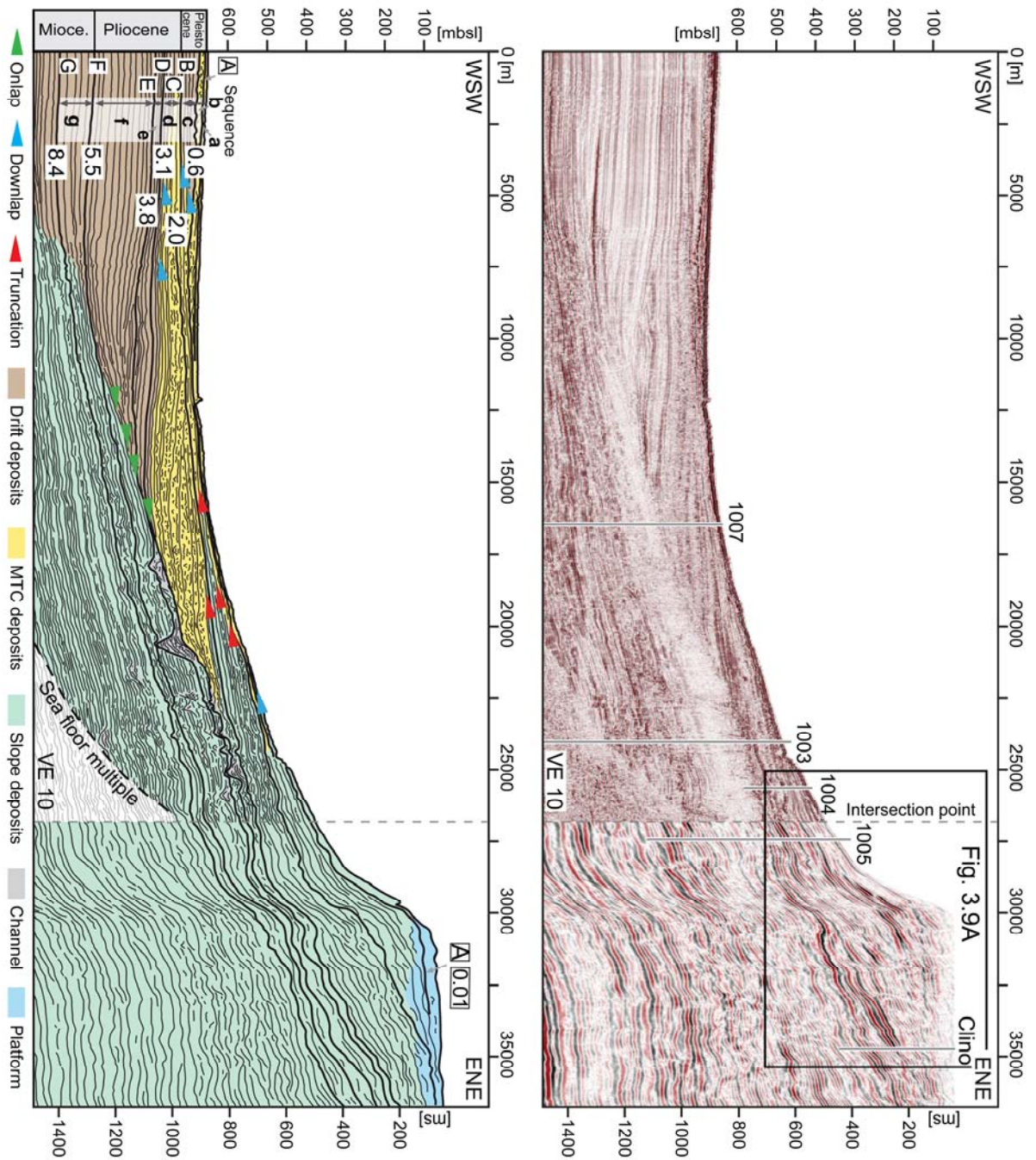


**Fig. 3.5:** Along-slope composite seismic profile from the northern working area and interpretation below. The dashed line indicates the intersection point; see Figure 3.1B for location. Black rectangle indicates the projected position of Figure 3.9A. The ages of the SSBs are given in million years (Ma). From sequence f on, the drift deposits (brown) progressively onlap and migrated eastwards accompanied by a thinning of the slope deposits (green) along the toe of slope. Major events of MTC deposit accumulation occur during the formation of sequences d to a.

### **3.4.3.7 Sequence a**

Sequence a is bordered at its base and top by SSB A and the recent seafloor, respectively. The sequence has similar characteristics as Sequences b1 to b4. To the south, it forms a smooth sedimentary wedge, which thins out approximately 7 km from the platform margin (Figs. 3.10; 3.14E). In the northern part, the sediment thickness increase in the proximal parts of the slope (Fig. 3.14E). In its proximal part, the slope is lined by a margin-parallel depression, which is bordered basinwards by a ridge (Fig. 3.9B).

### **3.4.3.8 Stochastic models**

Sediment surface samples and core data were correlated with the high-resolution hydroacoustic data to define a series of seismic facies, which are subdivided into seismic packages and seismic surfaces (Fig. 3.15). The seismic facies were used to develop two stochastic models, which show the differences in the facies distribution between the northern and southern part of the slope. Both models emphasize the spatial facies heterogeneities within the sequences b1 to a. The positions of both models are indicated in Figure 3.1C.

The southern stochastic model covers a slope area of 20.4 km<sup>2</sup> and integrates sedimentological data of ODP wells 1008, 1009, and 13 synthetic wells (Fig. 3.16). Within sequence b1, the facies distribution varies in downslope and along-strike direction. Sequence b1 is dominated by mudstones and packstones, which interfinger with small lenses of wackestone or wacke- to packstone. The overlying sequences (b2 to a) show a layer-cake stratigraphy along strike with little lateral facies changes. Major facies alternations occur predominantly in downslope direction. Within the sequences, the dominating facies are mudstone, mud- to wackestone, wackestone and packstone. Wacke- to packstones and pack- to grainstones and grainstones are restricted to the uppermost parts of the sequences below.

The area for the second stochastic model is located in the northern part of the study area and covers 29.8 km<sup>2</sup> (Figs. 3.1C; 3.17). This model integrates the sedimentological data of three gravity cores, one multicore and one box core, extended by nine synthetic wells. Compared to the model on the southern slope, the northern model exhibits a more irregular facies distribution. Rapid facies alternations occur in downslope and along-strike direction. Cut-and-fill structures form a complex pattern of isolated facies bodies, which are bounded by the SBBs. The filling of the cut and fill structures is dominated by wackestone and wacke-

to packstone. Within the individual sequences, deposits are dominated by wackestones (Fig. 3.17), intercalated with lenses of wacke- to packstones and mud- to wackestones.

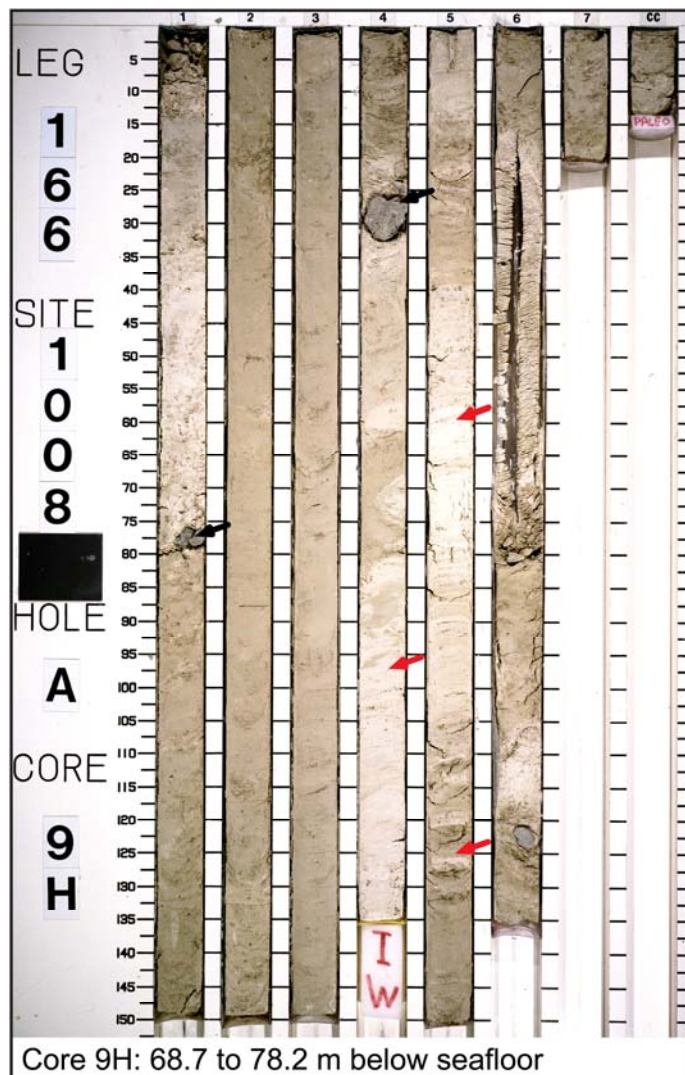


**Fig. 3.6:** Core photo from ODP site 1008A, core 9H. The core site was located in a water depth of 437 m. The upper part of the succession (Section 1 and 2) consist of unlithified peloidal wackestone. Sections 3 to 7 consist of peloidal mudstone to wackestone. According to the biostratigraphic age model of ODP core 1008A, the sediments deposited during the Mid-Pleistocene (Eberli et al., 1997). Black arrows mark large lithoclasts. Red arrows indicate slump structures within the sedimentary succession. Photo source: Scientific party of ODP Leg 166; IODP/TAMU - Janus Web Database.

### 3.5 Discussion

#### 3.5.1 Slope development since the Late Miocene

##### 3.5.1.1 Sequence g (8.4 Ma-5.5 Ma)

During the Late Miocene, the fluctuating sea level was the main controlling mechanism for deposition and erosion along the leeward slope of Great Bahama Bank. The slope deposits are generally thicker than the basinal drift deposits, indicating a concentration of the deposition on the slope and low current velocities (Anselmetti et al., 2000). Large erosional events, which affect the complete slope, are predominantly triggered by relative sea-level falls (Eberli, 2000). A sea-level drop about 5.5 Ma ago, caused the incision of large channels along the complete leeward slope (Eberli, 2000) (Figs. 3.3; 3.4; 3.18A).

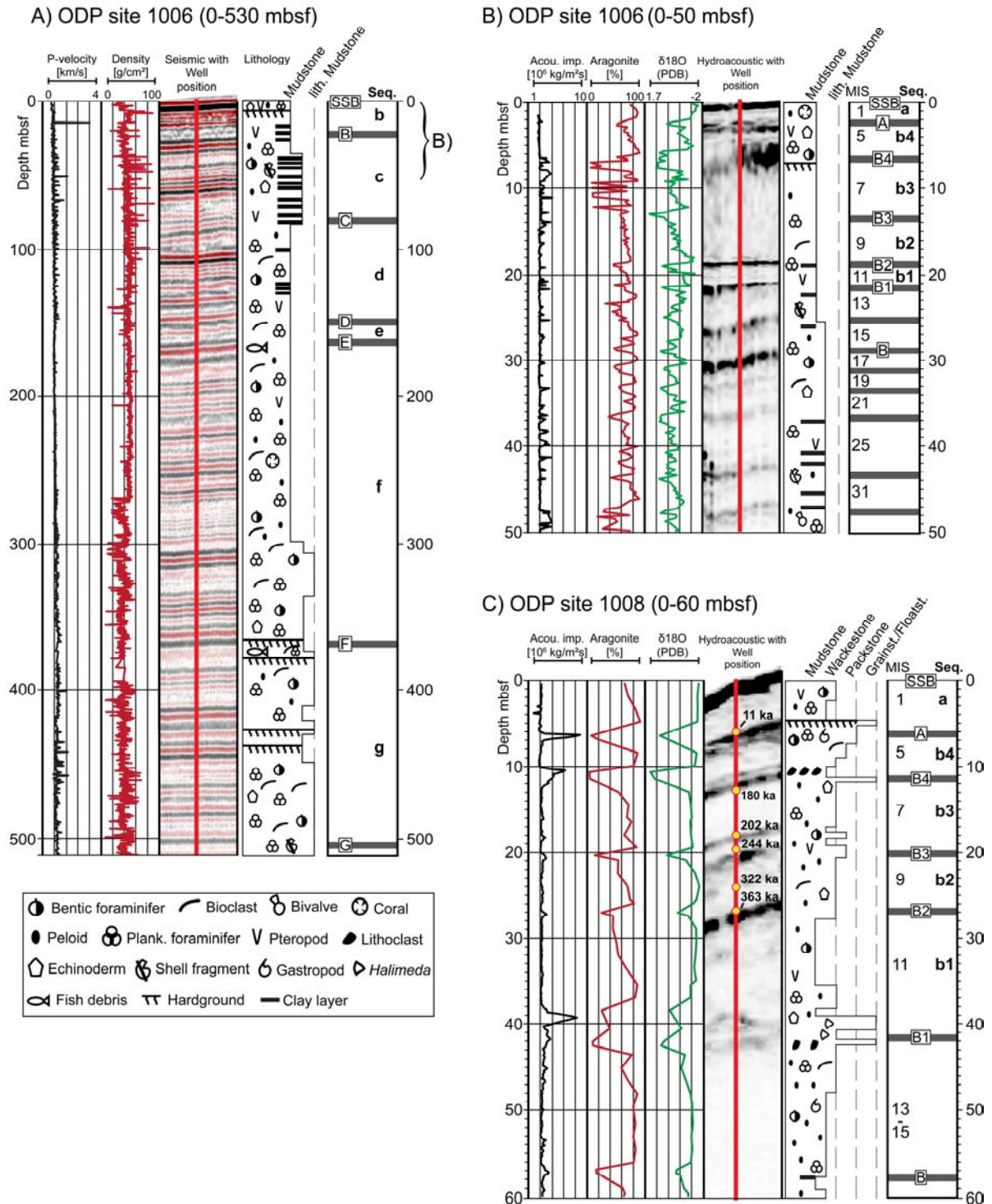


**Fig. 3.7:** Well to seismic ties of the ODP Sites 1006 and 1008. **A:** Well to seismic tie of ODP well 1006, which is located at a water depth of 657 m. The correlation shows that the reflections of the seismic sequence boundaries are produced by sharp changes in the sedimentary succession. In the basal succession of ODP core, the reflections are produced by clay layers intercalated in mudstone. Density, sonic velocities and lithology column are taken from Eberli et al. (1997). **B:** Correlation between the subsurface data and the upper 50 m of ODP well 1006. Aragonite content and stable oxygen isotope data are taken from Kroon et al. (2000). Lithology column is taken from Eberli et al. (1997). **C:** Correlation between the subsurface data and ODP well 1008, which is located at a water depth of 437 m. Aragonite content and stable oxygen isotope data are taken from Malone (2000). Lithology column is from Eberli et al. (1997). The yellow circles indicate position of U/Th ages measured by Robinson et al. (2002) and Henderson et al. (2006).

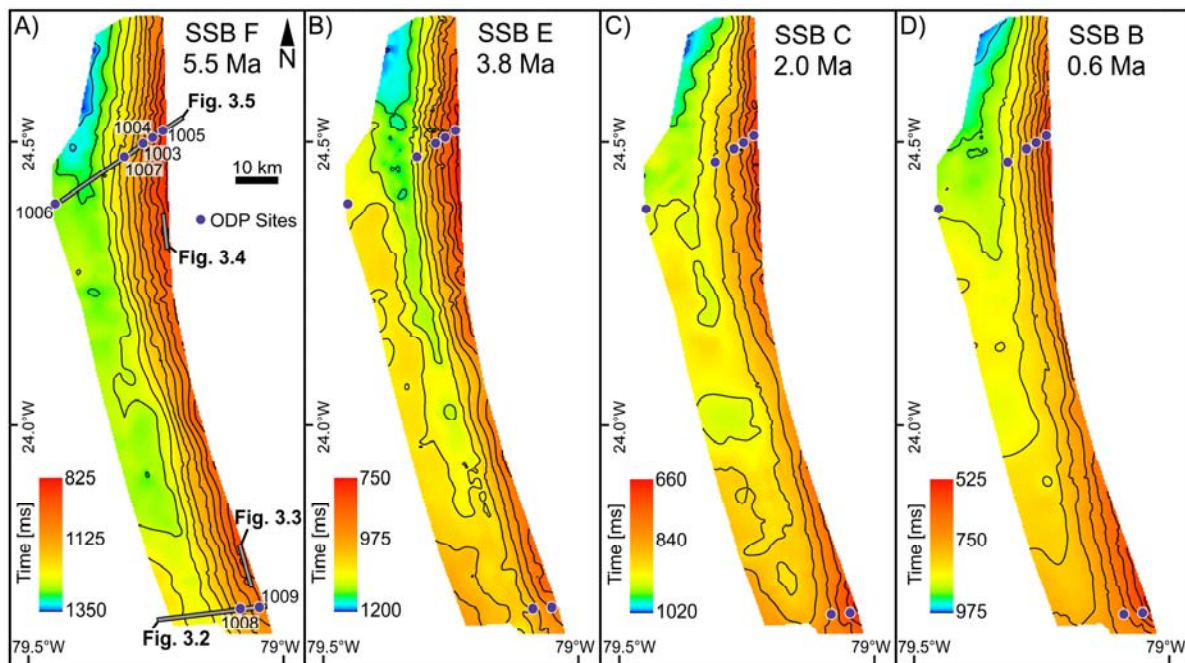


**Fig. 3.8:** Contour maps generated from the reflection seismic data by mapping the seismic boundaries (SSB) F, E, C and B.

### 3.5.1.2 Sequence f (5.5 Ma-3.8 Ma)

Since the Messinian, the intensification of the north-directed contour currents and a contemporary increased sediment input to the basin induced an eastward migration of the Santaren drift, which started to onlap the slope deposits (Fig. 3.18B) (Anselmetti et al., 2000). The migration pattern of the Santaren drift varies along strike. In the south, the Santaren Drift migrated continuously upslope without the formation of a deep moat. In the north, drift migration was accompanied by the formation of a deep moat along the toe of slope, restricted to the area where the north-directed contour currents of the Santaren Channel merge with the FC (Figs. 3.5; 3.8B; 3.18B). The drift migration is consistent with an intensification of the FC, which exceeded modern conditions (Kaneps, 1979; Haug et al., 2001; Steph et al., 2006; 2010). The intensification was caused by the gradually closure of the Central American Seaway between 4.6 to 3.6 Ma (Haug and Tiedemann, 1998). The changes in the current regime exerted an increased current control on slope architecture. During the lower Pliocene, moat indentation was accompanied by a winnowing of sediments along the toe of slope and resulting reduced sedimentation rates (Wright and Kroon, 2000). Furthermore, winnowing oversteepened the toe of slope and triggered the incision of channels that were subsequently filled with platform material (Figs. 3.4; 3.5). The continuous oversteepening of the toe of slope finally triggered headward eroding of slope failures and the incision of larger v-shaped channels (Figs. 3.4; 3.5). In the northern part, at the toe of slope, this erosional event correlates with a 0.4 Ma hiatus in the succession

of ODP core 1007 (Wright and Kroon, 2000). A sea-level fall as potential trigger mechanism of the channel incision can be excluded, because the oxygen isotope data show no evidence of a major sea-level drop during this time period and the platform top was an area of high productivity (Kenter et al., 2001; Reijmer et al., 2002).

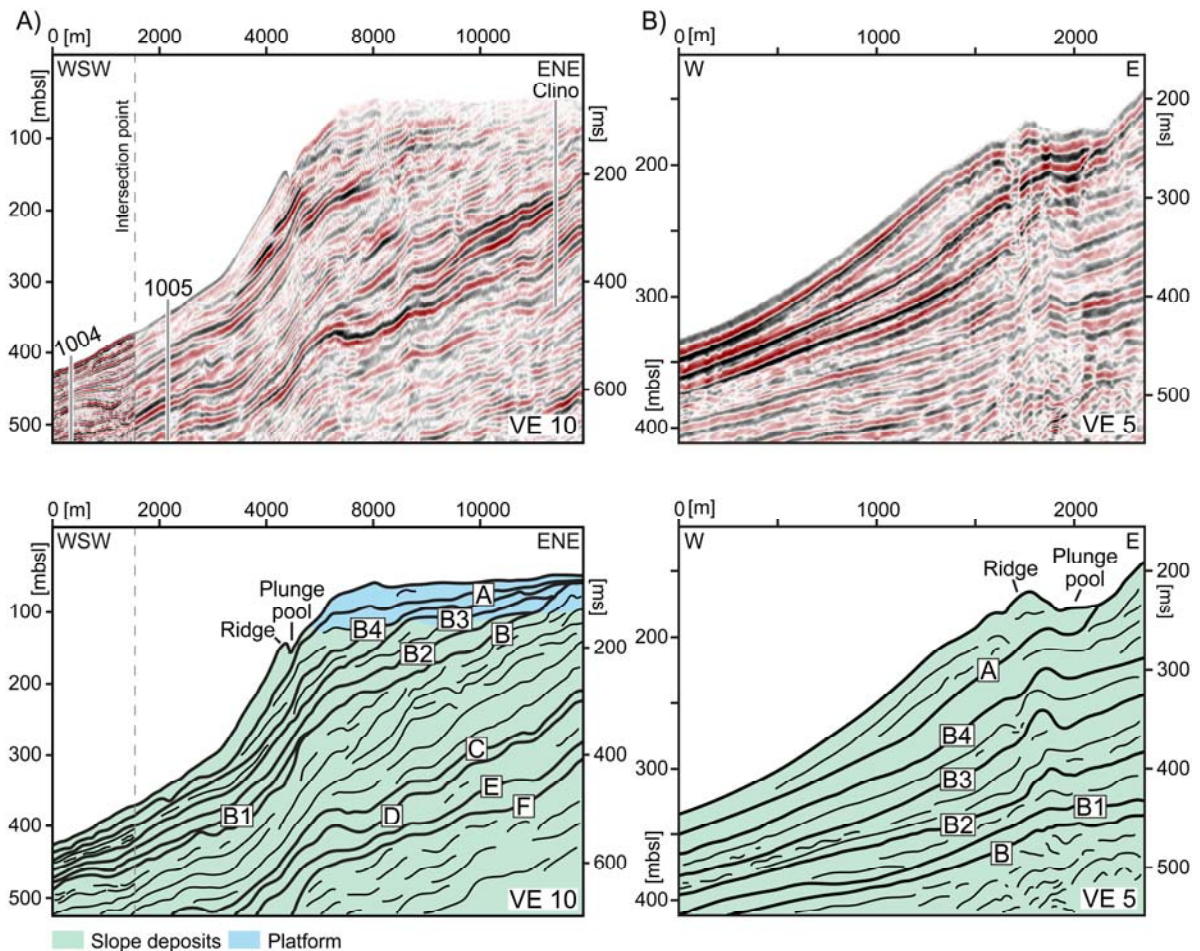


**Fig. 3.9:** **A:** Seismic profile from northern working area (interpretation below), which run across the platform margin. See Figure 3.6 for location. The platform margin show a continuous steepening since the onset of the sequence b, discussed in text. **B:** Seismic profile from the southern working area and interpretation below, see Figure 3.2 for location. The profile shows a closer view on the plunge pool and adjoined sedimentary ridge. Sequence b marks the onset of the plunge pool and ridge formation, see text for discussion. The position of both structures is relatively stable since they were formed.

### 3.5.1.3 Sequence e (3.8-3.1 Ma)

During the early stages of Sequence e, continued eastward migration of the Santaren drift was restricted to the northern part of the study area and the drift deposits formed a smaller mound-shaped body within the moat axis (Figs. 3.5; 3.18C). This decreased rate of drift migration is likely the sedimentary expression of the contemporaneous deceleration of the FC caused by a weaker thermohaline circulation in the Northern Atlantic (Kaneps, 1979;

Raymo et al., 1996; Billups, 2002). In the Bahamian archipelago, the Pliocene was marked by a high carbonate production on the platform top and increased sediment export towards the leeward slope (Eberli et al., 1997; Reijmer et al., 2002). In the south, this led to an extensive westward progradation of the slope deposits, which suppressed eastward drift migration (Fig. 3.2). In the north, increased sedimentation rates on the leeward slope leveled the pre-existing channel topography (Betzler et al., 1999; Anselmetti et al., 2000). In the late stages of the sequence development, between 3.6 and 3.2 Ma, the FC gradually accelerated and recovered to its present strength caused by the onset of the Northern Hemisphere glaciations (Kaneps, 1979; Raymo et al., 1992; Haug and Tiedemann 1998;). Triggered by the re-intensification of the FC, sediment winnowing resumed along the northern toe of slope. This winnowing caused the incision of large channels around 3.1 Ma (Figs. 3.4; 3.5; 3.18C).

#### **3.5.1.4 Sequence d (3.1-2.0 Ma)**

During the late Pliocene and early Pleistocene, the moat was filled with MTC deposits, which formed a strike continuous belt (Figs. 3.5; 3.18D) (Reijmer et al. 2002; Principaud et al., 2016). The re-enforced FC caused a toe of slope backstepping, which triggered these mass-wasting processes. The MTC deposits consist of material derived from the upper slope and platform margin, funneled by the channels, which were incised around 3.1 Ma (Eberli et al., 2004; Principaud et al., 2016). The deposition of the MTC deposits stopped after the moat was backfilled and the slope profile was leveled (Figs. 3.8C; 3.18D). The coarse-grained nature of the MTC deposits prevented the incision of a new moat. At the same time, the southern part of the leeward slope underwent extensive progradation (Sequence d; Fig. 3.2). This progradation coincides with a transition in the platform geometry from a carbonate ramp to a flat-topped platform (Fig. 3.5) (Eberli and Ginsburg, 1987; Betzler et al., 1999).

#### **3.5.1.5 Sequence c (2.0-0.6 Ma)**

The early Pleistocene was characterized by extensive progradation of the bank edge (Figs. 3.5; 3.9A). In the southern part, this progradation was accompanied by large slope failures, which formed a gullied upper slope and displaced slope material to the lower slope and toe of slope (Figs. 3.2; 3.3; 3.6; 3.18E). It is proposed that these slope failures were triggered during drops in sea level after times of high slope sedimentation rates. Emplacement of these deposits coincides the Mid-Pleistocene transition (MPT). During the MPT (1.25-0.7 Ma), sea-level variability increased in amplitude, forced by the progressively change from low- 41 ka to high-amplitude 100-ka climate oscillations (Shackleton and Opdyke, 1976;

Pisias and Moore, 1981; Clark et al., 2006; Maslin and Brierley, 2015). On the inner platform, sea-level variations resulted in the formation of several exposure horizons in the sedimentary succession (Kievman, 1998).

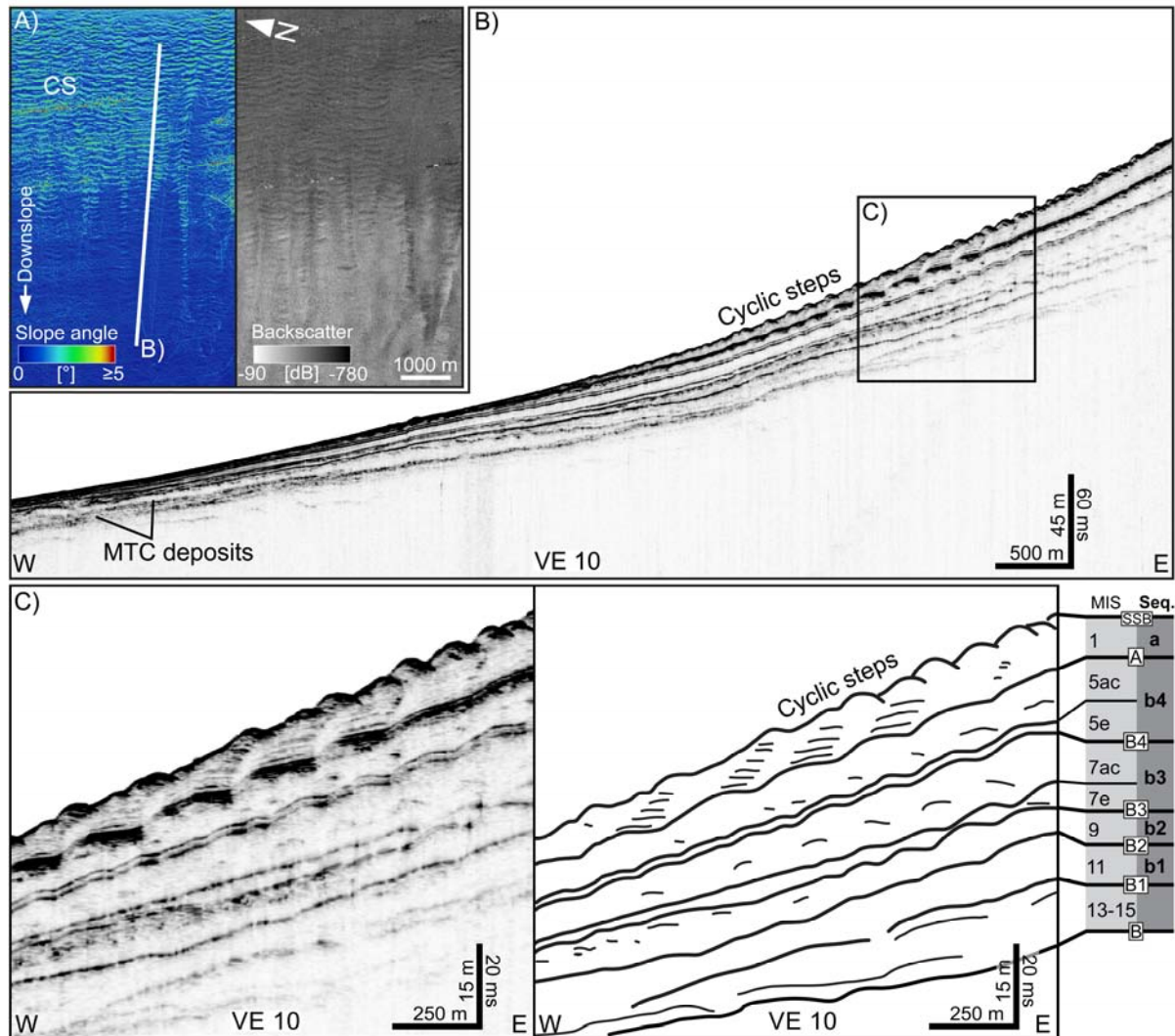


**Fig. 3.10:** A: Slope-angle steepness map and backscatter image of the southern part of the leeward slope, showing a field of cyclic steps. White line indicates the positions of the subsurface profile in B. B: Along-slope high-resolution subsurface profile; for position see Figure 3.1C. The slope deposits occur as relatively transparent wedges, which are separated by high-amplitude reflections. The wedges pinch out nearly at the same position. C: Each wedge represents a high-frequency sequence, which formed during a distinct Marine Isotope Stage (MIS) (see text for discussion). The high-amplitude reflections define the sequence boundaries. In the more proximal parts of the slope, these sequence boundaries appear wavy by the occurrence of cyclic steps.

In the north, the wedge of the slope deposits reached the position of the former moat (Fig. 3.5). A further progradation, however, was prevented by the northward flowing contour currents, which winnowed the sediments along the toe of slope (Rendle and Reijmer, 2002). The biostratigraphic data of ODP core 1007 indicate a condensed Pleistocene interval (Wright and Kroon, 2000). About 0.6 Ma ago, during a sea-level lowering, a large slope

failure occurred in the northern part of the study area (Fig. 3.18E). This slope failure originated at the lower slope and formed a scarp (headwall), which is traceable in the entire northern part of the study area (Figs. 3.13B; C; 3.18E). This slope failure removed sediments from the lower slope and deposited the material as MTC at the base of the slope and in the adjoined basin (Fig. 3.13B; C). Larger slope failures that occurred at the same time along the northwestern part of the leeward GBB-slope were related to a lowering of the sea level (Wunsch et al., 2016).

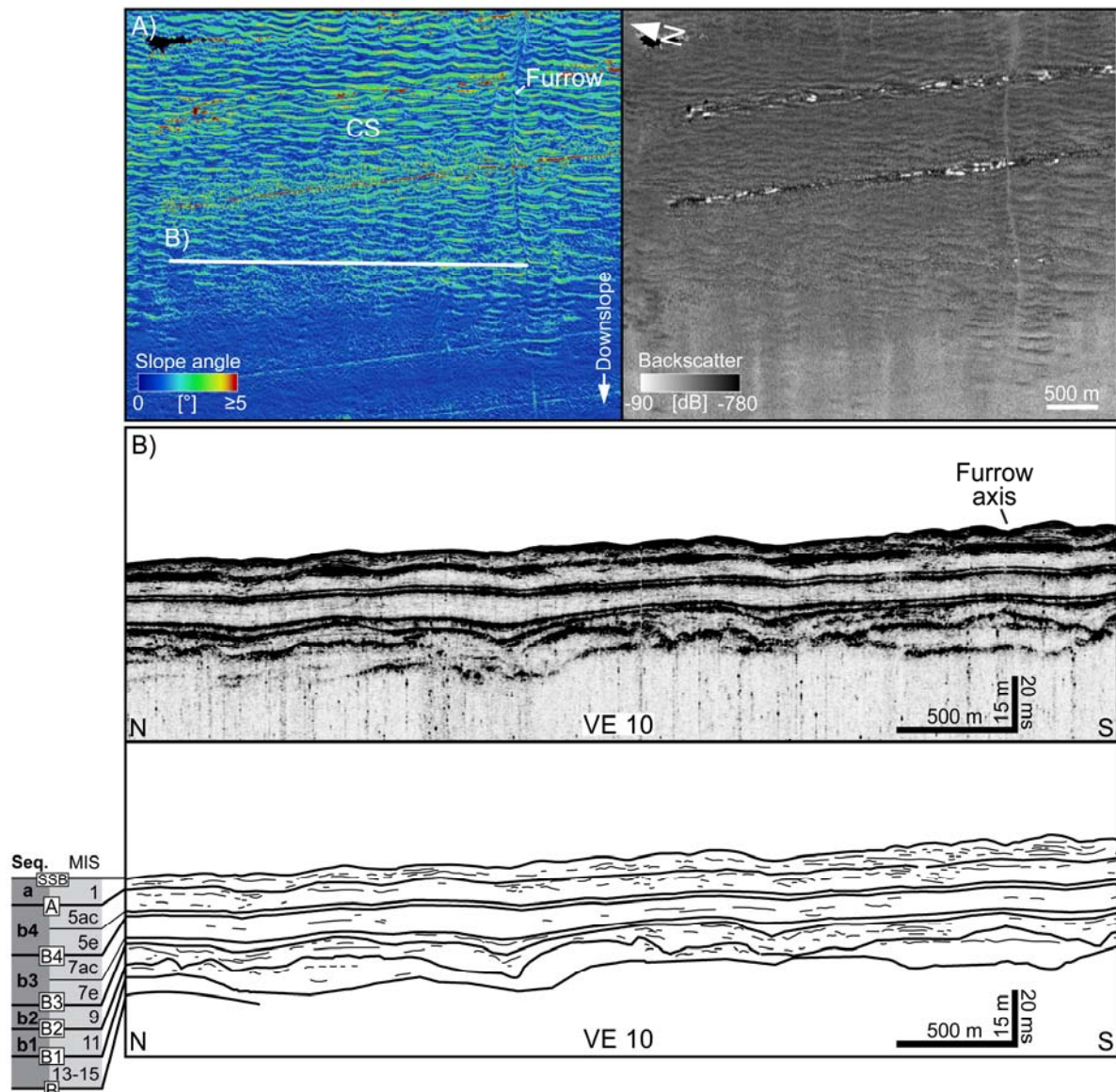


**Fig. 3.11:** A: Slope-angle steepness map and backscatter image of the southern part of the leeward slope, showing a shallow furrow cutting into a field of cyclic steps. White line indicates the position of the subsurface profile in B. B: Across-strike high-resolution subsurface profile from the southern working area (interpretation below). See Figure 3.1C for position.

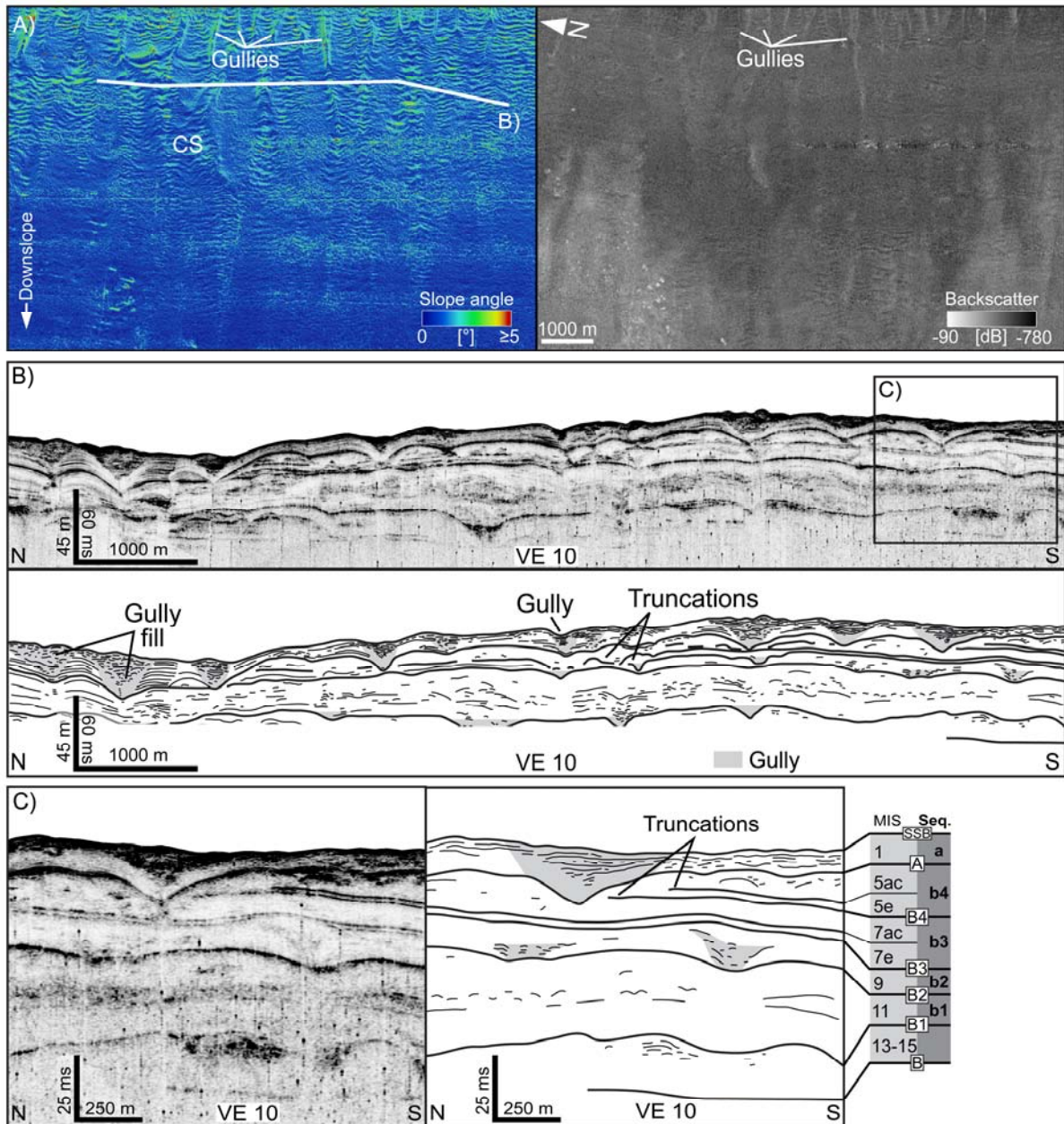


**Fig. 3.12:** A: Slope-angle steepness map and backscatter image of the northern part of the leeward slope, CS=cyclic steps. White lines indicate the positions of the subsurface profile in B. **B:** Across-strike high-resolution subsurface profile (interpretation below) from the northern working area. See Figure 3.1C for position. The slope deposits are dissected by cut-and-fill structures of variable size. **C:** These numerous erosional features result in truncations and a noncoherent reflection pattern.

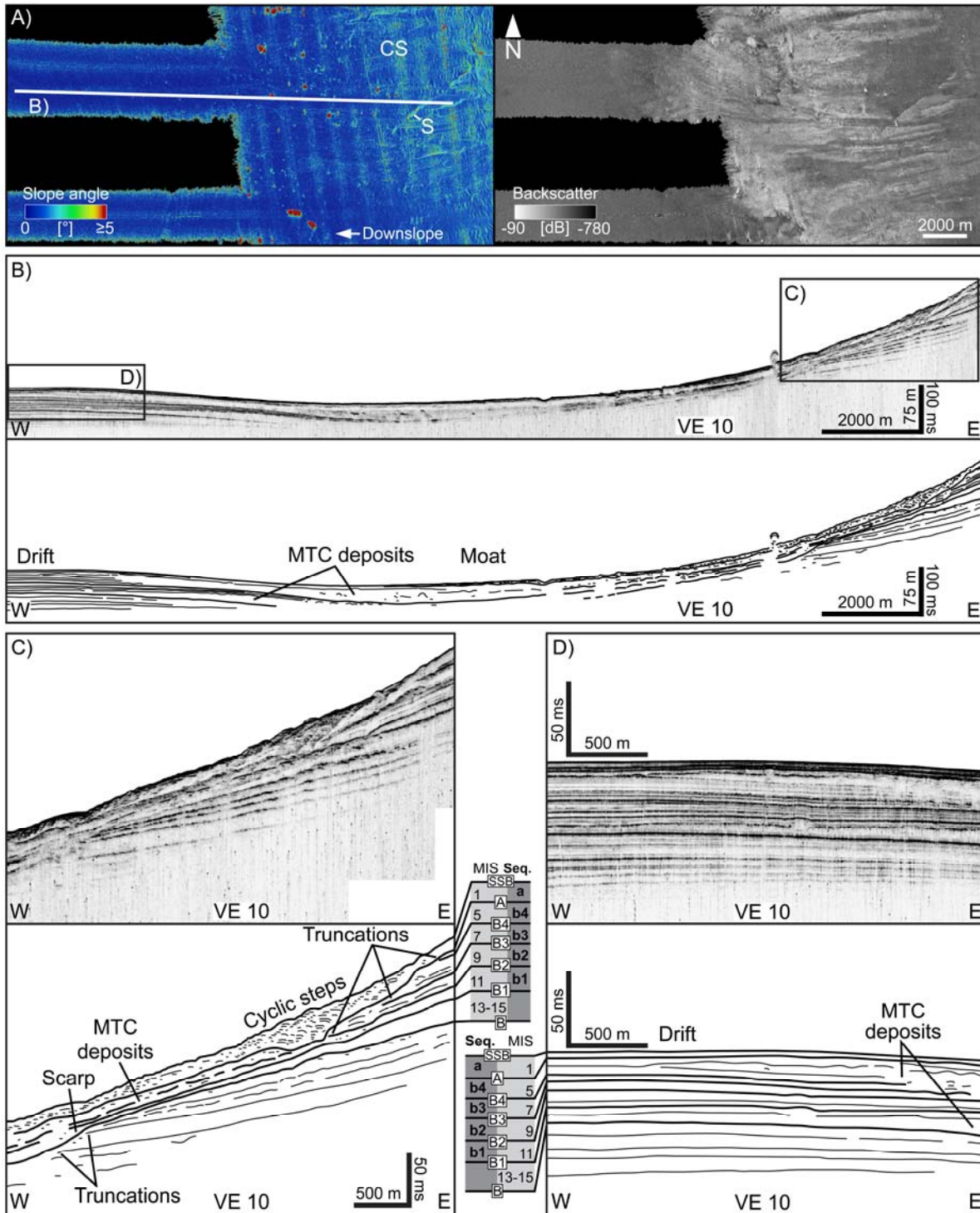


**Fig. 3.13:** **A:** Slope-angle steepness map and backscatter image of the northern part of the leeward slope. White lines indicate the positions of the subsurface profile in B. **B:** Along-slope high-resolution subsurface profile (interpretation below) from the northern working area. See Figure 3.1C for position. **C:** At the lower slope, MTC deposits interfinger with slope deposits. Large buried scarps occur along the slope and truncate several sequence boundaries. **D:** Basinwards, the MTC deposits interfinger with drift deposits.

### **3.5.1.6 Sequence b and a (0.6-0 Ma)**

During the early formation stages of sequence b, about 0.43 Ma ago, large slope failures occurred along the entire leeward slope of GBB. It is proposed that these slope failures were triggered by changes in the amplitude of the sea-level fluctuations that occurred during the Mid-Brunhes event (MBE). The MBE roughly corresponds to the transition between MIS 12 and MIS 11 (Termination V) and marks the onset of a step-like change in the intensity of interglacial, which resulted in increased amplitude of glacial-interglacial cycles (Berger and Wefer, 2003; EPICA, 2004).

The post-MBE slope succession can be subdivided into five individual sedimentary wedges, based on the hydroacoustic data. These wedges represent the sedimentary product of fourth-order sequences (b1 to a), generated by 100 ka glacial-interglacial cycles (Fig. 3.10B; C). Each of these high-frequency sequences can be assigned to a specific MIS (Figs. 3.7B; C). According to Wunsch et al. (2016), individual wedges can be subdivided into two parts based on sediment texture and aragonite content. The lower part represents the initial wedge, which formed right after the onset of platform flooding. Sediments are fine-grained with a higher aragonite content. The upper part of the wedge consists of coarser sediments with lower aragonite content and accumulated after completion of platform flooding (Fig. 3.7B; C). The individual wedges (b1 to a) differ between the northern and southern part of the study area.

#### **3.5.1.6.1 Southern part of the study area**

In the southern part, the lower most sequence (b1) is characterized by leveling of the slope morphology, which was formed by extensive mass wasting processed during the MBE. During the deposition of sequences b2 to a, the exported platform sediments formed individual wedges that all thin out at nearly the same distance from the recent platform margin (Fig. 3.10B; 3.18F). A further westward progradation of these highstand wedges is herein proposed to have been prevented by the north-directed contour currents that winnow the sediments along the toe of slope. Platform-derived sedimentation on the slope is strongly tied to short-term sea-level fluctuations (Droxler and Schlager, 1985; Rendle et al., 2000). On a flat-topped carbonate platform, like the GBB, a sea-level drop of just 10 m can emerge large parts of the platform interrupting the sediment export to the slope (Schlager et al., 1994; Kievman, 1998). During sea-level lowstands, the sedimentation on the slope is reduced with deposition of coarse-grained sediments, partly enriched in lithoclasts (Fig. 3.7C) (Rendle-Buehring and Reijmer, 2005). Such sea-level fluctuations occurred during the MIS substages 7d (sequence b3) and 5e (sequence b4). Due to a lower sea level during the

MIS 7, approximately 18 m below its present position, large parts of the platform top were emerged and carbonate production was restricted to the deeper margin areas (c.f. Manfrino and Ginsburg, 2001; Kievman, 1998). Between 235 and 220 ka BP, during the MIS substage 7d, sea level dropped to about 85 m below its present position. At this time, a partially lithified wacke- to packstone interval formed along the leeward slope of GBB (Fig. 3.7C). After 220 ka BP, during MIS substage 7c, the margin areas were re-flooded and the carbonate production resumed. This interpretation is supported by U/Th dates of core 1008A from depths of 17.49 and 18.84 mbsf that assign the sediments above and below the wacke- to packstone interval to the MIS substages 7c (202 ka BP) and 7e (244 ka BP), respectively (Fig. 3.7C) (Robinson et al., 2002; Henderson et al., 2006). A sea-level oscillation during the substage 5e caused the formation of a mud- to wackestone layer enriched in lithoclasts (Fig. 3.7C). This sea-level oscillation lasted 10 ka, from 130 to 120 ka BP and in the Bahamian region, the sea level dropped from 2.5 m above to 2 m below its present position. Around 120 ka BP (substage 5e), after a period of continuous rise, sea level reached 6 m above its present position (Neumann and Hearty, 1996; Hearty, 1998; Hearty et al., 2007). On the GBB, this was a time of erosion, which dramatically reshaped the morphology of the archipelago (Hearty and Neumann, 2001).

#### **3.5.1.6.2 Northern part of the study area**

In the northern part of the working area, the sedimentary record of the individual sequences (b1 to a) appears incomplete. This is caused by the interplay of depositional and erosional processes (Wunsch et al., 2016). Erosion primarily took place during lowerings of sea level. Slope failures eroded large volumes of sediments deposited during the previous sea-level highstand and the displaced debris were deposited as MTC at the toe of slope (Figs. 3.13B; 3.18F). These slope failures formed large depressions, which are upslope bordered by head scarps, which created the initial base of gullies (Fig. 3.12B). During the subsequent sea-level rise and highstand, the sediments exported from the platform were funneled by these gullies. These funneled sediments subsequently filled the depressions beneath the scarps (Figs. 3.13B; C; 3.18F). This alternating pattern of deposition and mass wasting formed a complex slope morphology of gullies and scarps, which also characterizes the recent sea floor (Figs 3.12A; 3.13A).

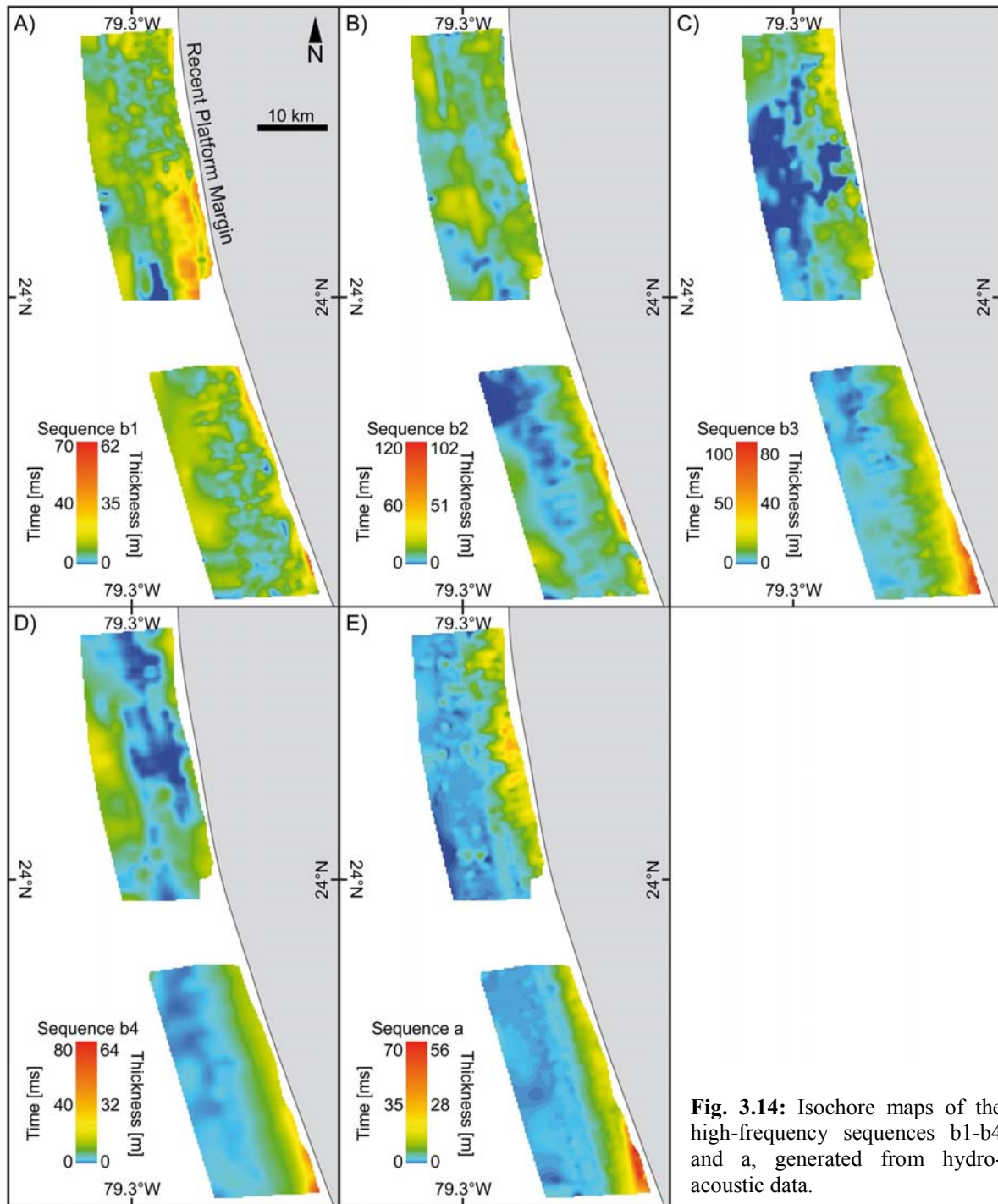


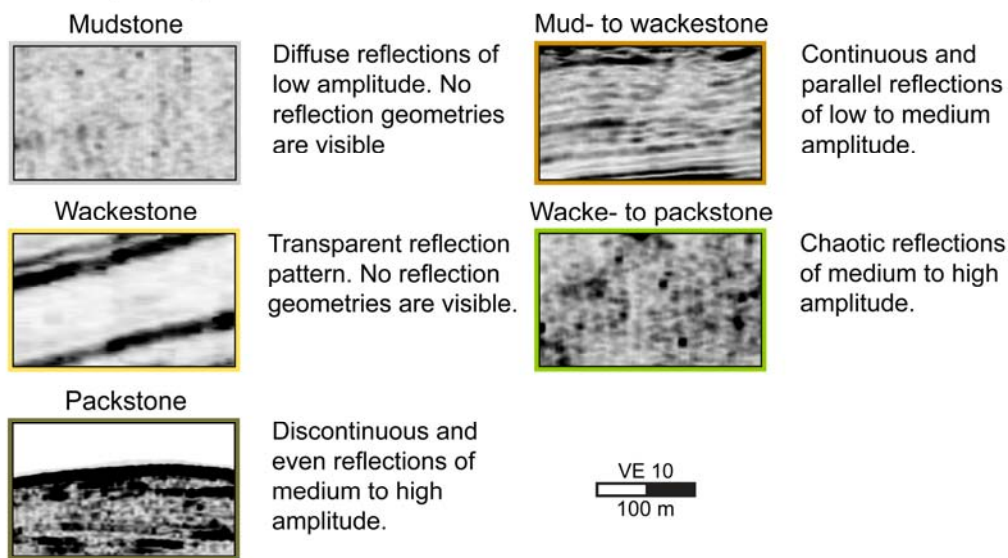
**Fig. 3.14:** Isochore maps of the high-frequency sequences b1-b4 and a, generated from hydro-acoustic data.

### 3.5.1.6.3 Development of the recent platform margin

Since the Middle Pleistocene (sequences b1), the platform margin shows a continuous steepening, which resulted in a 150-m high recent submarine cliff (Fig. 3.9A). Eberli (2000) related this steepening to the increased amplitudes in the sea-level fluctuations after the MBE. It is proposed that the steepening of the margin changed the predominant mode of off-bank transport from normal off-bank currents to density cascading. Density cascading events are hyperpycnal off-bank flows triggered by the increased density of inner bank

waters. Density cascading is responsible for the gross of the modern off-bank transport (Wilson and Roberts, 1992; 1995). As a result of this change in the off-bank sediment transport, two features developed that are prominent on the recent slope. The first a margin-parallel depression, which is bordered basinwards by a sediment ridge (Fig. 3.9B); the second are the cyclic steps that occupy the complete middle slope (Betzler et al., 2014; Wunsch et al., 2016) (Figs. 3.10A; 3.11A; 3.18F). The margin-parallel depression represents an erosional trough, similar to a plunge pool (Wilber et al., 1990). This plunge pool was carved into the slope by the hyperpycnal flows of the density cascading, which can reach a maximum down-slope velocity of 2.47 m/s (Wilber et al., 1993). Since its initial formation, the position of the plunge pool is relatively stable (Fig. 3.9B). The cyclic steps formed near a slope break which has been proposed to trigger a hydraulic jump in the supercritical flows of the density cascading (Fig 3.10A) (Betzler et al., 2014).

**Seismic packages:**



**Seismic surfaces:**

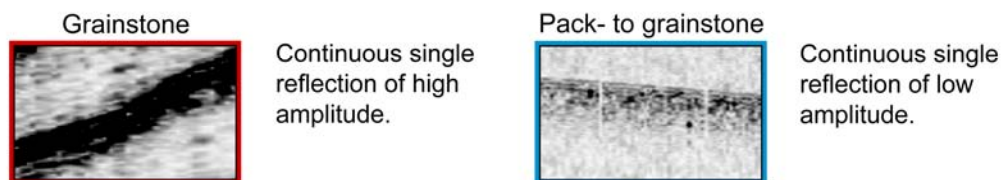


**Fig. 3.15:** Seismic facies generated from the correlation of sedimentological core data and the high-resolution subsurface data. The seismic facies are subdivided into seismic packages and seismic surfaces. See text for discussion.

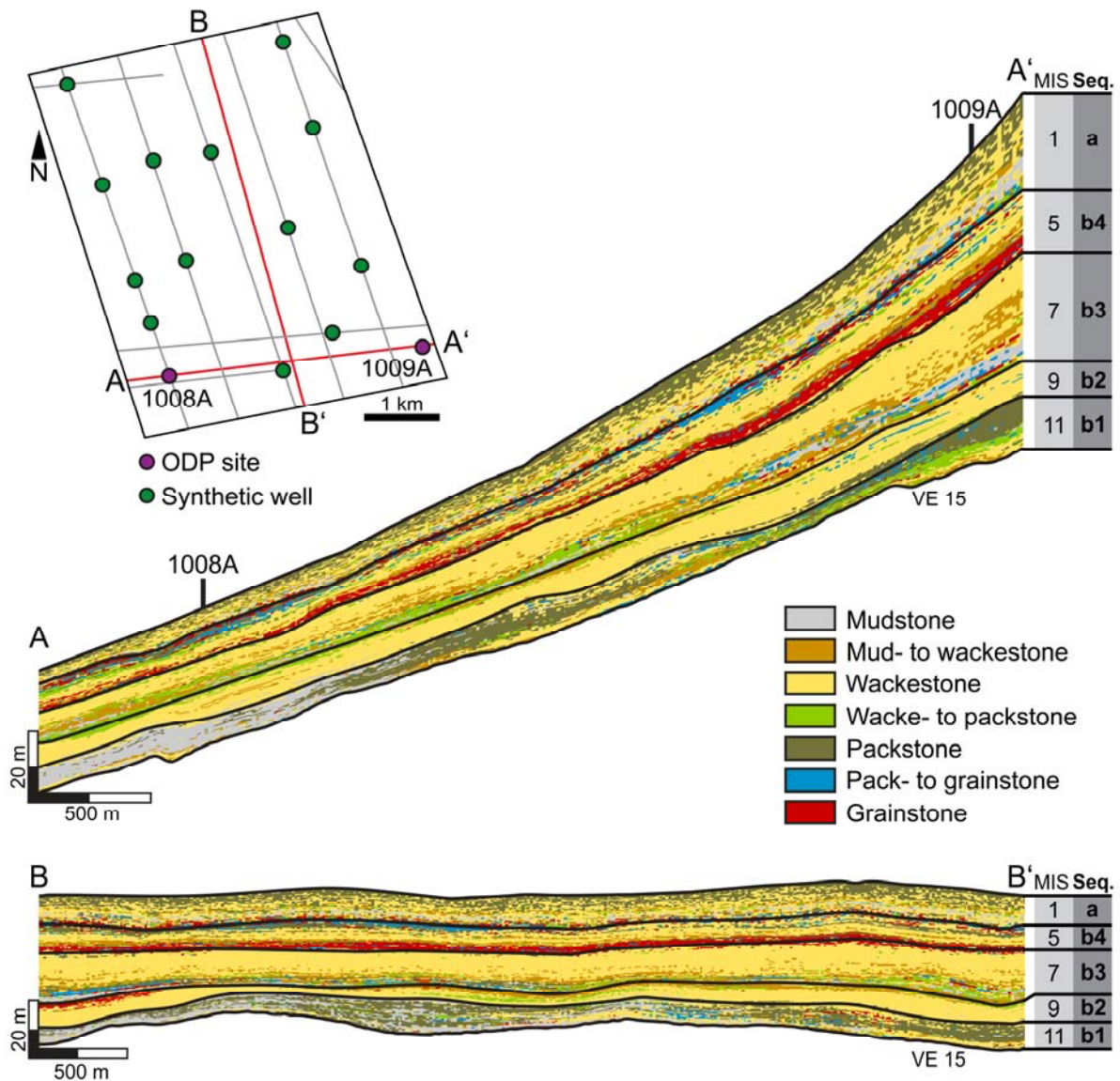


**Fig. 3.16:** Stochastic facies model for the southern study area (see location in Fig. 3.1C). The model shows the facies heterogeneities along-slope and across strike of the slope within the succession of the sequences b1-b4 and a. MIS= Marine Isotope Stage.

### 3.5.2 Facies distribution and heterogeneities along the leeward slope

The current influence on the GBB slope strengthens from south to north. This results in contrasting facies-distribution patterns. Currents as a driver of facies variability adds a further mechanism to the established models of carbonate slope deposition (Schlager and Ginsburg, 1981; Playton, 2010), where the slopes is fed by line sources, the sediment fines with increasing distance from the platform margin, and lateral facies changes are caused by differences in source-sediment grain sizes and textures. The encountered facies heterogeneities along the strike of a carbonate slope make the development depositional models challenging. An improved understanding of such facies heterogeneities is also important in reservoir modelling, because facies alternations at small scales lead to

significant changes in the spatial petrophysical properties, such as porosity and permeability (Lucia, 1995).

In the south of the GBB slope, the impact of the currents on the sediment distribution is weak and the exported fine-grained platform sediments such as wackestone form the highstand wedge as part of the periplatform drift. During sea-level lowstands, the coarser-grained sediments form condensed lowstand intervals. This along-strike layer-cake stratigraphy fits well into simplified reservoir models, which predict the same facies and petrophysical properties at the same stratigraphic level (Borgomano et al., 2008; Alnazghah et al., 2013) (Fig. 3.16).

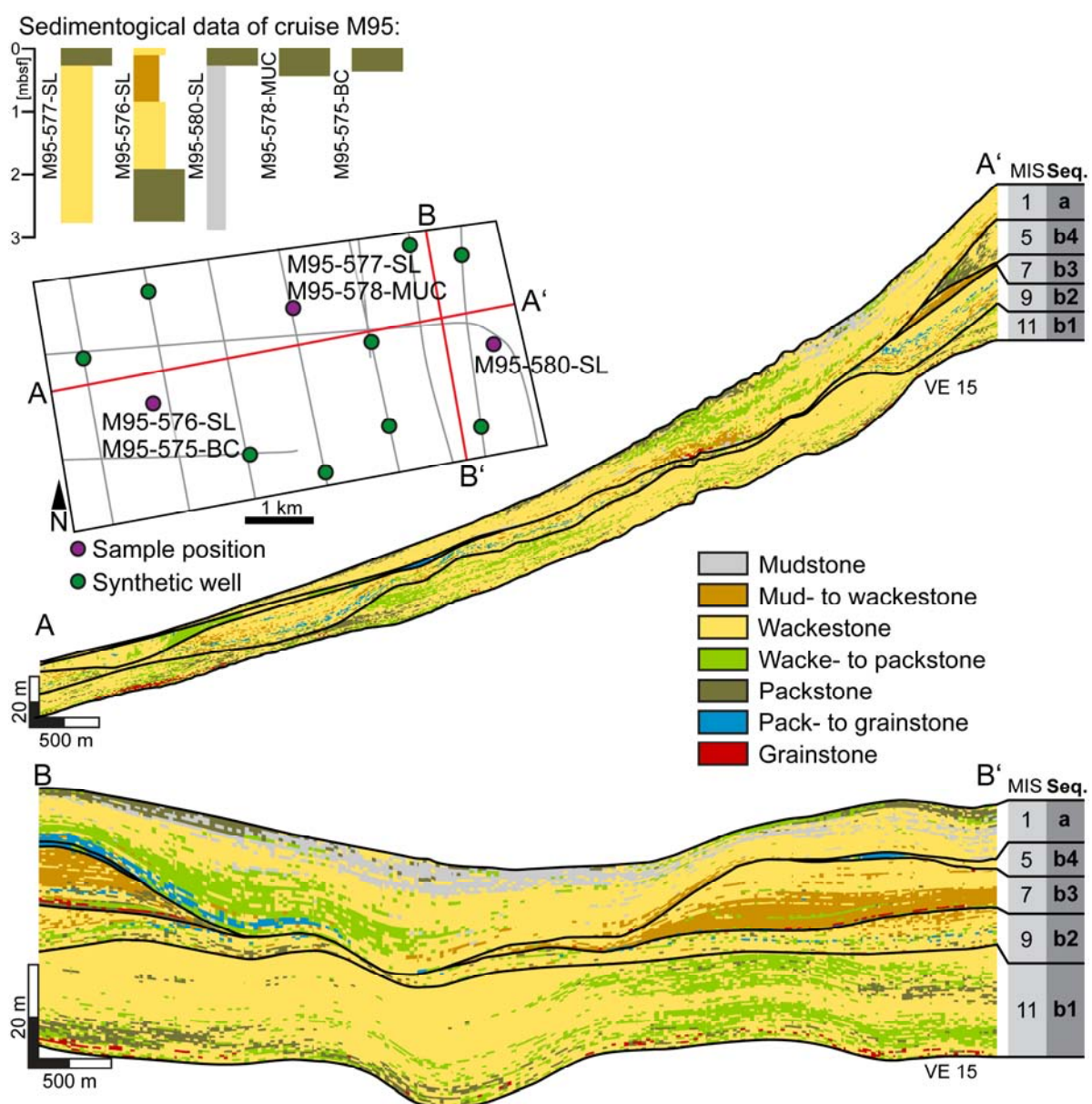


**Fig. 3.17:** Stochastic facies model for the northern study area (see location in Fig. 3.1C). The model shows the facies heterogeneities along-slope and across strike of the slope within the succession of the sequences b1-b4 and a. MIS= Marine Isotope Stage.

In the northern part of the slope, where the current impact is strong, formation and filling of large depressions induces facies heterogeneities at an interwell-scale (Fig. 3.17). During sea-level lowering, extensive erosion formed isolated sedimentary bodies of the same facies, bounded by unconformities and separated by large depressions (Fig. 3.17). Platform-derived sediments fill these depressions, during the subsequent sea-level rise and highstand (Fig. 3.17). This alternation of deposition and erosion forms a complex facies distribution. The infill is not homogenous and coarsens towards the flanks as the result of sea-floor winnowing by bottom currents (Betzler et al., 2014). The encountered facies heterogeneities are beyond the resolution of reflection seismic data and make a reservoir characterization complicated.

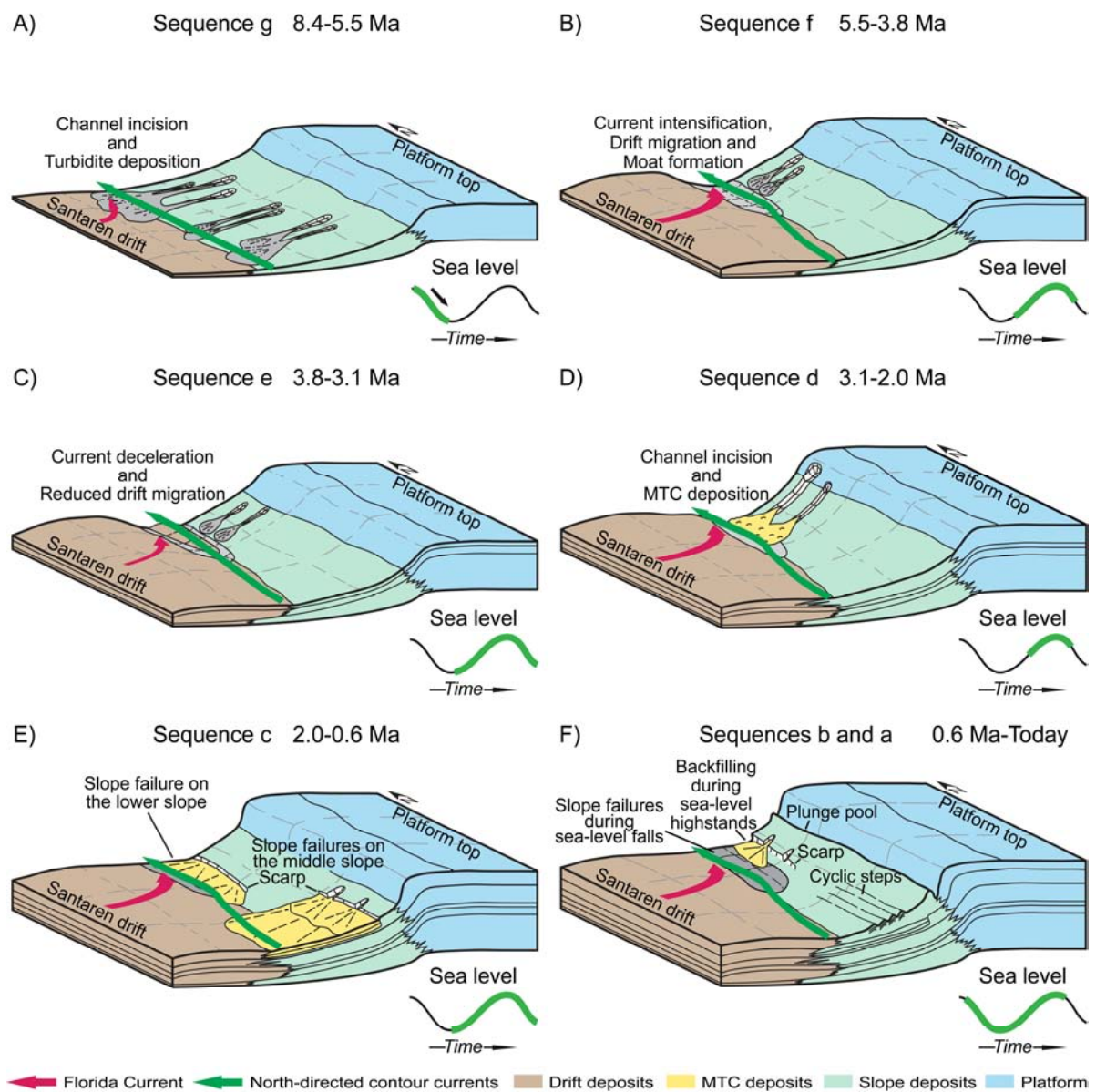


**Fig. 3.18:** Depositional model for the evolution of the leeward slope of Great Bahama Bank; see discussion for details.

### 3.5.3 The role of contour currents on the slope sedimentation along the leeward slope

Various authors have recognized an influence of the currents on the leeward slope of GBB (Schlager and Ginsburg, 1981; Ball et al., 1987; Anselmetti et al., 2000; Rendle and Reijmer, 2002; Rendle-Buehring and Reijmer, 2005; Bergman, 2005; Betzler et al., 2014; Wunsch et al., 2016; Principaud et al., 2016). The herein presented data document an increasing influence of the current regime on the sedimentation and the slope architecture towards the north of the study area. In the southern part, where only the north-directed currents acts on the slope, the current influence is low and restricted to the toe of slope. At the toe of slope the contour current winnows the sediments and probably prevents the leeward slope from further westward progradation. Toward the north, the current impact gradually increases with the coalescence of north-directed contour currents and the Florida Current. Current winnowing and drift migration formed a large moat. Continuous winnowing triggered the incision of channels and the accumulation of large mass transport complexes. In this context, it can be speculated if continuous winnowing also favors the large slope failures that occurred during the middle and upper Pleistocene (sequences b1 to b4).

The current control on the slope must be even higher north of the study area, where the Florida Current bends towards the north along the slope of GBB (Fig. 3.1A). The present position and shape of this slope segment reveal the role of the currents in inhibiting slope progradation (Ball et al., 1987). Large parts of the lower slope are winnowed and show no Holocene sediment cover (Principaud, 2015). In this area, the basinal drift sedimentation was initiated during the Miocene and evolved throughout successive phases of growth and lateral migration (Principaud et al., 2016). During the Late Pliocene and Pleistocene, large slope failures displaced slope material as mass-transport complexes into the basin (Principaud et al. 2015; 2016). These large slope failures occurred simultaneously with the accumulation of MTC deposits along the toe of slope, described in this thesis. Regarding the higher current impact on the slope, oversteepening of the toe of slope by current winnowing is therefore proposed as a potential trigger mechanism for slope failures along this part of the leeward slope.

## **The Holocene slope succession of Great Bahama Bank; slope sedimentation in response to platform bathymetry and sediment producers**

### **4.1 Outline of the chapter**

In contrast to the previous chapters II and III, which described the sedimentary processes and the resulting slope features, chapter IV focuses on the sedimentary wedge along the leeward slope of Great Bahama Bank (GBB) that deposited since the last glacial maximum. The interpretation of hydroacoustic data in chapter II and III shows that this wedge can be subdivided into two parts. This subdivision was previously interpreted as the result of an increased off-bank transport (Betzler et al., 2014). This chapter provides an analysis of two gravity cores, which indicate a compositional change in the exported platform sediments during the postglacial sea-level rise. This compositional change is caused by the unique platform bathymetry of GBB and the different sediment producers, which established on the platform top during different stages of re-flooding.

### **4.2 Platform morphology and environmental settings**

The Bahamian archipelago is composed of several carbonate platforms, which are exposed to a wind regime dominated by the easterly trade winds (Sealey, 1994). The largest carbonate platform of the archipelago is the GBB (Fig. 4.1A). On the platform top of the GBB, the trade-wind induced surface currents are responsible for sediment distribution and the prevailing off-bank transport to the western leeward side of the platform (Hine and Steinmetz, 1984). The bathymetry of GBB is non-planar and islands are located mainly on its windward, eastern margin. The water depth of the platform interior varies between 0 m in the intertidal areas of the islands and 15 m in the deepest parts (Boss and Rasmussen, 1995; Harris et al., 2015). The leeward margin smoothly inclines towards the west and is nowadays situated at water depths between 15 and 60 m, with the platform edge at 60 m (Fig. 4.1B; Freile et al., 1995; Eberli, 2013; Harris et al., 2014; Jo et al., 2015). The uppermost part of the leeward slope, from 60 m to 160 m water depth is formed by a steep escarpment that is lined at its base by a margin-parallel plunge pool, bordered basinward by a ridge (Wilber et al., 1990; Betzler et al., 2014; Jo et al., 2015; Wunsch et al., 2016).

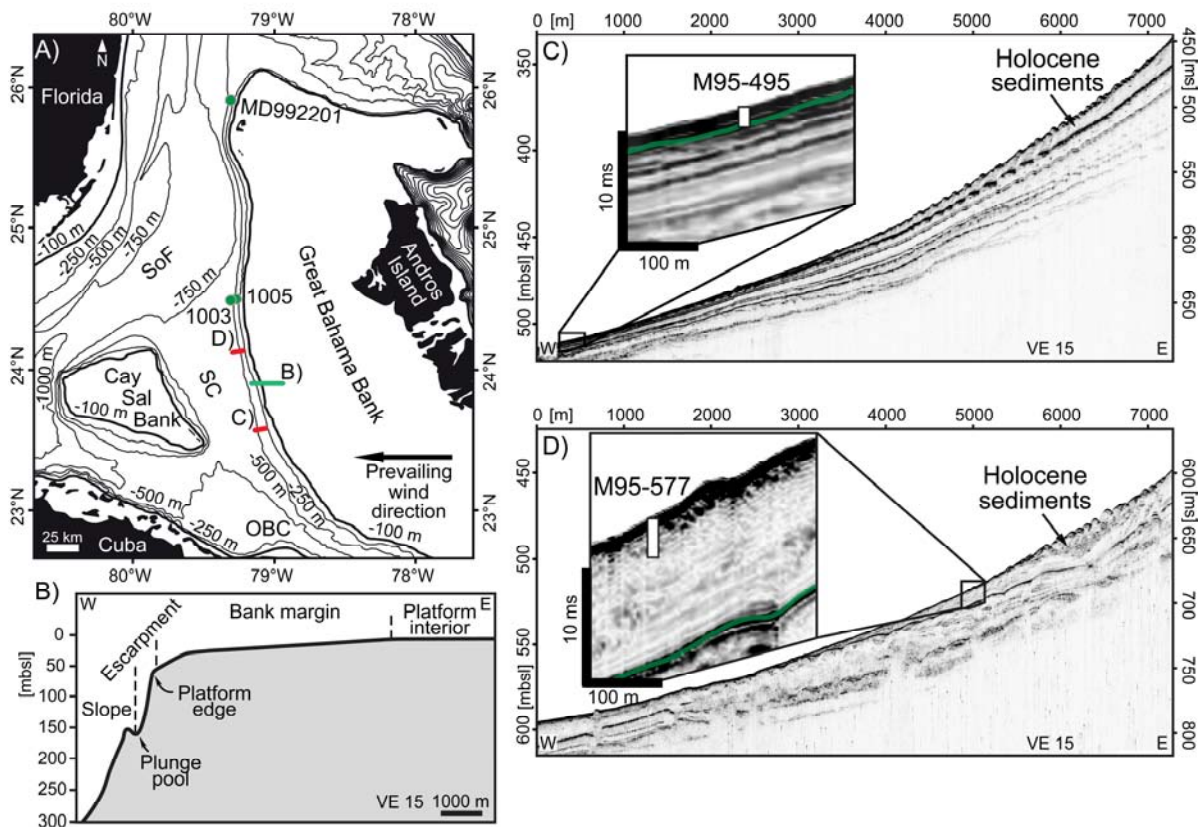


**Fig. 4.1:** **A:** Location map of the study area. The Santaren Channel (SC) connects the Straits of Florida (SoF) with the Old Bahama Channel (OBC). Green dots mark position of core sites. Red lines indicate the position of the subsurface profiles shown in C and D. Green line shows approximated position of the idealized profile in B. **B:** Idealized profile of the leeward platform margin, generated from bathymetrical data after Newell and Imbrie (1955); Wilber et al. (1990); Freile et al. (1995); Jo et al., 2015); Harris et al. (2014; 2015). **C:** Subsurface profile from the southern part of the leeward slope. The position of gravity core M95-495 is indicated in the inset. The green line indicates SSB S. **D:** Subsurface profile of the northern part of the leeward slope. The position of gravity core M95-577 is indicated in the inset. The green line indicate SSB S.

### 4.3 Data and methods

Subsurface profiles were recorded during R/V Meteor cruise M95 with a parametric sediment echosounder (PARASOUND P70; Atlas Elektronik, Bremen, Germany). The system was operated with two frequencies (18 kHz and 22 kHz). The software PS32segy (Hanno Keil, University of Bremen, Germany) was used to cut and convert the data. Data processing comprised automatic gain control and along-profile amplitude normalization using the software package ReflexW (Sandmeier Software, Karlsruhe, Germany).

Both sediment cores (M95-495, -577) were acquired with a gravity corer (6 m pipe). The cores were cut into one-meter segments and split into half. Sediment texture, -structures and -composition were described onboard, together with measurements of the sediment lightness ( $L^*$ ) with a handheld Minolta (CM-525i) spectrophotometer. Cores were sampled

equidistantly (1.5 cm<sup>3</sup> each 1 cm) for bulk grain-size analysis. Grain-size measurements were performed with a Helos KFMagic laser particle size analyzer (measuring range 0.5/18 to 3500 µm). Grain-size statistics are based on the graphical method after Folk and Ward (1957) and were calculated using the software GRADISTAT (Blott and Pye, 2001). Thin sections were analyzed to describe and quantify the sediment composition. The following components were differentiated: peloids, matrix, foraminifera (benthic and planktonic), lithoclasts, pteropods, bivalves/gastropods, and echinoderma. The sediment texture was classified after Dunham (1962). Smear slides were analyzed to identify the composition of the mud fraction (< 63 µm).

Radiocarbon dating was performed by Beta Analytics Inc. (Miami, FL, USA) on three samples composed of mixed planktonic foraminifera (*Globigerinoides ruber*; *Globigerinoides sacculifer*). Conventional radiocarbon ages were calibrated using CALIB (version 7.0.4; Stuiver and Reimer, 1993) and the calibration curve Marine13 (Reimer et al., 2013) with no correction for local reservoir effects. Ages are rounded to the nearest decade and are reported as maximum of the probability distribution with 2-sigma error range.

Scanning X-ray fluorescence element analysis (XRF) was carried out at the Alfred Wegner Institut (AWI), Bremerhaven, using an Avaatech XRF core scanner at 1 cm scanning intervals and generator settings of 30 kV (1.0 mA) and 10 kV (0.2 mA). All measured values are given in counts per second (cps). Scanning of core M95-495 was possible only in parts because of an uneven sediment surface.

## **4.4 Results**

### **4.4.1 Core sites**

Core site M95-495 is located at the toe of slope (23°36.432' N, 79°07.209' W) at a water depth of 500 m (Fig. 4.1C). Core site M95-577 (24°08.712' N, 79°14.022' W) is located in a filled depression at 514 m water depth (Fig. 4.1D). Subsurface data along the slope of GBB show a series of high-amplitude reflections separating acoustically transparent intervals. The uppermost of these transparent intervals is the Holocene sediment succession (Wunsch et al., 2016). Correlation of hydroacoustic data with ODP Leg 166 core data shows that the high-amplitude reflection at the base of the Holocene corresponds with a cemented interval, the high-frequency seismic sequence boundary S (SSB S), which formed during the last sea-level lowstand (Eberli et al., 1997; Betzler et al. 2014).

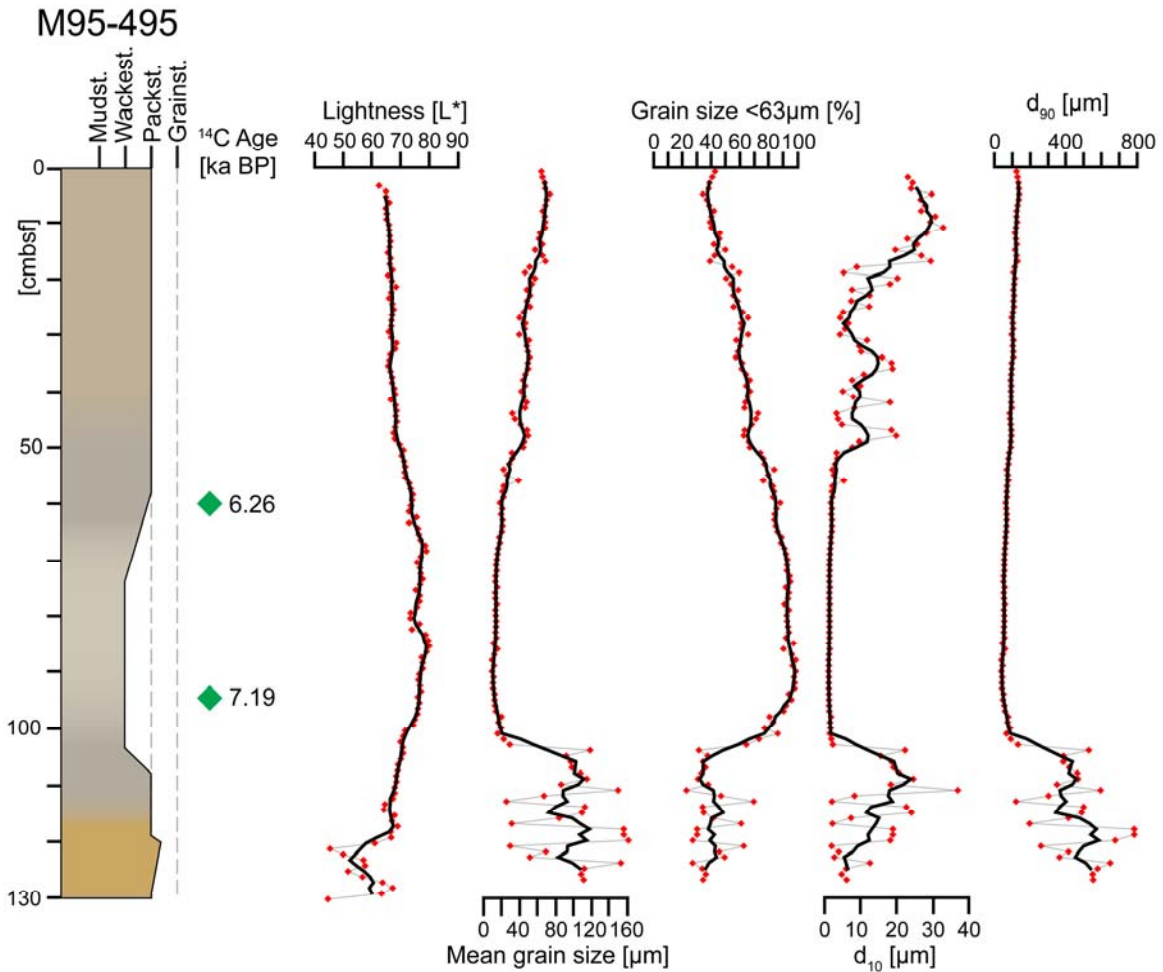


**Fig. 4.2:** Lithological column of core M95-495 with variations in the optical lightness ( $L^*$ ), Mean grain size, the percentage of grains smaller  $63 \mu\text{m}$ , and the  $d_{10}$  and  $d_{90}$  percentiles. Bold black lines indicate 5-point running average. Green rectangles indicate the position of samples used for radiocarbon dating.

Depth (cmbsf)	M95-495					M95-577			
	25	50	80	110	120	50	100	150	220
Peloids	50	40	20	15	15	45	45	35	30
Matrix	30	40	60	60	48	20	25	30	40
Foraminifera	10	15	9	10	5	13	10	12	15
Lithoclasts	5	0	0	10	10	0	0	0	0
Pteropoda	5	5	5	5	5	10	10	18	10
Bivalves and Gastropoda	0	0	5	0	15	10	5	5	0
Echinoiderma	0	0	1	0	2	2	5	0	5

**Table 4.1:** Summary of thin section analyses. The abundance of the components is given in %.

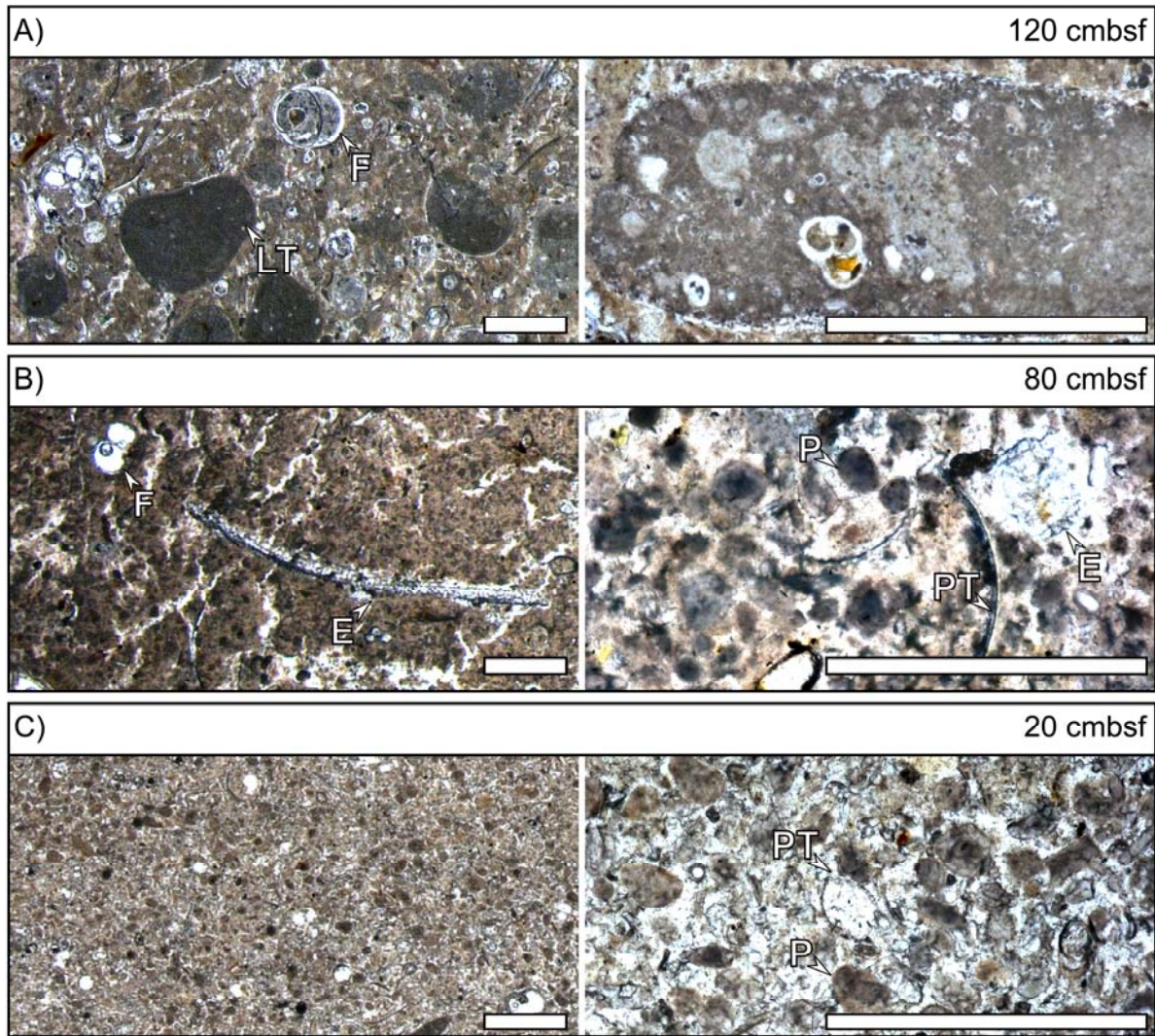


**Fig. 4.3:** **A:** Thin section photographs from a depth of 120 cmbsf (centimeters below sea floor). The sediments have a packstone texture, and containing blackened lithoclasts (LT) and foraminifera (F) filled with dark micrite. These lithoclasts incorporates foraminifera remain and smaller lithoclasts. **B:** Thin sections from a core depth of 80 cmbsf. The sediments have a wackestone texture and are characterized by high matrix content. Components are peloids (P) foraminifera (F), echinoderm (E) and Pteropoda (PT) fragments. **C:** The sediments from a depth of 20 cmbsf have a packstone texture. The main components are peloids. Scale bar = 500  $\mu\text{m}$ .

#### 4.4.2 Core M95-495

The lowermost part of core M95-495, from 130 cmbsf to 105 cmbsf (centimeters below sea floor), consists of lithified sediments with a pack- to grainstone texture, overlain by unlithified sediments with a packstone texture (Fig. 4.2). The optical lightness ( $L^*$ ) values of the lithified pack- to grainstone shows no trend and varies between 40 and 70, but increases gradually in the overlying packstone. The mean grain size and the percentage of grains  $< 63 \mu\text{m}$  show no trend. The  $d_{10}$  shows a constant upcore-coarsening, while the  $d_{90}$  shows a fining. The analysis of thin sections shows that the sediments contain foraminifera filled with dark-stained micrite and large blackened lithoclasts (Fig. 4.3A; Tab. 4.1).

The overlying interval (105-50 cmbsf) consists of gray sediments with a wackestone texture. The sediment is mainly composed of peloids, foraminifera, pteropod remains and a high percentage of matrix (Fig. 4.3B; Tab. 4.1). Optical lightness peaks at 85 cmbsf ( $L^*$  80) and decrease upcore ( $L^*$  around 75). The mean grain size drops to its minimum (10  $\mu\text{m}$ ) at 88 cmbsf; above 70 cmbsf there is a coarsening-upward trend (Fig. 4.2). Both, the curves for  $d_{10}$  and  $d_{90}$ , show a plateau at 2  $\mu\text{m}$  and 50  $\mu\text{m}$ , respectively.

The uppermost interval of the core (50-0 cmbsf) consists of brownish sediments with a packstone texture and shows decreasing  $L^*$ -values towards the sea floor (Fig. 4.2). The packstone interval shows an increasing percentage of peloids and decreasing matrix content towards the top of the core, compared to the subjacent wackestone (Fig. 4.3C; Tab. 4.1). Smear slides show that the matrix of the wackestone interval consists of aragonite needles (< 10  $\mu\text{m}$ ), coccoliths and very small bioclasts. Upcore, in the packstone interval, the fraction < 63  $\mu\text{m}$  is composed of small peloids, peloid fragments and bioclasts, whereas aragonite needles are rare. Samples from 60 cm and 95 cmbsf yielded radiocarbon ages of 6.26 ka cal BP and 7.19 ka cal BP, respectively (Fig. 4.2; Tab. 4.2).

#### 4.4.3 Core M95-577

The lowermost interval (265-100 cmbsf) of core M95-577 consists of unlithified sediments with a mud- to wackestone texture. There is a coarsening-upward trend accompanied by a decrease in optical lightness (Fig. 4.4). The coarsening is also reflected in a gradually decreasing percentage of grains smaller 63  $\mu\text{m}$  (Fig. 4.4; 90% at 265 cmbsf to 79% at 100 cmbsf). The  $d_{10}$  slightly declines upcore, while the  $d_{90}$  increases from 60  $\mu\text{m}$  (at 265 cmbsf) to 82  $\mu\text{m}$  (at 100 cmbsf). According to Rothwell et al (2006) is the strontium-calcium ration (Sr/Ca) a proxy for the aragonite content of carbonates of shallow-water origin. The Sr/Ca ratio gradually decreases upcore, from 0.205 cps at 265 cmbsf to 0.181 cps at 100 cmbsf. Sediments are composed of peloids, foraminifera and pteropods (Fig. 4.5A; Tab. 4.1).

The interval between 100 and 25 cmbsf consists of gray to light gray sediments with a packstone texture (Fig. 4.4). The sediment is composed of peloids, foraminifera and pteropoda remains with 20 to 25% of matrix (Fig. 4.5B; Tab. 4.1). The mean grain size slightly decreases, accompanied by an increasing portion of grains smaller 63  $\mu\text{m}$ . The  $d_{10}$  decreases from 2 to 1.5  $\mu\text{m}$  and the  $d_{90}$  increases and reaches its maximum of 98  $\mu\text{m}$  at 85 cmbsf. The Sr/Ca ratio increases (0.22 cps at 70 cmbsf).

Above 25 cmbsf the sediments have a packstone texture and decreased  $L^*$ -values. This change in the texture is reflected in the mean grain size, which shows a sharp increase

upcore of 25 cmbsf; the percentage of grains  $< 63 \mu\text{m}$  remains constant (about 72%); both,  $d_{10}$  and  $d_{90}$ , increases upcore, with maxima at the sea floor. A sample from 260 cmbsf yielded a radiocarbon age of 3.94 ka cal BP (Tab. 4.2).

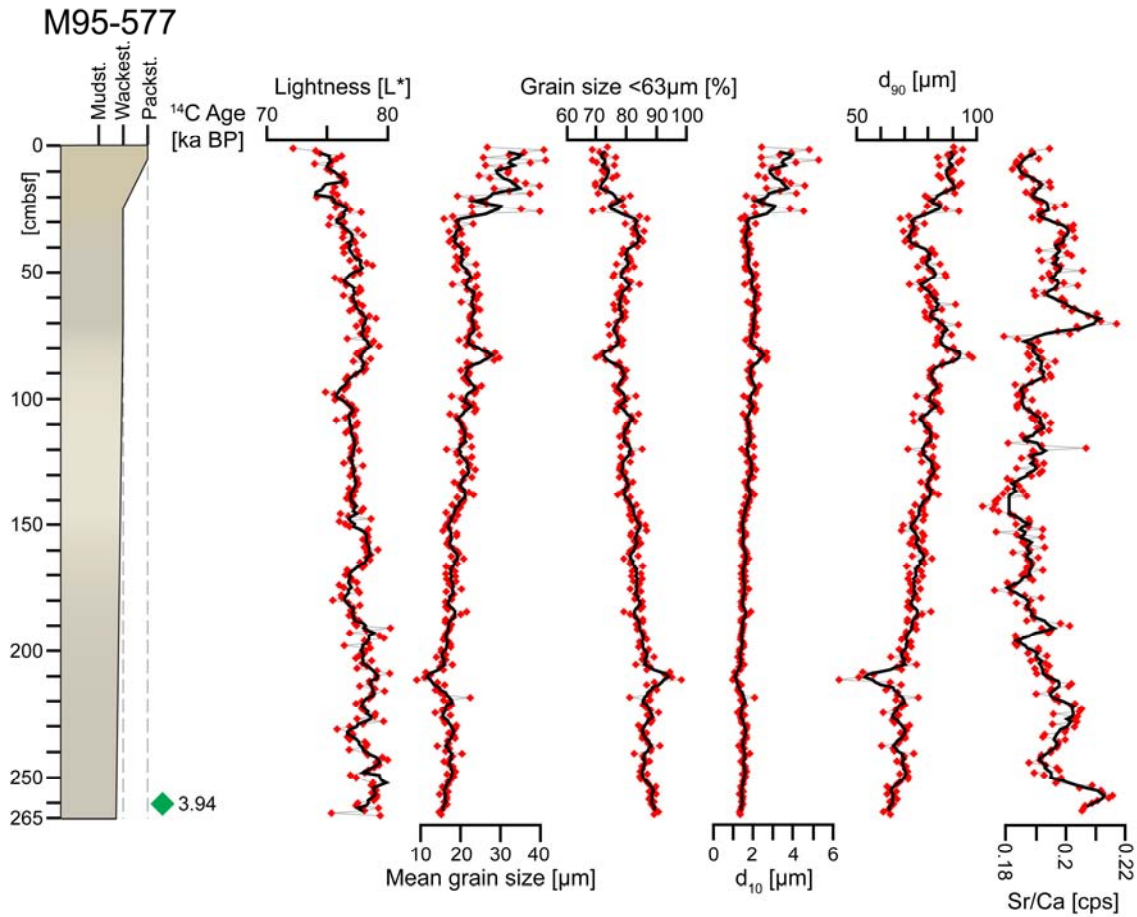


**Fig. 4.4:** Lithological column of core M95-577 with variations in the optical lightness ( $L^*$ ), Mean grain size, the percentage of grains smaller  $63 \mu\text{m}$ , the  $d_{10}$  and  $d_{90}$  percentiles, and Strontium (Sr) ratio given in relation to the calcium (Ca) counts of the XRF core scans. Bold black lines indicate 5-point running average. Green rectangle indicates the position of the sample used for radiocarbon dating.

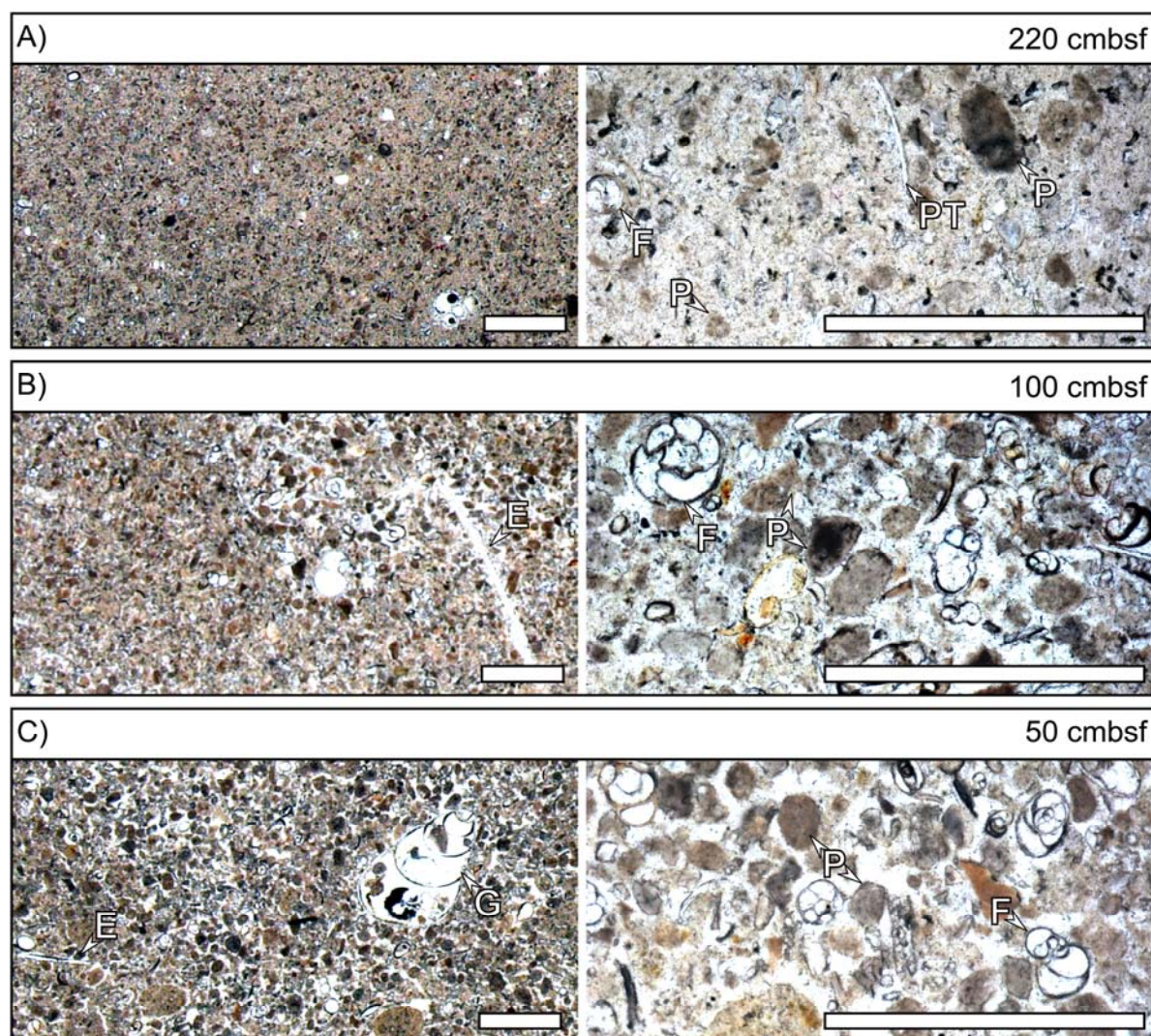


**Fig. 4.5:** **A:** Thin section photographs from a depth of 220 cmbsf (centimeters below sea floor). The sediments have a mud- to wackestone texture, and consisting of foraminifera (F), Peloids (P) and pterophoda fragments (PT). **B:** Thin section photograph from a core depth of 100 cmbsf. The sediments have a wackestone texture. The components are peloids (P) foraminifera (F) and echinoderm (E) fragments. **C:** The sediments from a depth of 50 cmbsf have a wackestone texture. The main components are peloids (P), foraminifera (F), echinoderm fragments (E) and gastropod shells (G). Scale bar = 500  $\mu\text{m}$ .

Core	Depth (cmbsf)	Lab ID	Material	$^{14}\text{C}$ age (yrs BP)	$^{13}\text{C}/^{12}\text{C}$ ratio (‰)	Calibrated age ( $\Delta R=0$ ) cal BP (2 $\sigma$ ranges, 95.4% prob.)	
						Range (yrs)	Median (ka)
M95-495	60	Beta-436327	Plank. Foraminifera	5410 $\pm$ 30	+1.5	6180 - 6320	6.26 $\pm$ 0.07
M95-495	95	Beta-436328	Plank. Foraminifera	6210 $\pm$ 30	+2.0	7115 - 7265	7.19 $\pm$ 0.075
M95-577	255	Beta-464460	Plank. Foraminifera	3950 $\pm$ 30	+2.3	3840 - 4040	3.94 $\pm$ 0.1

**Table 4.2:** Results of radiocarbon dating. Calibration was performed using Calib (v7.0.4, Stuiver & Reimer, 1993) and the calibration curve Marine13 (Reimer et al., 2013). No local reservoir correction was applied.

## **4.5 Interpretation and discussion**

### **4.5.1 Depositional geometry**

The two hydroacoustic profiles show that the distribution of Holocene sediments is not constant along strike of the leeward slope (Fig. 4.1C; D). In the southern part of the slope, where M95-495 is located, the Holocene sediments form a wedge that thins out approximately seven kilometers from the platform margin (Fig. 4.1C) (Wunsch et al., 2016). The radiocarbon dates indicate that the upper 95 cm of core M95-495 record the sedimentary history of the last 7 ka (Fig. 4.6). Towards the north, where M95-577 is located, large slope failures occurred during the sea level lowering after the last interglacial (Wunsch et al., 2016). These slope failures formed large depressions and gullies. During the subsequent highstand, the exported sediments were funneled by the gullies and bypassed to the depressions. This leveling of the slope morphology results in a thicker Holocene succession within the depressions compared to the surrounding slope areas (Fig. 4.1D) (Wunsch et al., 2016). Core M95-577 was recovered from such a filled depression and the radiocarbon dates show that the 3 m thick succession comprises sediments deposited during the last 4 ka (Fig. 4.7).

### **4.5.2 Glacial/transgressional stage (sea level position: -125 m to -60 m)**

The flooding history of GBB is subdivided into three stages based on lithological changes described herein (Fig. 4.8). The first is the glacial/transgressional stage, which comprises the last glacial maximum (LGM) and the subsequent sea-level rise until the flooding of the platform edge. The platform top was emerged during the LGM, according to sea-level reconstructions for the LGM and the subsequent sea-level rise (Fleming et al., 1998; Toscano and Macintyre, 2003). On the platform top, subaerial exposure led to karstification and soil formation (Carew and Mylroie, 1995; Kievman, 1998; Manfrino and Ginsburg, 2001). On the western, the leeward slope of GBB, the sediment supply was restricted to pelagic input (Eberli et al., 1997). This limited supply enabled the formation of hardgrounds (Malone et al., 2001; Eberli et al., 2002). In core M95-495 LGM sedimentation is represented by a lithified pack- to grainstone interval that correlates with a lithified grainstone layer in the succession of ODP core 1008 (Figs. 4.2; 4.8A) (Eberli et al., 1997; Malone et al., 2001). The lithified interval is overlain by unlithified sediments, which contain large blackened lithoclasts and foraminifera shells filled with dark micrite (Fig. 4.2; 4.3A). These sediments were deposited during the post-LGM sea-level rise. The lithoclasts consist of material eroded from the escarpment and the bank edge (Fig. 4.8A). Grammer and Ginsburg (1992) pointed out that the escarpment of the GBB was an important sediment

source during the sea-level rise after the LGM. Erosion by storms and waves, bioerosion and the failure of oversteeped ledges produced a large amount of debris, which deposited on the slope.

### M95-495

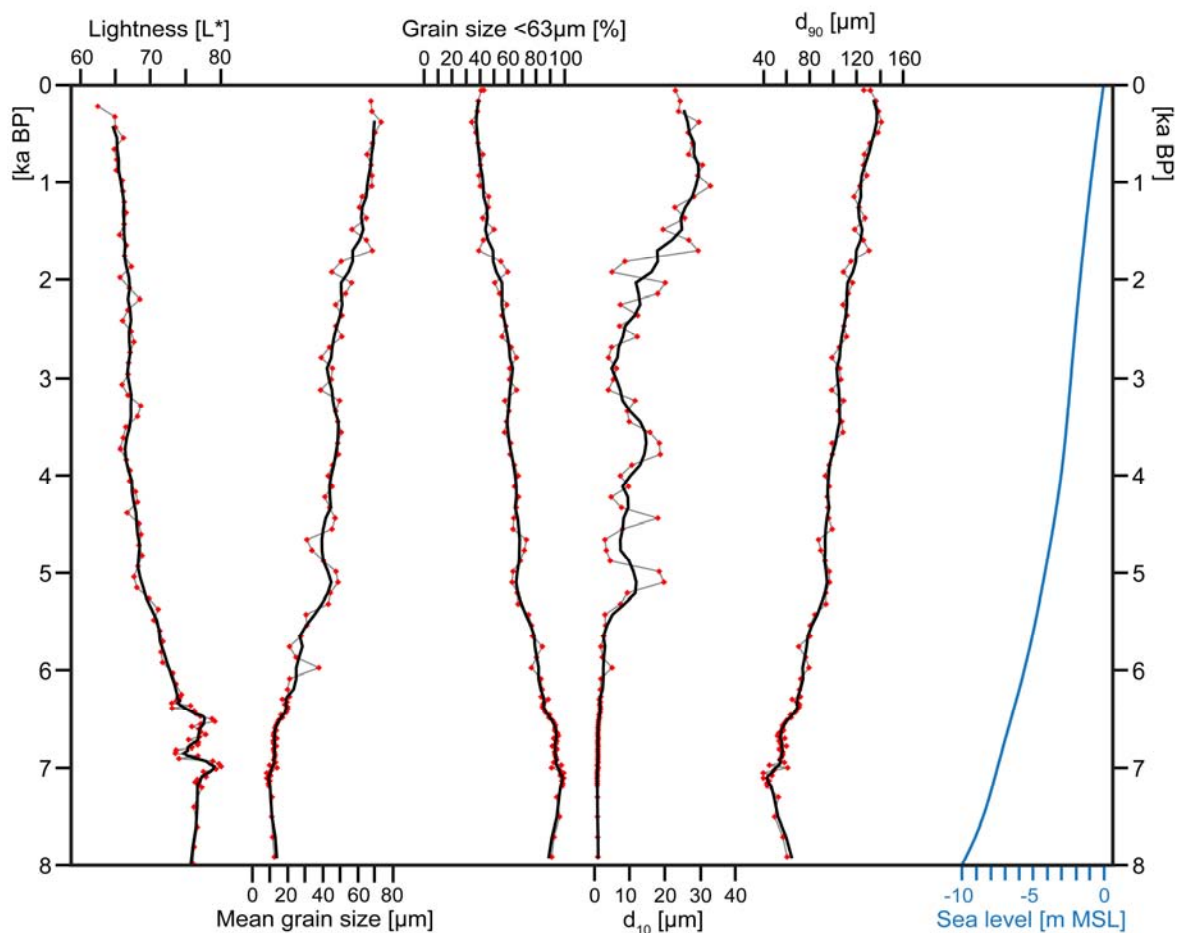


**Fig. 4.6:** Compilation of the optical lightness ( $L^*$ ), Mean grain size, the percentage of grains smaller  $63 \mu\text{m}$ , and the  $d_{10}$  and  $d_{90}$  percentiles, against the age. Bold black lines indicate 5-point running average. Position of samples used for age model is shown in Fig. 4.2. On the right hand side of the figure, the position of the sea level is shown (Data: Toscano and Macintyre, 2003).

#### 4.5.3 Early highstand stage (sea level position: -60 m to -5 m)

The early highstand stage comprises the time period between 13 and 5.5 ka BP, as the rising sea level submerged the leeward marginal areas of GBB (Fig. 4.8B). The platform top was flooded around 13 ka BP, as the rising sea level reached the bank edge that is nowadays located at a water depth of 60 m (Toscano and Macintyre, 2003; Jo et al., 2015). The highstand shedding of GBB began approx. around 7 ka BP (Roth and Reijmer, 2004). The sediment production resumed in the flooded parts and the platform exported fine-grained and mud-enriched sediments to the leeward slope. This mud mainly consists of aragonite needles. Aragonite needles are the predominant component in the mud fraction ( $<63 \mu\text{m}$ ) of

modern periplatform sediments (Schlager and James, 1978; Gischler et al., 2013). A high aragonite content correlates with increased  $L^*$  values (Fig. 4.6) (Roth and Reijmer, 2005). The most likely source for the aragonite needles during the early highstand stage is the calcareous algae *Halimeda*.

Dives along the escarpment and the leeward bank margin showed a profusion growth of *Halimeda* along the upper escarpment, whereas the bank margins are colonized by dense meadows of *Halimeda* (Ginsburg et al., 1991; Freile et al., 1995). Tides and wave action transport the produced sediments to the adjoined leeward slope. It is assumed that *Halimeda*, in a similar way, colonized the leeward bank margin, right after the re-flooding.

### M95-577

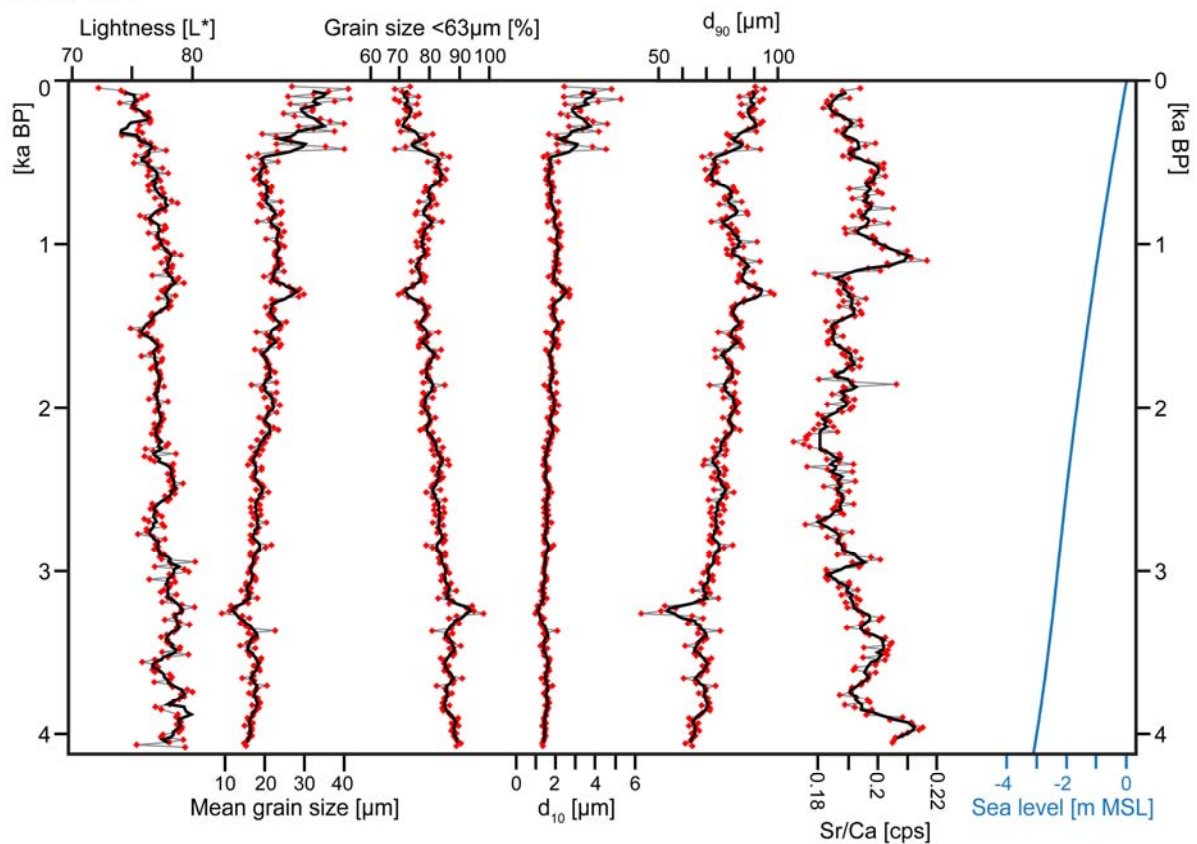


**Fig. 4.7:** Compilation of the optical lightness ( $L^*$ ), Mean grain size, the percentage of grains smaller 63  $\mu\text{m}$ , the  $d_{10}$  and  $d_{90}$  percentiles, and Sr/Ca ratio, against the age. Bold black lines indicate 5-point running average. Position of the sample used for age model is shown in Fig. 4.4. On the right hand side of the figure, the position of the sea level is shown (Data: Toscano and Macintyre, 2003).

On the slope, the exported sediments formed an initial sedimentary wedge, which was identified in the hydroacoustic data by Wunsch et al. (2016). Coarser sediments (e.g. complete *Halimeda* plates) remained on the platform or were deposited at the toe of the escarpment, whereas finer-grained sediments were transported to the distal part of the slope, where the core site of M95-495 is located.

The occurrence of whittings during the early highstand can be excluded, because the platform interior, the common place for the occurrence of whittings today was still emerged and the submerged platform parts had an unhindered water exchange with the adjoined Santaren Channel. The distribution of whittings on the GBB is nonrandom and 85% of all whittings are concentrated leeward of Andros Island (Robbins et al., 1997). In this area, the bank-top water is sheltered from the prevailing easterly trade winds, has the longest residence time on GBB and is supersaturated with respect to carbonate minerals such as aragonite (Broecker and Takahashi, 1966; Boss and Neumann, 1993). However, during the early highstand stage, the submerged platform parts had an unhindered water exchange with the adjoined Santaren channel.

#### **4.5.4 Late highstand stage (sea level position: >-5 m)**

Around 5 ka, the continuously rising sea level started to flood the platform interior. On the slope, this progressive flooding of the platform coincided with a gradual change in the sediment composition and a coarsening trend caused by increasing peloid export and a coarsening of the mud fraction (<63  $\mu\text{m}$ ) (Figs. 4.2; 4.6; 4.7; Tab. 4.1). In the mud fraction, the aragonite needles (<5  $\mu\text{m}$ ) became diluted by an increasing export of bioclasts and small peloids fragments (>10  $\mu\text{m}$ ) (Figs. 4.6; 4.7). This indicates the establishment of a pellet-producing bottom community in the shallow platform interior (Fig. 4.8C). Fecal pellets and peloids mainly consist of aragonitic mud and are supposed to be formed by sediment-feeding worms and crabs (Newell et al. 1959; Cloud, 1962). The incorporation of low-magnesium calcite and high-magnesium calcite (e.g. foraminifera fragments) components in the fecal pellets leads to an up to 20 % lower aragonite content, compared to pure aragonite mud (Stehli and Hower, 1961). Consequently, the aragonite content in the slope sediments will decrease with increasing pellet export.

The platform export was reinforced by the west-directed surface currents, which were able to cross the platform top with increasing water depths. On the leeward slope, this intensification of off-bank currents is reflected in the formation of the plunge pool (Betzler et al., 2014). The surface currents also influence the sediment distribution in the platform interior of GBB (Traverse and Ginsburg, 1966). Studies on the recent sediment distribution on the GBB support this assumed influence of surface currents and show that the platform top in the north and south of Andros Island is covered with coarser-grained sediments (grainstone, rudstone). Fine grained and mud-rich sediments (mudstone, wackestone), however, accumulate in the protected lee areas of Andros Island (Newell et al., 1959; Cloud, 1962; Purdy, 1963; Traverse and Ginsburg, 1966; Reijmer et al. 2009; Harris et al., 2015).

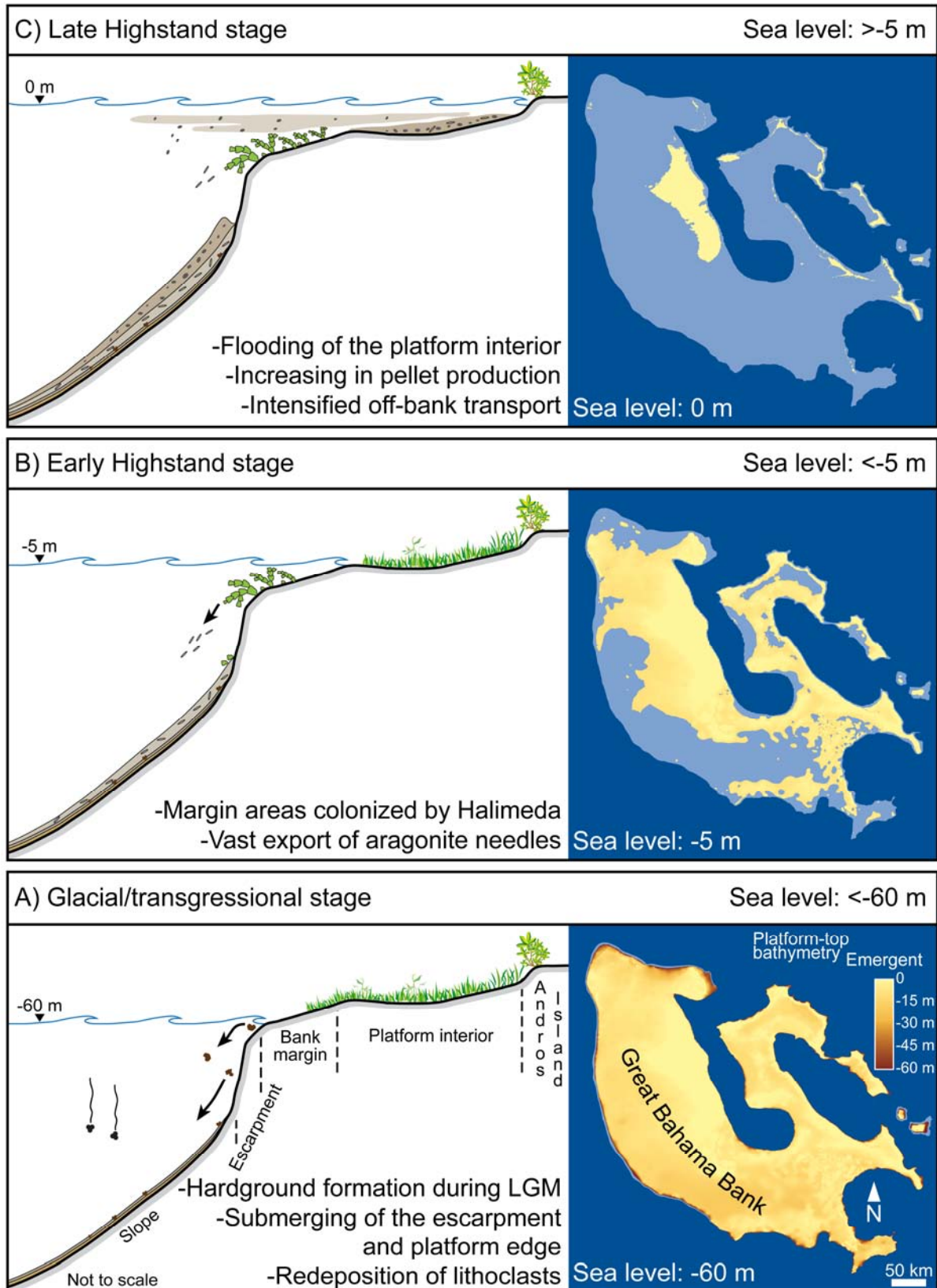


**Fig. 4.8:** Depositional model for the post-glacial flooding history of Great Bahama Bank, see discussion for details. Bathymetrical data from Harris et al. 2014; Smith and Sandwell 1997.

#### 4.5.5 Implications for the highstand shedding

A comparison of the herein presented core data with other Holocene successions shows that the encountered sedimentation pattern occurs along the complete leeward slope of GBB (Fig. 4.9). Indeed, highstand shedding is responsible for the high sedimentation rates along the leeward slope, but it seems to be more than a simple off-on mechanism, which continuously sheds sediments with the same composition into the surrounding basin (Schlager et al., 1994). In contrast to this, a subdivision is needed between early highstand and late highstand stage of platform export. During the early highstand stage, the carbonate production is restricted to the flooded marginal areas. The flooded parts export fine grained and aragonite-enriched sediments to the adjacent leeward slope. This stage correlates with the re-flooding window of carbonate platforms, proposed by Jorjy et al. (2010). The re-flooding window is a short period, in which the neritic carbonate production re-initiates. This time window is constrained by the bathymetry of the platform top and the position of sea level during the marine incursion. During the late highstand stage, with the successive flooding of the platform interior and the establishment of a pellet-producing benthic community, the platform export changed. The exported sediments show a coarsening-upward trend accompanied by decreasing aragonite content. This change in the sediment composition implies that the platform export (grain-size, components) is not only controlled by global factors (sea-level position, insolation) but rather local factors like the platform bathymetry or sediment-producing communities.

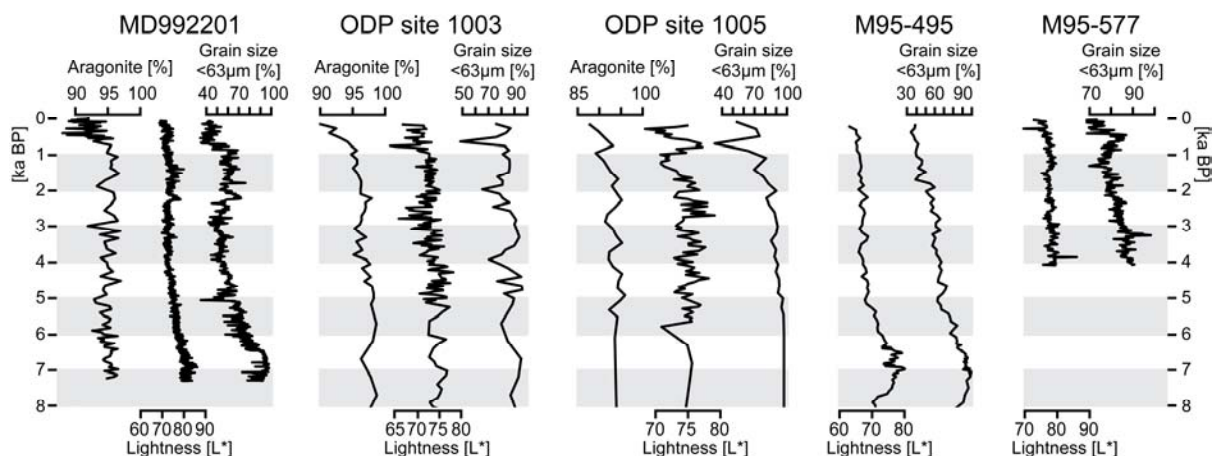


**Fig. 4.9:** Comparison of core data from the leeward slope of Great Bahama Bank, see Figure 1A for position. Aragonite content, optical lightness ( $L^*$ ), Grain size and age model of Core MD992201 after Roth 2003. Aragonite content and optical lightness ( $L^*$ ) for the ODP sites 1003 and 1005 after Eberli et al., 1997, Grain size data and age models after Rendle, 2000; Henderson et al. 2000.

The encountered changes in the slope sedimentation shown in this chapter have also implications for the interpretation or characterization of ancient slope successions and carbonate reservoirs. Sediment alterations in ancient slope successions, supposed to be deposited during one sea level cycle, are often interpreted as a result of environmental or oceanographic changes. This leads to the conclusion that such changes simply represent different stages of platform flooding. In terms of the characterization of a carbonate reservoir, changes in grain size and sediment composition influence directly the diagenetic processes and hence the spatial petrophysical properties, such as permeability, porosity and saturation of the solid rock (Lucia, 1995). This makes an accurate prediction of the reservoir properties challenging, because these heterogeneities are commonly beyond the resolution of reflection seismic data.



## *Chapter V*

### **Conclusions**

Chapter II determines the timing and the trigger mechanisms of slope failures, channel incisions and bedforms on two Bahamian slopes. These carbonate platform slopes are dissected by furrows, gullies and channels that are not necessarily genetically related. Several different mechanisms produce these slope features. This encompasses intensified off-bank transport and tectonic movements, as well as undercutting and erosion at the toe of slope by contour currents. Large mass transport complexes at platform flanks do not necessarily result from earthquakes, but also may be a consequence of differences in shear strength in the sedimentary succession characterized by an alternation of lithified lowstand and unlithified highstand depositional packages. During sea-level lowering, carbonate platform emersion can induce a downwelling current along the windward slope, which can erode the sediment on the platform top and transport it downslope, as demonstrated for the Cay Sal Bank. As a result, these sediments supply channels along the slope, and form falling stage deposits. Therefore, this chapter documents how different controlling factors impinge upon platform flanks and control heterogeneities in slope sedimentation. Through time, the combination of processes results in a spatially heterogeneous facies distribution, which should be taken into account when determining the variability of properties in ancient carbonate slopes.

Chapter III shows that contour currents are an underestimated factor in shaping the slope geometry. Along the leeward slope of Great Bahama Bank, current impact increases from south to north and is highest where the contour currents coalesce with the Florida Current. In this slope segment, constant current winnowing oversteepens the toe of slope triggering slope failures, incision of channels, and probably the accumulation of large mass transport complexes. To the south, large slope failures were rare and occurred primarily during sea level lowering. Rather than the simple occurrence of a sea-level drop, changes in the cyclicity or the amplitude of sea-level fluctuations seem to be important factors in triggering slope failures. Large slope failures occurred during the MPT and the MBE; periods characterized by sea-level fluctuations of varying amplitudes. The differences between the northern and southern part of the study area are also reflected in the facies distribution along the slope. In the north, where the current impact is strong, the facies distribution is complex. Facies distribution varies in both, the downslope and the along-strike direction. In the

southern part of the study area, where the current influence is weak, the facies heterogeneities occur primarily in downslope direction.

Chapter IV provides an analysis of two gravity cores from the leeward slope of Great Bahama Bank. The cored sediment succession consists of a hardground overlain by a packstone with large lithoclasts, a wackestone with a high content of aragonite needles, and a peloidal packstone on top. According to the encountered slope succession, the flooding history of the Great Bahama Bank can be subdivided into three stages: a glacial/transgression stage, an early highstand stage, and a late highstand stage. The glacial/transgression stage is represented by the lithified packstone (hardground) and the overlying packstone. During the early highstand stage, Halimeda meadows established in the flooded margin areas after the initial flooding of platform. The Halimeda meadows produced a vast amount of aragonite needles, which is represented in the slope succession as unlithified sediments with a wackestone texture. During the late highstand stage, the continuously rising sea level flooded the platform interior. In the platform interior, a pellet producing benthic community established. Consequently, the texture of the exported sediments changed from wackestone to packstone, accompanied by decreasing aragonite content. The described change of platform export shows that the concept of the highstand shedding can not be seen as a simple on-off mechanism, in which the platform export is only controlled by the sea-level position but that local factors like platform bathymetry and sediment-producing communities are also important in controlling texture and composition of exported sediments. This should be also taken into account when interpreting ancient slope successions, because such alternations in ancient succession are often interpreted as a result of environmental or oceanographic changes.

This thesis refines and expands established carbonate slope models by improving the understanding of the factors that control the sediment distribution and slope curvature. In established models for sedimentation on carbonate slopes, the sediment budget is tied to the position of the sea level. The sediments on the slope form margin-parallel facies belts along the slope, which are reported to show a fining towards the basin. The assumed trigger mechanisms for re-sedimentation processes (e.g. slope failures) are sea-level fluctuations or seismic shocks, induced by earthquakes. The established models need to be revised according to the obtained following main conclusions of this thesis.

*The main conclusions are:*

1. These carbonate platform slopes are dissected by furrows, gullies and channels. Despite morphological similarities, these slope features are not genetically related but the result of different mechanisms.
2. The influence of bottom- and contour currents is an underestimated factor in slope evolution on different scales. On a greater scale, the contour currents shape the slope curvature. Constant winnowing oversteepens the toe of slope and favors the incision of channels, slope failures and the accumulation of large mass transport complexes. On a smaller scale, bottom- and contour currents can influence the off-bank transport and gravity-driven processes (turbidity currents) by deflecting parts of the sediment load. In addition, sea-floor winnowing erodes finer-grained sediments and leads to complex facies variabilities and grain-size distributions along the slope, which make the development facies models challenging. The findings provide in this thesis can help to indentify indications for the impact of bottom- and contour currents in similar settings.
3. The morphology of the platform top has a great impact on the timing of slope sedimentation and sediment composition. In dependence of sea level position, the platform morphology can induce the accumulation of falling stage deposits or influences the composition of exported sediments. Both processes apply for carbonate platforms in comparable settings and similar platform top morphologies.
4. Large slope failures along the slope of Great Bahama Bank were triggered during time periods of irregular sea-level fluctuations. This implies that rather than the simple occurrence of a sea-level drop, the cyclicity or the amplitude of sea-level fluctuations seem to be important factors in triggering large slope failures along carbonate platform slopes.



## References

- Adams, E.W., Kenter, J.A.M.** (2013) So Different, Yet So Similar: Comparing and Contrasting Siliciclastic and Carbonate Slopes, in: *Deposits, Architecture, and Controls of Carbonate Margin, Slope, and Basinal Settings* (Eds. Verwer, K., Playton, T., Harris, P.M.). *SEPM Special Publication*, 105, 14–26.
- Alnazghah, M.H., Bádenas, B., Pomar, L., Aurell, M., Morsilli, M.** (2013) Facies heterogeneity at interwell-scale in a carbonate ramp, Upper Jurassic, NE Spain. *Marine and Petroleum Geology*, 44, 140–163.
- Anselmetti, F.S., Eberli, G.P., Ding, Z.-D.** (2000) From the Great Bahama Bank into the Straits of Florida: A margin architecture controlled by sea-level fluctuations and ocean currents. *Geological Society of America Bulletin*, 112, 829–844.
- Ball, M.M., Dillon, W.P., Wilber, R.J.** (1987) Comment and Reply on “Segmentation and coalescence of Cenozoic carbonate platforms, northwestern Great Bahama Bank.” *Geology*, 15, 1081–1082.
- Berger, W.H., Wefer, G.** (2003) On the dynamics of the ice ages: Stage-11 Paradox, mid-brunhes climate shift, and 100-ky cycle, in: *Earth's Climate and Orbital Eccentricity: The Marine Isotope Stage 11 Question* (Eds. Droxler, A.W., Poore, R.Z., Burckle, L.H.). *Geophysical Monograph Series*, 137, 41–59.
- Bergman, K.L.** (2005) *Seismic Analysis of Paleocurrent Features in the Florida Straits: Insights into the Paleo-Florida Current, Upstream Tectonics, and the Atlantic-Caribbean Connection* (unpublished Ph.D. thesis). University of Miami, Rosenstiel School of Marine and Atmospheric Sciences, Miami, 189 pp.
- Bergman, K.L., Westphal, H., Janson, X., Poiriez, A., Eberli, G.P.** (2010) Controlling Parameters on Facies Geometries of the Bahamas, an Isolated Carbonate Platform Environment, in: *Carbonate Depositional Systems: Assessing Dimensions and Controlling Parameters* (Eds. Westphal, H., Riegl, B., Eberli, G.P.). Springer, Dordrecht, The Netherlands, 5–80.
- Bernet, K., Eberli, G.P., Gilli, A.** (2000) Turbidite frequency and composition in the distal part of the Bahamas Transect, in: *Proceedings of the Ocean Drilling Program, Scientific Results, Leg 166* (Eds. Swart, P.K., Eberli, G.P., Malone, M.J., Sarg, J.F.). Ocean Drilling Program, College Station, USA, 45–60.
- Betzler, C., Reijmer, J.J.G., Bernet, K., Eberli, G.P., Anselmetti, F.S.** (1999) Sedimentary patterns and geometries of the Bahamian outer carbonate ramp (Miocene-Lower Pliocene, Great Bahama Bank). *Sedimentology*, 46, 1127–1143.
- Betzler, C., Lindhorst, S., Eberli, G.P., Lüdmann, T., Möbius, J., Ludwig, J., Schutter, I., Wunsch, M., Reijmer, J.J.G., Hübscher, C.** (2014) Periplatform drift: The combined result of contour current and off-bank transport along carbonate platforms. *Geology*, 42, 871–874.

- Billups, K.** (2002) Late Miocene through early Pliocene deep water circulation and climate change viewed from the sub-Antarctic South Atlantic. *Palaeogeography, Palaeoclimatology, Palaeoecology*, 185, 287–307.
- Black, K., Peppe, O., Gust, G.** (2003) Erodibility of pelagic carbonate ooze in the northeast Atlantic. *Journal of Experimental Marine Biology and Ecology*, 285–286, 143–163.
- Blanchette, F., Piche, V., Meiburg, E., Strauss, M.** (2006) Evaluation of a simplified approach for simulating gravity currents over slopes of varying angles. *Computers & Fluids*, 35, 492–500.
- Blondel, P.** (2009) *The handbook of sidescan sonar*. Springer, Berlin, Germany, 316 pp.
- Blott, S.J., Pye, K.** (2001) GRADISTAT: a grain size distribution and statistics package for the analysis of unconsolidated sediments. *Earth Surface Processes and Landforms*, 26, 1237–1248.
- Boardman, M.R., Neumann, A.C.** (1984) Sources of periplatform carbonates; Northwest Providence Channel, Bahamas. *Journal of Sedimentary Research*, 54, 1110–1123.
- Borgomano, J.R.F., Fournier, F., Viseur, S., Rijkels, L.** (2008) Stratigraphic well correlations for 3-D static modeling of carbonate reservoirs. *AAPG Bulletin*, 92, 789–824.
- Bosart, L.F., Schwartz, B.E.** (1979) Autumnal rainfall climatology of the Bahamas. *Monthly Weather Review*, 107, 1663–1672.
- Boss, S.K., Neumann, A.C.** (1993) Physical versus chemical processes of “whiting” formation in the Bahamas. *Carbonates and Evaporites*, 8, 135–148.
- Boss, S.K., Rasmussen, K.A.** (1995) Misuse of Fischer plots as sea-level curves. *Geology*, 23, 221–224.
- Broccoli, A.J.** (2000) Tropical Cooling at the Last Glacial Maximum: An Atmosphere–Mixed Layer Ocean Model Simulation. *Journal of Climate*, 13, 951–976.
- Broecker, W.S., Takahashi, T.** (1966) Calcium carbonate precipitation on the Bahama Banks. *Journal of Geophysical Research*, 71, 1575–1602.
- Carew, J.L., Mylroie, J.E.** (1995) Depositional model and stratigraphy for the Quaternary geology of the Bahama Islands, in: *Terrestrial and Shallow Marine Geology of the Bahamas and Bermuda* (Eds. Curran, H.A., White, B.). *GSA Special Papers*, 300, 5–32.
- Cartigny, M.J.B., Postma, G., van den Berg, J.H., Mastbergen, D.R.** (2011) A comparative study of sediment waves and cyclic steps based on geometries, internal structures and numerical modeling. *Marine Geology*, 280, 40–56.
- Chérubin, L.M.** (2014) High-resolution simulation of the circulation in the Bahamas and Turks and Caicos Archipelagos. *Progress in Oceanography*, 127, 21–46.
- Clark, P.U., Archer, D., Pollard, D., Blum, J.D., Rial, J.A., Brovkin, V., Mix, A.C., Pisias, N.G., Roy, M.** (2006) The middle Pleistocene transition: characteristics, mechanisms, and implications for long-term changes in atmospheric pCO<sub>2</sub>. *Quaternary Science Reviews*, 25, 3150–3184.

- Cloud, P.E.** (1962) Environment of calcium carbonate deposition west of Andros Island, Bahamas. *United States Geological Survey Professional Paper*, 360, 138pp.
- Collins, J., Narr, W., Harris, P.M., Playton, T., Jenkins, S., Tankersley, T., Kenter, J.A.M.** (2013) Lithofacies, Depositional Environments, Burial Diagenesis, and Dynamic Field Behavior in a Carboniferous Slope Reservoir, Tengiz Field (Republic of Kazakhstan), and Comparison With Outcrop Analogs, in: *Deposits, Architecture, and Controls of Carbonate Margin, Slope and Basinal Settings* (Eds. Verwer, K., Playton, T.E., Harris, P.M.). *SEPM Special Publication*, 105, 50–83.
- Correa, T.B.S., Grasmueck, M., Eberli, G.P., Reed, J.K., Verwer, K., Purkis, S.** (2012) Variability of cold-water coral mounds in a high sediment input and tidal current regime, Straits of Florida: Cold-water coral mound variability. *Sedimentology*, 59, 1278–1304.
- Deutsch, C.V., Journel, A.G.** (1998) *GSLIB: geostatistical software library and user's guide*, 2nd edition. Oxford University Press, New York, USA, 369 pp.
- Droxler, A.W., Schlager, W., Whallon, C.C.** (1983) Quaternary aragonite cycles and oxygen-isotope record in Bahamian carbonate ooze. *Geology*, 11, 235–239.
- Droxler, A.W., Schlager, W.** (1985) Glacial versus interglacial sedimentation rates and turbidite frequency in the Bahamas. *Geology*, 13, 799–802.
- Dunham, R.** (1962) Classification of carbonate rocks according to depositional textures, in: *Classification of Carbonate Rocks, A Symposium* (Ed. Ham, W.E.). *AAPG Memoir*, 1, 108–121.
- Eberli, G.P., Ginsburg, R.N.** (1987) Segmentation and coalescence of Cenozoic carbonate platforms, northwestern Great Bahama Bank. *Geology*, 15, 75–79.
- Eberli, G.P.** (1988) Physical Properties of Carbonate Turbidite Sequences Surrounding the Bahamas—Implications for Slope Stability and Fluid Movements, in: *Proceedings of the Ocean Drilling Program, Scientific Results, Leg 101* (Eds. Austin Jr., J.A., Schlager, W.). Ocean Drilling Program, College Station, USA, 305–314.
- Eberli, G.P., Ginsburg, R.N.** (1989) Cenozoic progradation of northwestern Great Bahama Bank, a record of lateral platform growth and sea-level fluctuations, in: *Controls on Carbonate Platform and Basin Development: Based on a Symposium* (Ed. Crevello, P.D.). *SEPM Special Publication*, 44, 339–351.
- Eberli, G.P.** (1991) Growth and Demise of Isolated Carbonate Platforms: Bahamian Controversies, in: *Controversies in Modern Geology* (Eds. Müller, D.W., MacKenzie, J.A., Weissert, H.). Academic Press, London, United Kingdom, 205–232.
- Eberli, G.P., Kendall, C.G.S.C., Moore, P., Whittle, G.L., Cannon, R.** (1994) Testing a seismic interpretation of Great Bahama Bank with a computer simulation. *AAPG Bulletin*, 78, 981–1004.
- Eberli, G.P., Swart, P.K., Malone, M.J.** (1997) *Proceedings of the Ocean Drilling Program, Initial Reports, Leg 166*. Ocean Drilling Program, College Station, USA, 850 pp.

- Eberli, G.P.** (2000) The record of Neogene sea-level changes in the prograding carbonates along the Bahamas Transect—Leg 166 synthesis, in: *Proceedings of the Ocean Drilling Program, Scientific Results, Leg 166* (Eds. Swart, P.K., Eberli, G.P., Malone, M.J., Sarg, J.F.). Ocean Drilling Program, College Station, USA, 167–177.
- Eberli, G.P., Anselmetti, F.S., Kroon, D., Sato, T., Wright, J.D.** (2002) The chronostratigraphic significance of seismic reflections along the Bahamas Transect. *Marine Geology*, 185, 1–17.
- Eberli, G.P., Anselmetti, F.S., Betzler, C., Van Konijnenburg, J.-H., Bernoulli, D.** (2004) Carbonate Platform to Basin Transitions on Seismic Data and in Outcrops: Great Bahama Bank and the Maiella Platform Margin, Italy, in: *Seismic Imaging of Carbonate Reservoirs and Systems* (Eds. Eberli, G.P., Masafarro, J.L., Sarg, J.F.). *AAPG Memoir*, 81, 207–250.
- Eberli, G.P.** (2013) The uncertainties involved in extracting amplitude and frequency of orbitally driven sea-level fluctuations from shallow-water carbonate cycles. *Sedimentology*, 60, 64–84.
- Embry, A.F., Klován, J.E.** (1971) A late Devonian reef tract on northeastern Banks Island, N.W.T. *Bulletin of Canadian Petroleum Geology*, 19, 730–781.
- Enos, P.** (1985) Cretaceous Debris Reservoirs, Poza Rica Field, Veracruz, Mexico, in: *Carbonate Petroleum Reservoirs* (Eds. Roehl, P.O., Choquette, P.W.). Springer, New York, USA, 455–469.
- EPICA Community** (2004) Eight glacial cycles from an Antarctic ice core. *Nature*, 429, 623–628.
- Fairbanks, R.G.** (1989) A 17,000-year glacio-eustatic sea level record: influence of glacial melting rates on the Younger Dryas event and deep-ocean circulation. *Nature*, 342, 637–642.
- Fleming, K., Johnston, P., Zwart, D., Yokoyama, Y., Lambeck, K., Chappell, J.** (1998) Refining the eustatic sea-level curve since the Last Glacial Maximum using far-and intermediate-field sites. *Earth and Planetary Science Letters*, 163, 327–342.
- Flügel, E.** (2010) *Microfacies of carbonate rocks: analysis, interpretation and application*, 2nd edition. Springer, Berlin, Germany, 984 pp.
- Folk, R.L., Ward, W.C.** (1957) Brazos River bar [Texas]; a study in the significance of grain size parameters. *Journal of Sedimentary Research*, 27, 3–26.
- Freile, D., Milliman, J.D., Hillis, L.** (1995) Leeward bank margin Halimeda meadows and draperies and their sedimentary importance on the western Great Bahama Bank slope. *Coral Reefs*, 14, 27–33.
- Gebelein, C.D.** (1974) *Guidebook for the modern bahamian platform environments*, *GSA Annual Meeting Fieldtrip Guide*. Geological Society of America, Boulder, USA, 94 pp.
- Ginsburg, R.N., Harris, P.M., Eberli, G.P., Swart, P.K.** (1991) The growth potential of a bypass margin, Great Bahama Bank. *Journal of Sedimentary Research*, 61, 976–987.

- Gischler, E., Dietrich, S., Harris, D., Webster, J.M., Ginsburg, R.N.** (2013) A comparative study of modern carbonate mud in reefs and carbonate platforms: Mostly biogenic, some precipitated. *Sedimentary Geology*, 292, 36–55.
- Goldberg, W.M.** (1983) Cay Sal Bank, Bahamas: a biologically impoverished, physically controlled environment. *Atoll Research Bulletin*, 271, 1–17.
- Gradstein, F.M., Ogg, J.G., Schmitz, M.D., Ogg, G.M. (Eds.)** (2012) *The geologic time scale 2012*, 1st edition. Elsevier, Kidlington, United Kingdom, 1144 pp.
- Grammer, G.M., Ginsburg, R.N.** (1992) Highstand versus lowstand deposition on carbonate platform margins: insight from Quaternary foreslopes in the Bahamas. *Marine Geology*, 103, 125–136.
- Grammer, G.M., Ginsburg, R.N., Harris, P.M.** (1993) Timing of Deposition, Diagenesis, and Failure of Steep Carbonate Slopes in Response to a High-Amplitude/High-Frequency Fluctuation in Sea Level, Tongue of the Ocean, Bahamas, in: *Carbonate Sequence Stratigraphy: Recent Developments and Applications* (Eds. Loucks, R.G., Sarg, J.F). *AAPG Memoir*, 57, 107–131.
- Grasmueck, M., Eberli, G.P., Viggiano, D.A., Correa, T., Rathwell, G., Luo, J.** (2006) Autonomous underwater vehicle (AUV) mapping reveals coral mound distribution, morphology, and oceanography in deep water of the Straits of Florida. *Geophysical Research Letters*, 33, Doi: 10.1029/2006GL027734.
- Harris, P.M., Purkis, S.J., Ellis, J.** (2014) *Evaluating Water-Depth Variation and Mapping Depositional Facies on the Great Bahama Bank – a “Flat-Topped” Isolated Carbonate Platform*. SEPM Short Course Notes, 56, 48 pp.
- Harris, P.M., Purkis, S.J., Ellis, J., Swart, P.K., Reijmer, J.J.G.** (2015) Mapping bathymetry and depositional facies on Great Bahama Bank. *Sedimentology*, 62, 566–589.
- Harwood, G., Towers, P.** (1988) Seismic sedimentologic interpretation of a carbonate slope, north margin of Little Bahama Bank, in: *Proceedings of the Ocean Drilling Program, Scientific Results, Leg 101* (Eds. Austin Jr., J.A., Schlager, W.). Ocean Drilling Program, Collage Station, USA, 263–277.
- Haug, G.H., Tiedemann, R.** (1998) Effect of the formation of the Isthmus of Panama on Atlantic Ocean thermohaline circulation. *Nature*, 393, 673–676.
- Haug, G.H., Tiedemann, R., Zahn, R., Ravelo, A.C.** (2001) Role of Panama uplift on oceanic freshwater balance. *Geology*, 29, 207–210.
- Hearty, P.J.** (1998) The geology of Eleuthera Island, Bahamas: A Rosetta Stone of Quaternary stratigraphy and sea-level history. *Quaternary Science Reviews*, 17, 333–355.
- Hearty, P.J., Neumann, A.C.** (2001) Rapid sea level and climate change at the close of the Last Interglaciation (MIS 5e): evidence from the Bahama Islands. *Quaternary Science Reviews*, 20, 1881–1895.
- Hearty, P.J., Hollin, J.T., Neumann, A.C., O’Leary, M.J., McCulloch, M.** (2007) Global sea-level fluctuations during the Last Interglaciation (MIS 5e). *Quaternary Science Reviews*, 26, 2090–2112.

- Hebbeln, D., Wienberg, C., and cruise participants** (2012) Report and preliminary results of R/V Maria S. Merian cruise MSM20-4. WACOM - West-Atlantic Cold-water Corals Ecosystems: The West Side Story. Bridgetown - Freeport, 14 March - 7 April 2012. *Berichte aus dem MARUM und dem Fachbereich Geowissenschaften der Universität Bremen*, 290, 53 pp.
- Henderson, G.M., Rendle, R.H., Slowey, N.C., Reijmer, J.J.G.** (2000) U-Th dating and diagenesis of Pleistocene highstand sediments from the Bahamas Slope, in: *Proceedings of the Ocean Drilling Program, Scientific Results, Leg 166* (Eds. Swart, P.K., Eberli, G.P., Malone, M.J., Sarg, J.F.). Ocean Drilling Program, College Station, USA, 23–31.
- Henderson, G.M., Robinson, L.F., Cox, K., Thomas, A.L.** (2006) Recognition of non-Milankovitch sea-level highstands at 185 and 343 thousand years ago from U-Th dating of Bahamas sediment. *Quaternary Science Reviews*, 25, 3346–3358.
- Hine, A.C., Wilber, R.J., Neumann, A.C.** (1981) Carbonate sand bodies along contrasting shallow bank margins facing open seaways in northern Bahamas. *AAPG Bulletin*, 65, 261–290.
- Hine, A.C., Steinmetz, J.C.** (1984) Cay Sal Bank, Bahamas-A partially drowned carbonate platform. *Marine Geology*, 59, 135–164.
- Jaime Gómez-Hernández, J., Mohan Srivastava, R.** (1990) ISIM3D: An ANSI-C three-dimensional multiple indicator conditional simulation program. *Computers & Geosciences*, 16, 395–440.
- Janson, X., Kerans, C., Loucks, R., Marhx, M.A., Reyes, C., Murguía, F.** (2011) Seismic architecture of a Lower Cretaceous platform-to-slope system, Santa Agueda and Poza Rica fields, Mexico. *AAPG Bulletin*, 95, 105–146.
- Jo, A., Eberli, G.P., Grasmueck, M.** (2015) Margin collapse and slope failure along southwestern Great Bahama Bank. *Sedimentary Geology*, 317, 43–52.
- Jorry, S.J., Droxler, A.W., Francis, J.M.** (2010) Deepwater carbonate deposition in response to re-flooding of carbonate bank and atoll-tops at glacial terminations. *Quaternary Science Reviews*, 29, 2010–2026.
- Journel, A.G.** (1983) Nonparametric estimation of spatial distributions. *Journal of the International Association for Mathematical Geology*, 15, 445–468.
- Kaneps, A.G.** (1979) Gulf Stream: Velocity Fluctuations During the Late Cenozoic. *Science*, 204, 297–301.
- Kendall, C.G.S.C., Schlager, W.** (1981) Carbonates and relative changes in sea level. *Marine Geology*, 44, 181–212.
- Kenter, J.A.M.** (1990) Carbonate platform flanks: slope angle and sediment fabric. *Sedimentology*, 37, 777–794.

- Kenter, J.A.M., Ginsburg, R.N., Troelstra, S.R.** (2001) Sea-level-driven sedimentation patterns on the slope and margin, in: *Subsurface Geology of a Prograding Carbonate Platform Margin, Great Bahama Bank: Results of the Bahamas Drilling Project* (Eds. Ginsburg, R.N., Warzeski, E.R.). *SEPM Special Publication*, 70, 61–100.
- Kenter, J.A.M., Harris, P.M., Della Porta, G.** (2005) Steep microbial boundstone-dominated platform margins—examples and implications. *Sedimentary Geology*, 178, 5–30.
- Kievman, C.M.** (1998) Match between late Pleistocene Great Bahama Bank and deep-sea oxygen isotope records of sea level. *Geology*, 26, 635–638.
- Kostic, S.** (2011) Modeling of submarine cyclic steps: Controls on their formation, migration, and architecture. *Geosphere*, 7, 294–304.
- Kourafalou, V.H., Kang, H.** (2012) Florida Current meandering and evolution of cyclonic eddies along the Florida Keys Reef Tract: Are they interconnected? *Journal of Geophysical Research*, 117, Doi: 10.1029/2011JC007383.
- Kroon, D., Reijmer, J.J.G., Rendle, R.H.** (2000) Mid- to late-Quaternary variations in the oxygen isotope signature of Globigerinoides ruber at Site 1006 in the western subtropical Atlantic, in: *Proceedings of the Ocean Drilling Program, Scientific Results, Leg 166* (Eds. Swart, P.K., Eberli, G.P., Malone, M.J., Sarg, J.F.). Ocean Drilling Program, College Station, USA, 13–22.
- Kula, D.** (2014) *Neotectonics on the Edge of the Cuban Fold and Thrust Belt* (Published Master Thesis). University of Miami, Rosenstiel School of Marine and Atmospheric Sciences, Miami, 118 pp.
- Laberg, J.S., Camerlenghi, A.** (2008) Chapter 25 The Significance of Contourites for Submarine Slope Stability, in: *Developments in Sedimentology Contourites* (Eds. Rebesco, M., Camerlenghi, A.). Elsevier Science Ltd, Oxford, United Kingdom. 537–556.
- Ladd, J.W., Sheridan, R.E.** (1987) Seismic stratigraphy of the Bahamas. *AAPG Bulletin*, 71, 719–736.
- Leaman, K.D., Vertes, P.S., Atkinson, L.P., Lee, T.N., Hamilton, P., Waddell, E.** (1995) Transport, potential vorticity, and current/temperature structure across Northwest Providence and Santaren Channels and the Florida Current off Cay Sal Bank. *Journal of Geophysical Research*, 100, 8561–8569.
- Lee, T.N., Leaman, K., Williams, E., Berger, T., Atkinson, L.** (1995) Florida Current meanders and gyre formation in the southern Straits of Florida. *Journal of Geophysical Research*, 100, 8607–8620.
- Lucia, F.J.** (1995) Rock-Fabric/Petrophysical Classification of Carbonate Pore Space for Reservoir Characterization. *AAPG Bulletin*, 79, 1275–1300.
- Lüdmann, T., Paulat, M., Betzler, C., Möbius, J., Lindhorst, S., Wunsch, M., Eberli, G.P.** (2016) Carbonate mounds in the Santaren Channel, Bahamas: A current-dominated periplatform depositional regime. *Marine Geology*, 376, 69–85.

- Lynch-Stieglitz, J., Curry, W., Slowey, N.C.** (1999) Weaker Gulf Stream in the Florida Straits during the Last Glacial Maximum. *Nature*, 402, 644–648.
- Malone, M.J.** (2000) Data report: geochemistry and mineralogy of periplatform carbonate sediments: Sites 1006, 1008, and 1009, in: *Proceedings of the Ocean Drilling Program, Scientific Results; Leg 166* (Eds. Swart, P.K., Eberli, G.P., Malone, M.J., Sarg, J.F.). Ocean Drilling Program, College Station, USA, 145–152.
- Malone, M.J., Slowey, N.C., Henderson, G.M.** (2001) Early diagenesis of shallow-water periplatform carbonate sediments, leeward margin, Great Bahama Bank (Ocean Drilling Program Leg 166). *Geological Society of America Bulletin*, 113, 881–894.
- Manfrino, C., Ginsburg, R.N.** (2001) Pliocene to Pleistocene Depositional History of the Upper Platform Margin, in: *Subsurface Geology of a Prograding Carbonate Platform Margin, Great Bahama Bank: Results of the Bahamas Drilling Project* (Eds. Ginsburg, R.N., Warzeski, E.R.). *SEPM Special Publication*, 70, 61–100.
- Masaferro, J.L.** (1997) *Interplay of tectonism and carbonate sedimentation in the Bahamas foreland basin* (Published Ph.D. thesis). University of Miami, Rosenstiel School of Marine and Atmospheric Sciences, Miami, 147 pp.
- Masaferro, J.L., Eberli, G.P.** (1999) Jurassic-cenozoic structural evolution of the southern great Bahama bank, in: *Sedimentary Basins of the World* (Ed. Mann, P.). Elsevier, Amsterdam, The Netherlands, 167–193.
- Masaferro, J.L., Poblet, J., Bulnes, M., Eberli, G.P., Dixon, T.H., McClay, K.** (1999) Palaeogene-Neogene/present day(?) growth folding in the Bahamian foreland of the Cuban fold and thrust belt. *Journal of the Geological Society*, 156, 617–631.
- Masaferro, J.L., Bulnes, M., Poblet, J., Eberli, G.P.** (2002) Episodic folding inferred from syntectonic carbonate sedimentation: the Santaren anticline, Bahamas foreland. *Sedimentary Geology*, 146, 11–24.
- Maslin, M.A., Brierley, C.M.** (2015) The role of orbital forcing in the Early Middle Pleistocene Transition. *Quaternary International*, 389, 47–55.
- Meyerhoff, A.A., Hatten, C.W.** (1974) Bahamas Salient of North America: Tectonic Framework, Stratigraphy, and Petroleum Potential. *AAPG Bulletin*, 58, 1201–1239.
- Mulder, T., Ducassou, E., Eberli, G.P., Hanquiez, V., Gonthier, E., Kindler, P., Principaud, M., Fournier, F., Leonide, P., Billeaud, I., Marsset, B., Reijmer, J.J.G., Bondu, C., Joussiaume, R., Pakiades, M.** (2012) New insights into the morphology and sedimentary processes along the western slope of Great Bahama Bank. *Geology*, 40, 603–606.
- Mullins, H.T., Lynts, G.W.** (1977) Origin of the northwestern Bahama Platform: Review and reinterpretation. *Geological Society of America Bulletin*, 88, 1447–1461.
- Neumann, A.C., Ball, M.M.** (1970) Submersible Observations in the Straits of Florida: Geology and Bottom Currents. *Geological Society of America Bulletin*, 81, 2861–2873.
- Neumann, A.C., Hearty, P.J.** (1996) Rapid sea-level changes at the close of the last interglacial (substage 5e) recorded in Bahamian island geology. *Geology*, 24, 775–778.

- Newell, N.D., Imbrie, J.** (1955) Biogeological Reconnaissance in the Bimini area, Great Bahama Bank. *Transactions of the New York Academy of Sciences*, 18, 3–14.
- Newell, N.D., Imbrie, J., Purdy, E.G., Thurber, D.L.** (1959) *Organism communities and bottom facies, Great Bahama Bank*. Bulletin of the American Museum of Natural History, 117, 65 pp.
- Parker, G., Fukushima, Y., Pantin, H.M.** (1986) Self-accelerating turbidity currents. *Journal of Fluid Mechanics*, 171, 145–181.
- Peterson, L.C., Haug, G.H., Hughen, K.A., Röhl, U.** (2000) Rapid Changes in the Hydrologic Cycle of the Tropical Atlantic During the Last Glacial. *Science*, 290, 1947–1951.
- Pisias, N.G., Moore, T.C.** (1981) The evolution of Pleistocene climate: A time series approach. *Earth and Planetary Science Letters*, 52, 450–458.
- Playton, T.E., Janson, X., Kerans, C.** (2010) Carbonate slopes, in: *Facies Models 4* (Eds. James, N.P., Dalrymple, R.W.). Geological Association of Canada, St. Johns, 449–476.
- Prager, E.J., Southard, J.B., Vivoni-Gallart, E.R.** (1996) Experiments on the entrainment threshold of well-sorted and poorly sorted carbonate sands. *Sedimentology*, 43, 33–40.
- Principaud, M.** (2015) *Morphologie, Architecture et dynamique Sédimentaire d'une pente carbonatée moderne: le Great Bahama Bank (Bahamas)* (Published Ph.D. thesis). University of Bordeaux, Bordeaux, 320 pp.
- Principaud, M., Mulder, T., Gillet, H., Borgomano, J.** (2015) Large-scale carbonate submarine mass-wasting along the northwestern slope of the Great Bahama Bank (Bahamas): Morphology, architecture, and mechanisms. *Sedimentary Geology*, 317, 27–42.
- Principaud, M., Ponte, J.-P., Mulder, T., Gillet, H., Robin, C., Borgomano, J.** (2016) Slope-to-basin stratigraphic evolution of the carbonate northwestern Great Bahama Bank (Bahamas) during the Neogene to Quaternary: interactions between downslope and bottom currents deposits. *Basin Research*, Doi: 10.1111/br.12195.
- Puga-Bernabéu, Á., Webster, J.M., Beaman, R.J., Guilbaud, V.** (2011) Morphology and controls on the evolution of a mixed carbonate–siliciclastic submarine canyon system, Great Barrier Reef margin, north-eastern Australia. *Marine Geology*, 289, 100–116.
- Purdy, E.G.** (1963) Recent Calcium Carbonate Facies of the Great Bahama Bank. 2. Sedimentary Facies. *The Journal of Geology*, 71, 472–497.
- Purkis, S., Kerr, J., Dempsey, A., Calhoun, A., Metsamaa, L., Riegl, B., Kourafalou, V., Bruckner, A., Renaud, P.** (2014) Large-scale carbonate platform development of Cay Sal Bank, Bahamas, and implications for associated reef geomorphology. *Geomorphology*, 222, 25–38.
- Raymo, M.E., Hodell, D., Jansen, E.** (1992) Response of deep ocean circulation to initiation of northern hemisphere glaciation (3–2 MA). *Paleoceanography*, 7, 645–672.

- Raymo, M.E., Grant, B., Horowitz, M., Rau, G.H.** (1996) Mid-Pliocene warmth: stronger greenhouse and stronger conveyor. *Marine Micropaleontology*, 27, 313–326.
- Reijmer, J.J., Betzler, C., Kroon, D., Tiedemann, R., Eberli, G.P.** (2002) Bahamian carbonate platform development in response to sea-level changes and the closure of the Isthmus of Panama. *International Journal of Earth Sciences*, 91, 482–489.
- Reijmer, J.J.G., Swart, P.K., Bauch, T., Otto, R., Reuning, L., Roth, S., Zechel, S.** (2009) A Re-Evaluation of Facies on Great Bahama Bank I: New Facies Maps of Western Great Bahama Bank, in: *Perspectives in Carbonate Geology: A Tribute to the Career of Robert Nathan Ginsburg* (Eds. Swart, P.K., Eberli, G.P., McKenzie, J.A., Jarvis, I., Stevens, T.). *IAS Special Publication*, 41, Wiley-Blackwell, Chichester, United Kingdom, 29–46.
- Reijmer, J.J.G., Mulder, T., Borgomano, J.** (2015) Carbonate slopes and gravity deposits. *Sedimentary Geology*, 317, 1–8.
- Reimer, P.J., Bard, E., Bayliss, A., Beck, J.W., Blackwell, P.G., Ramsey, C.B., Buck, C.E., Cheng, H., Edwards, R.L., Friedrich, M., Grootes, P.M., Guilderson, T.P., Hafliðason, H., Hajdas, I., Hatté, C., Heaton, T.J., Hoffmann, D.L., Hogg, A.G., Hughen, K.A., Kaiser, K.F., Kromer, B., Manning, S.W., Niu, M., Reimer, R.W., Richards, D.A., Scott, E.M., Southon, J.R., Staff, R.A., Turney, C.S.M., van der Plicht, J.** (2013) IntCal13 and Marine13 Radiocarbon Age Calibration Curves 0–50,000 Years cal BP. *Radiocarbon*, 55, 1869–1887.
- Rendle, R.H.** (2000) *Quaternary Slope Development and Sedimentology of the Western, Leeward Margin of Great Bahama Bank (ODP Leg 166)* (Published PhD thesis). Christian-Albrechts-Universität, Kiel, 182 pp.
- Rendle, R.H., Reijmer, J.J.G., Kroon, D., Henderson, G.M.** (2000) Mineralogy and sedimentology of the Pleistocene to Holocene on the Leeward margin of Great Bahama Bank, in: *Proceedings of the Ocean Drilling Program, Scientific Results, Leg 166* (Eds. Swart, P.K., Eberli, G.P., Malone, M.J., Sarg, J.F.). Ocean Drilling Program, College Station, USA, 61–76.
- Rendle, R.H., Reijmer, J.J.G.** (2002) Quaternary slope development of the western, leeward margin of the Great Bahama Bank. *Marine Geology*, 185, 143–164.
- Rendle-Bühning, R.H., Reijmer, J.J.G.** (2005) Controls on grain-size patterns in periplatform carbonates: Marginal setting versus glacio-eustacy. *Sedimentary Geology*, 175, 99–113.
- Reolid, J., Betzler, C., Braga, J.C., Martín, J.M., Lindhorst, S., Reijmer, J.J.G.** (2014) Reef slope geometries and facies distribution: controlling factors (Messinian, SE Spain). *Facies*, 60, 737–753.
- Robbins, L.L., Tao, Y., Evans, C.A.** (1997) Temporal and spatial distribution of whittings on Great Bahama Bank and a new lime mud budget. *Geology*, 25, 947–950.
- Robinson, L.F., Henderson, G.M., Slowey, N.C.** (2002) U–Th dating of marine isotope stage 7 in Bahamas slope sediments. *Earth and Planetary Science Letters*, 196, 175–187.

- Roth, S.** (2003) *Holocene climate variations recorded on the western flank of Great Bahama Bank* (Published Ph.D. thesis). Christian-Albrechts-Universität, Kiel, 137 pp.
- Roth, S., Reijmer, J.J.G.** (2004) Holocene Atlantic climate variations deduced from carbonate periplatform sediments (leeward margin, Great Bahama Bank). *Paleoceanography*, 19, Doi: 10.1029/2003PA000885.
- Roth, S., Reijmer, J.J.G.** (2005) Holocene millennial to centennial carbonate cyclicity recorded in slope sediments of the Great Bahama Bank and its climatic implications: Holocene carbonate cyclicity. *Sedimentology*, 52, 161–181.
- Rothwell, R.G., Hoogakker, B., Thomson, J., Croudace, I.W., Frenz, M.** (2006) Turbidite emplacement on the southern Balearic Abyssal Plain (western Mediterranean Sea) during Marine Isotope Stages 1–3: an application of ITRAX XRF scanning of sediment cores to lithostratigraphic analysis, in: *New Techniques in Sediment Core Analysis* (Ed. Rothwell, R.G.). *Geological Society Special Publications*, 267, London, United Kingdom, 79–98.
- Sarg, J.F.** (1988) Carbonate sequence stratigraphy, in: *Sea-Level Changes: An Integrated Approach* (Eds. Wilgus, C.K., Hastings, B.S., Kendall, C.G.S.C., Posamentier, H., Ross, C.A., Van Wagoner, J.). *SEPM Special Publication*, 42, 155–181.
- Schlager, W., James, N.P.** (1978) Low-magnesian calcite limestones forming at the deep-sea floor, Tongue of the Ocean, Bahamas. *Sedimentology*, 25, 675–702.
- Schlager, W., Ginsburg, R.N.** (1981) Bahama carbonate platforms — The deep and the past. *Marine Geology*, 44, 1–24.
- Schlager, W., Camber, O.** (1986) Submarine slope angles, drowning unconformities, and self-erosion of limestone escarpments. *Geology*, 14, 762–765.
- Schlager, W., Reijmer, J.J.G., Droxler, A.W.** (1994) Highstand Shedding of Carbonate Platforms. *Journal of Sedimentary Research*, B64, 270–281.
- Schmidt, M.W., Spero, H.J.** (2011) Meridional shifts in the marine ITCZ and the tropical hydrologic cycle over the last three glacial cycles. *Paleoceanography*, 26, Doi: 10.1029/2010PA001976.
- Schmitz, W.J., Richardson, P.L.** (1991) On the sources of the Florida Current. Deep Sea Research Part A. *Oceanographic Research Papers*, 38, 379–409.
- Schnyder, J.S.D., Jo, A., Eberli, G.P., Betzler, C., Lindhorst, S., Schiebel, L., Hebbeln, D., Winterseller, P., Mulder, T., Principaud, M.** (2014) A 5000km<sup>2</sup> data set along western Great Bahama Bank illustrates the dynamics of carbonate slope deposition, in: *Geophysical Research Abstracts Vol. 16*. (Presented at the EGU General Assembly 2014).
- Schott, F.A., Lee, T.N., Zantopp, R.** (1988) Variability of Structure and Transport of the Florida Current in the Period Range of Days to Seasonal. *Journal of Physical Oceanography*, 18, 1209–1230.
- Sealey, N.E.** (1994) *Bahamian landscapes: an introduction to the geology and physical geography of the Bahamas*. Media Publishing, Nassau, Bahamas, 174pp.

- Shackleton, N.J., Opdyke, N.D.** (1976) Oxygen-Isotope and Paleomagnetic Stratigraphy of Pacific Core V28-239 Late Pliocene to Latest Pleistocene, in: Investigation of Late Quaternary Paleoceanography and Paleoclimatology (Eds. Cune, R.M., Hays, J.D.). GSA Memoir, 145, 449–463.
- Siddall, M., Rohling, E.J., Almogi-Labin, A., Hemleben, C., Meischner, D., Schmelzer, I., Smeed, D.A.** (2003) Sea-level fluctuations during the last glacial cycle. *Nature*, 423, 853–858.
- Slowey, N.C., Wilber, R.J., Haddad, G.A., Henderson, G.M.** (2002) Glacial-to-Holocene sedimentation on the western slope of Great Bahama Bank. *Marine Geology*, 185, 165–176.
- Smith, W.H.F., Sandwell, D.T.** (1997) Global Sea Floor Topography from Satellite Altimetry and Ship Depth Soundings. *Science*, 277, 1956–1962.
- Southard, J.B., Young, R.A., Hollister, C.D.** (1971) Experimental erosion of calcareous ooze. *Journal of Geophysical Research*, 76, 5903–5909.
- Stehli, F.G., Hower, J.** (1961) Mineralogy and early diagenesis of carbonate sediments. *Journal of Sedimentary Research*, 31, 358–371.
- Steph, S., Tiedemann, R., Prange, M., Groeneveld, J., Nürnberg, D., Reuning, L., Schulz, M., Haug, G.H.** (2006) Changes in Caribbean surface hydrography during the Pliocene shoaling of the Central American Seaway. *Paleoceanography*, 21, Doi: 10.1029/2004PA001092.
- Steph, S., Tiedemann, R., Prange, M., Groeneveld, J., Schulz, M., Timmermann, A., Nürnberg, D., Rühlemann, C., Saukel, C., Haug, G.H.** (2010) Early Pliocene increase in thermohaline overturning: A precondition for the development of the modern equatorial Pacific cold tongue. *Paleoceanography*, 25, Doi: 10.1029/2008PA001645.
- Stow, D.A.V., Hernández-Molina, F.J., Llave, E., Sayago-Gil, M., Diaz del Rio, V., Branson, A.** (2009) Bedform-velocity matrix: The estimation of bottom current velocity from bedform observations. *Geology*, 37, 327–330.
- Stuiver, M., Reimer, P.J.** (1993) Extended  $^{14}\text{C}$  Data Base and Revised CALIB 3.0  $^{14}\text{C}$  Age Calibration Program. *Radiocarbon*, 35, 215–230.
- Toscano, M.A., Macintyre, I.G.** (2003) Corrected western Atlantic sea-level curve for the last 11,000 years based on calibrated  $^{14}\text{C}$  dates from *Acropora palmata* framework and intertidal mangrove peat. *Coral Reefs*, 22, 257–270.
- Tournadour, E., Mulder, T., Borgomano, J., Hanquiez, V., Ducassou, E., Gillet, H.** (2015) Origin and architecture of a Mass Transport Complex on the northwest slope of Little Bahama Bank (Bahamas): Relations between off-bank transport, bottom current sedimentation and submarine landslides. *Sedimentary Geology*, 317, 9–26.
- Traverse, A., Ginsburg, R.N.** (1966) Palynology of the surface sediments of Great Bahama Bank, as related to water movement and sedimentation. *Marine Geology*, 4, 417–459.
- Wallis, F.E.** (1993) Tectonic and diagenetically induced seal failure within the southwestern Great Bahamas Bank. *Marine and Petroleum Geology*, 10, 14–28.

- Wang, J., Mooers, C.N.K.** (1997) Three-dimensional perspectives of the Florida current: transport, potential vorticity, and related dynamical properties. *Dynamics of Atmospheres and Oceans*, 27, 135–149.
- Werner, F., Unsöld, G., Koopmann, B., Stefanon, A.** (1980) Field observations and flume experiments on the nature of comet marks. *Sedimentary Geology*, 26, 233–262.
- Wilber, R.J., Milliman, J.D., Halley, R.B.**, (1990) Accumulation of bank-top sediment on the western slope of Great Bahama Bank: Rapid progradation of a carbonate megabank. *Geology*, 18, 970–974.
- Wilber, R.J., Whitehead, J., Halley, R.B., Milliman, J.D., Wilson, P.A., Roberts, H.H.** (1993) Carbonate-periplatform sedimentation by density flows: A mechanism for rapid off-bank and vertical transport of shallow-water fines: Comment and Reply. *Geology*, 21, 667–668.
- Wilson, P.A., Roberts, H.H.** (1992) Carbonate-periplatform sedimentation by density flows: A mechanism for rapid off-bank and vertical transport of shallow-water fines. *Geology*, 20, 713–716.
- Wilson, P.A., Robert, H.H.** (1995) Density Cascading: Off-shelf Sediment Transport, Evidence and Implications, Bahama Banks. *Journal of Sedimentary Research*, 65A, 45–56.
- Wright, J.D., Kroon, D.** (2000) Planktonic Foraminiferal Biostratigraphy of Leg 166, in: *Proceedings of the Ocean Drilling Program, Scientific Results, Leg 166* (Eds. Swart, P.K., Eberli, G.P., Malone, M.J., Sarg, J.F.). Ocean Drilling Program, College Station, USA, 3–12.
- Wunsch, M., Betzler, C., Lindhorst, S., Lüdmann, T., Eberli, G.P.** (2016) Sedimentary dynamics along carbonate slopes (Bahamas archipelago). *Sedimentology*, 64, 631–657.



## Acknowledgments

The completion of this thesis would not have been possible without a continued support of many people. First, I would like to thank my supervisor Professor Dr. Christian Betzler who initiated this project and gave me the opportunity to write a PhD thesis. I am furthermore indebted to him for his continuous help, support and invaluable scientific input. I am also very grateful to Dr. Sebastian Lindhorst for providing valuable suggestions, hints and support throughout the writing of this thesis.

I am especially thankful to Professor Dr. Gregor Eberli for sharing his knowledge about carbonate sedimentology and the geology of the Bahamian archipelago. The discussions with him helped me to find my way through the data jungle to a valuable interpretation. Dr. Thomas Lüdman, Marco Paulat and Deniz Kula are acknowledged for the processing of the reflection seismic data. I also thank Dr. Gerhard Kuhn for providing us access to the XRF scanner at the Alfred Wegner Institut (Bremerhaven). I have to say thank you to Professor Dr. John Reijmer for his comments on my second manuscript. All surface samples used in this thesis were analysed by Lind Schiebel. Thank you, Linda for your incredible work! I have to thank my officemate and friend Khurram, for the discussions on geophysics, proof reading and the beautiful noise he is able to produce with his keyboard. The SCISS team is thanked, especially Dr. Ingo Harms and Berit Hachfeld, for extending my contract until October 2017. Rosa Flesch is thanked for her work on the gravity cores and the preparation of thin sections. I have to thank Jutta Richarz and Eva Vinx for their support in the laboratory, and Dirk Eggers for sharing sweets and coffee with me. I thank Jesús for the road trip all the way down to Italy. I deeply thank Juliane, Ilona, Freimut, Martin, Benedikt and Huaqing for being with me during this adventure. Thanks for being my friends!

I am eternally grateful to my family for their support and sympathy. Without their constant backing none of this would have been possible. I want to express my sincere gratitude to Chihiro, for her patience and understanding during all these years with various difficulties involved in producing a thesis.

Due thanks are also given to the German Science Foundation (DFG) who provided the financial support for the cruise M95 with the RV Meteor. My PhD position was funded within the cluster of Excellence "Integrated Climate System Analysis and Prediction" (CliSAP) at University of Hamburg.

